Atlantic water extent on the Faroe Current monitoring section
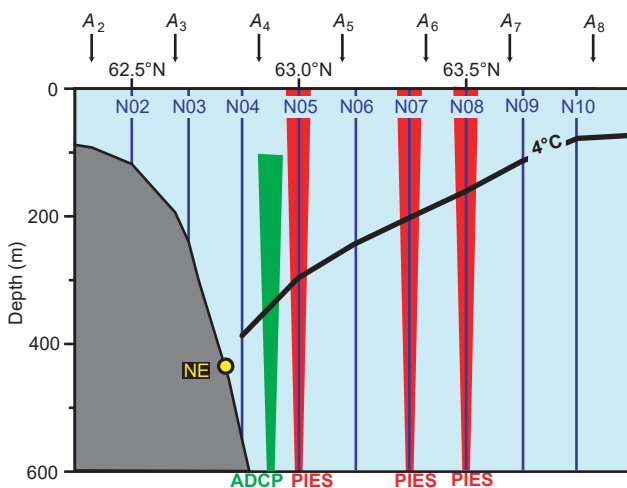
Tórshavn · May 2020

Bogi Hansen

Karin Margretha Húsgarð Larsen

Hjálmar Hátún

Svein Østerhus

1

Atlantic water extent
on the
Faroe Current monitoring section

Bogi Hansen, Karin Margretha Húsgarð Larsen, Hjálmar Hátún, Havstovan
Svein Østerhus, NORCE, Bergen

Abstract

This is the third in a series of reports documenting efforts to optimize the future monitoring system for the Faroe Current and optimize algorithms that allow high-quality extension of transport time series back to the start of satellite altimetry in 1993. Together, these reports serve to update the algorithms presented in Hansen et al. (2015). The first of these three reports (Hansen et al., 2019a) addressed the velocity field on the monitoring section and concluded that this field could be adequately simulated from satellite altimetry, once the altimetry data had been calibrated by in situ observations. The second report (Hansen et al., 2019b) addressed the hydrographic fields with the main focus on a preliminary analysis of the results from an experiment with two PIES (Pressure Inverted Echo Sounders) deployed on the section 2017-2019. From the analyses in this second report, it was concluded that PIES ought to be an integral part of the future monitoring system. The present report builds further on that and presents a complete design for the future monitoring system. The main topic discussed here is, however, how best to combine satellite and in situ data in order to simulate the Atlantic water extent and its variations throughout the satellite altimetry period, which is a prerequisite for generating time series of volume, heat, and salt transport of the Atlantic water in the Faroe Current as far back in time as possible at the present stage.

Content

1 Introduction and summary

1.1 Background and objectives

The Faroe branch of Atlantic inflow to the Nordic Seas crosses the Iceland-Faroe Ridge over a wide region where it would be demanding to monitor it, but east of the ridge it gets focused into a narrower current, the Faroe Current and this flow is monitored on the N-section extending northwards from the Faroe shelf (Figure 1.1). Hydrographic cruises along this section were initiated in the late 1980s and have been carried out 3-4 times each year since then so that more than a hundred CTD profiles have been obtained for most of the 14 standard stations on the section (Table 2.2). Regular ADCP deployments on the section started in 1997 and have been located at many points on the section, especially at site NB close to the core of the current. To complement the discontinuous CTD data, two PIES (Pressure Inverted Echo Sounders) were deployed at two of the standard stations in 2017 and recovered in 2019 (Figure 1.1b).
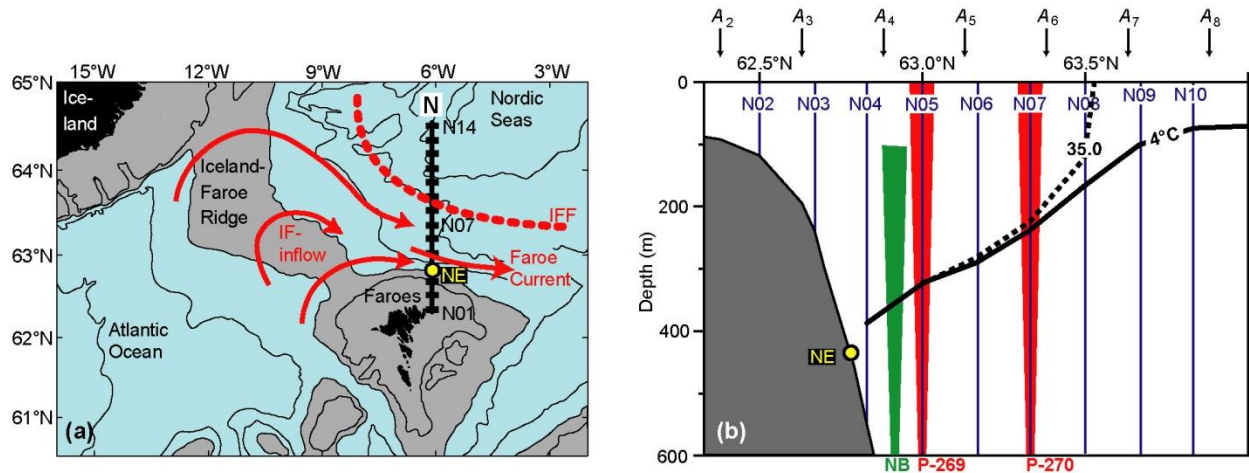
Figure 1.1. (a) The Iceland-Faroe region with red arrows indicating the Atlantic water inflow to the Nordic Seas between Iceland and Faroes (IF-inflow) and its continuation in the Faroe Current. The thick black line shows the monitoring section, the N-section, with CTD standard stations indicated by black rectangles labelled N01 to N14. **(b)** The central part of the monitoring section with the CTD standard stations from N02 to N10 indicated by vertical blue lines and altimetry grid points A_2 to A_8 indicated by arrows. The thick black lines show the average depths of the 4°C-isotherm (continuous) and the 35.0-isohaline (dashed). Red cones indicate the two moored PIES. Green cone indicates a long-term ADCP mooring at site NB. In both panels, site "NE" indicates bottom temperature monitoring.

Much of the motivation for gathering all these in situ observations has been to understand the local conditions and their influences on the marine ecosystem, but in addition, there has been a wish to monitor the transport of this important current, and this was the main motivation for deploying ADCPs along the section. The initial monitoring system for the Faroe branch was also totally based on in situ observations (Hansen et al., 2003). This in situ based monitoring system was, however, demanding to maintain, both in terms of manpower and funding. A systematic effort has therefore been ongoing for several years to optimize the system and make it less reliable on in situ observations. The first phase of this effort has been documented in Hansen et al. (2015), which concluded that altimetry complemented the in situ observations and could replace some of them, but there was no final conclusion as to the minimum necessary in situ system.

In addition to designing an optimized future monitoring system, efforts have been ongoing to determine time series of Faroe Current transport as far back in time and as accurately as possible in order to establish baselines on which to asses future variations.

Determining the transport of the Faroe Current can be split into two separate tasks: 1) determining the velocity field on the section, and 2) determining the hydrographic fields (temperature and salinity). The first of these tasks has been completed and documented (Hansen et al., 2019a) with the conclusion that the velocity field on the section and its variations on monthly time scales can be accurately determined from SLA (Sea Level Anomaly) data along a line of altimetry grid points adjacent to the monitoring section (Figure 1.1b) once they have been calibrated by the in situ observations. Here, the velocity field is to be understood as the horizontally averaged eastward velocity between neighbouring altimetry points at one meter interval from the surface down to 600 m depth..

This leaves the second task: determination of the hydrographic fields, both forward in time, and backward. This is required to derive heat (relative to some reference temperature) transport, but it is also required to distinguish the Atlantic water on the section from other water masses of Arctic origin. Various methods have been suggested for that purpose (Hansen et al., 2003), but Hansen et al. (2015) suggested to treat the hydrographic structure on the monitoring section as a two-layer system with an Atlantic water domain separated from the Arctic waters. Once the (variable) extent of this domain has been determined both vertically and horizontally, the volume transport of Atlantic water is found by integrating the velocity field over the domain.

Initial efforts to establish methods for determining the Atlantic water extent have been discussed in Hansen et al. (2015), but since then, more observational data have been acquired (CTD and PIES) and additional analyses of the total data set have generated new insight. The objective of this report is to document the results of these analyses with the aim to:

- design an optimized system for future monitoring of Atlantic water extent on the section that can ensure high-quality transport time series with minimal reliance on resource demanding in situ observations.

- develop algorithms that can use existing data from remote and in situ observations to extend time series of Atlantic water extent as far back in time as possible.

The first of these objectives has partly been realized already as documented by Hansen et al. (2019b), who concluded that an array of three moored PIES could monitor the Atlantic water extent along the section with high accuracy. In the present report, we will address the question of the future monitoring system and suggest some modifications to the system proposed in Hansen et al. (2019b), but the main focus here will be on generating time series of Atlantic water extent back in time.

The main features distinguishing Atlantic water from other water masses on the section are high temperature and high salinity. Typical temperatures in the core of the Atlantic water are around 8°C, whereas the deep waters of Arctic origin have temperatures around 0°C. This led Hansen et al. (2015) to use the 4°C-isotherm as Atlantic water boundary towards the deep waters. We will generally keep this criterion, although with slight modifications, and much of the report focuses on this isotherm.

This criterion is appropriate in the southern part of the Atlantic domain where the Atlantic water usually reaches large depths, but the boundary shoals towards the north (Figure 1.1). In the northern boundary region, both the Atlantic layer and the Arctic waters are affected by seasonal heating and

temperature is not a good criterion to distinguish between them. Instead, Hansen et al. (2015) suggested the 35.0-isohaline (practical salinity) as the northward boundary. In the report, we will discuss and modify this criterion.

The effort to develop a high-quality monitoring system for the Faroe Current and derive transport time series has been ongoing for a long time and has received support from many different sources. During the last phase and the completion of this report, we have especially received support from the Danish Ministry of Climate, Energy and Utilities as part of the Arctic Climate Support Programme and from the European Union's Horizon 2020 research and innovation programme under grant agreement no. 727852 (Blue-Action).

1.2 Structure of the report

The report starts in Chapter 2 with a description of the Atlantic water properties on the monitoring section, their spatial and temporal variations with a special focus on the 4°C-isotherm and its depth variations. This continues in Chapter 3 with a discussion of the 2017 – 2019 experiment with two PIES deployed on the section. Preliminary results from this experiment were reported in Hansen et al. (2019b), but when that report was written, altimetry data, which are used to process the PIES data, had not been updated for much of the experimental period. Chapter 3 also includes some additional features into the processing of the PIES data, so that the time series of 4°C-isotherm depths from the PIES experiment presented here should be more accurate than those presented in Hansen et al. (2019b).

The three following chapters attempt to use all the available remote and in situ observational data to extend time series of Atlantic water extent back in time, for as long, and with as much accuracy as possible. Chapter 4 discusses the extent to which the depth of the 4°C-isotherm can be derived from ADCP data, especially from the long-term ADCP site NB (Figure 1.1b).

Similarly, Chapter 5 discusses how the variations of this isotherm can be derived from altimetry data, alone. Since the altimetry data are the main basis for determining the variations of the velocity field (Hansen et al., 2019a), the altimetry period (since 1st January 1993) determines the longest period for which transport time series can be derived. It is therefore important to determine time series of Atlantic water extent for the whole of this period, even at times when no in situ data have been available. Algorithms to do this task were developed in Hansen et al. (2015), but new data (additional CTD data and PIES data) as well as new insights allow refinements of these algorithms to make them more accurate.

Almost without exception, Atlantic water has been found to dominate the shallow southern part of the monitoring section from surface to bottom. Determining the variations of the Atlantic water boundary towards the deep water therefore involves determining the depth variations of the 4°C-isotherm from station N04 northward until this isotherm becomes too shallow, usually in the vicinity of station N08 or N09 (Figure 1.1b). In Chapter 5 it is concluded that this can indeed be done from altimetry data alone with a fairly high accuracy from station N05 to station N08 (Sect. 5.5).

The 4°C-isotherm depth at station N04, on the other hand, does not appear to be tightly linked to altimetry, which is unfortunate since this is usually the station with the deepest Atlantic water extent and close to the typical location of the Atlantic water core. There are, however, two additional sources of in situ data that may be used: the ADCP data from site NB (discussed in Chapter 4) and measurements of bottom temperature at site NE (Figure 1.1). The combination of these two data sources with the altimetry data to generate time series of isotherm depth at N04 are discussed in Chapter 6.

As we approach the northern parts of the Atlantic water domain on the section, air-sea heat exchange makes temperature unfit as a criterion to distinguish between Atlantic water and other water masses.

Hansen et al. (2015) suggested using the 35.0-isohaline instead and developed algorithms to simulate the location (latitude) of this isohaline. In Chapter 7, this criterion is discussed and modified and a new algorithm is developed to simulate the location of the northern boundary of Atlantic water extent on the section.

Finally, Chapter 8 documents how the algorithms developed to monitor and simulate Atlantic water extent can be incorporated into transport estimates and what the effects are on the transport time series. This chapter also discusses the accuracy of the transport time series produced.

Many readers may find this report confusing. The analyses documented in the report are the result of an elaborate process and similar questions are sometimes addressed in separate parts of the report and sometimes with different notation. Hopefully, the summary presented in Sect. 1.3 can help the reader to navigate the report more easily. Also, some results are included even though they have not been utilized for the main purpose of the report. This has been done deliberately. Havstovan aims to continue monitoring the Faroe Current into the foreseeable future and it would probably be naive to expect no future modifications of the monitoring system or algorithms. To avoid future duplication of the analysis, results that have not shown any immediate utility have therefore been retained in the report.

1.3 Summary of results and recommendations

As mentioned in Sect. 1.1, this report has two main objectives: to optimize determination of Atlantic water extent in a new monitoring system, and to calculate time series of Atlantic water extent back in time. These two topics are summarized separately in the following.
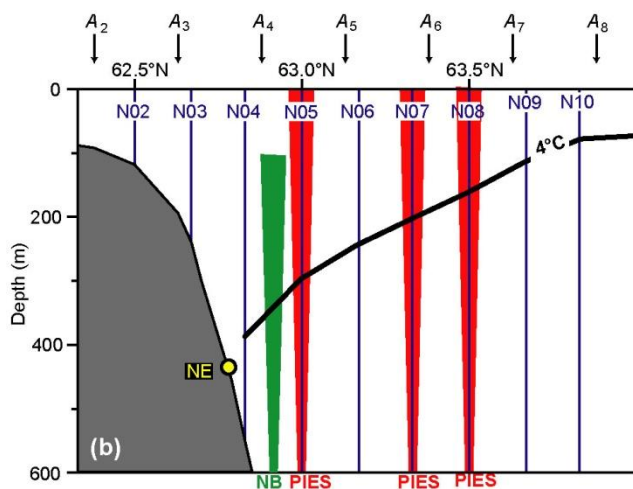
Figure 1.2. The planned new monitoring system for the Faroe Current.

1.3.1 Design of an optimized monitoring system

As new data and technology become available, the new monitoring system will undoubtedly require modifications, but its basic structure is built on five components, planned to be implemented in 2020 or as soon as funding and acquisition of instruments allow (Figure 1.2):

- Satellite altimetry along 6.125°W longitude to provide SLA data, from which the velocity field is determined (Hansen et al., 2019a) and to help monitoring the 4°C-isotherm depth

along the section as discussed in chapters 5 and 6, as well as the northern boundary of Atlantic water extent (Chapter 7).

- One ADCP at site NB to serve as backup, if major changes to the velocity field should disrupt the established relationships between altimetry and velocity field.

- Three PIES deployed on the bottom at stations N05, N07, and N08 to monitor the depth of the 4°C-isotherm at these stations. In Hansen et al. (2019b), the third PIES was suggested to be deployed at station N09, rather than N08, but the analysis in Sect. 7.3 shows that a PIES at N09 would not be able to monitor the isotherm accurately and that N08 is a preferable site for a PIES deployment. Isotherm depths at the intermediate station N06 are determined by interpolation (Sect. 5.5.2). Each PIES will be moored for several years and data uploaded regularly to research vessel.

- One bottom temperature logger deployed on the bottom in a protective frame at site NE. The presently installed system (Figure 6.1b) ought to remain operational until June 2022, but has not proved to be very reliable. This component may need re-assessment in the future.

- Regular (at least three times a year) CTD cruises along the section. These cruises – which also include other (e.g., plankton) observations – will provide data on long-term variations of the Atlantic water temperature and salinity and update the hydrographic data set to allow continuous refinement of algorithms.

1.3.2 Extending time series of Atlantic water extent back in time

The basic methodology, both for future monitoring, and for backward extension of time series, as established in Hansen et al. (2015) is to determine Atlantic water extent on the standard stations and then interpolate this information onto the grid of altimetry points (Figure 1.2), for which the velocity field is defined. The reason for this is that almost all our knowledge about hydrography and Atlantic water extent derives from CTD observations (and lately also PIES) at the standard stations.

Thus, the task is to use the CTD and PIES data to develop relationships between Atlantic water extent at the standard stations and altimetry and/or other available observational data. Over most of the section, this primarily involves determining the 4°C-isotherm depth at each station. Since we aim at producing monthly averaged transport values for the whole altimetry period, this means generating monthly averaged values for the depth of this isotherm, $D_j(t)$, for stations N04 to N10 (i.e., $j = 4,…,10$) for this period.

For most of the stations, it is found (Sect. 5.4.2) that there is a consistent seasonal variation of $D_j(t)$, which may be characterized by its amplitude, A_j, and the day of maximum, Day_j (1,…,365). In addition, there is a long-term variation that can be approximated as a linear trend, γ_j, in time plus a linear dependence on the temperature of the core of Atlantic water, $T_A(t)$.

As discussed in Chapter 5, much of the remaining variation of $D_j(t)$ can be explained by parameters derived from altimetry data. Hansen et al. (2019b) noted an almost instantaneous geostrophic adjustment between sea level height and isopycnal (i.e., also isothermal) depth. This is verified in Figure 5.9. In Sect. 4.3, it is also documented that the 4°C-isotherm depth in the southern part of the section tends to follow

the "velocity transition depth" at the core of the current (site NB), i.e., the depth at which the upper-layer eastward velocity is slowing down. Since this depth is also reflected in the altimetry data, relationships between isotherm depth and altimetry were to be expected.

Several combinations of altimetry parameters were found to have high explanatory power (Chapter 5), but overall, the best choice was found to be a linear combination of the SLA (Sea Level Anomaly) value interpolated to the latitude of the station, $h_j(t)$, and the principal component of the first EOF mode of SLA along the section, PcAH-1(t) (Sect. 5.2). For every day in the altimetry period, it is therefore possible to simulate $D_j(t)$ by an expression of the type:

$$D_j(t) = D_{0,j} + \gamma_j \cdot t + a_j \cdot [T_A(t) - \langle T_A \rangle] + A_j \cdot cos\left[2\pi \cdot \left(t - \frac{Day_j}{365}\right)\right] + a_{h,j} \cdot h_j(t) + a_{x,j} \cdot \text{PcAH-1(t)} \quad (1.1)$$

where t is the time (in years) since 1993, $\langle T_A \rangle$ is the average of $T_A(t)$ between 1993 and 2017 (8.336°C) and both $h_j(t)$ and PcAH-1(t) have been de-trended and de-seasoned (Sect. 5.3). The coefficients in this equation for stations N04 to N10 are listed in Table 1.1, which also lists how much of the variance in $D_j(t)$ (as observed by CTD) is explained by Eq. (1.1).

Table 1.1. Coefficients to use with Eq. (1.1) to simulate 4°C-isotherm depth at stations N04 to N10, explained variance (R^2) of the isotherm depths measured by CTD, and number of CTD profiles used (N). Based on Chapter 5.

Coeff.:	$D_{0,j}$	γ_j	$a_{TA,j}$	A_j	Day_j	$a_{h,j}$	$a_{x,j}$	R^2	N
Unit:	m	m/yr	m/°C	m			m		
N04:	365	1.97	0.0	25	298	1522	-60.30	0.31	112
N05:	257	2.33	30.6	32	294	3178	-151.38	0.62	115
N06:	205	3.20	44.0	45	283	2511	-135.41	0.58	102
N07:	161	3.16	45.1	65	262	2011	-94.09	0.66	105
N08:	113	3.12	30.4	56	269	1762	-63.33	0.63	102
N09:	57	3.00	0.0	48	262	872	0.00	0.56	101
N10:	47	1.21	0.0	48	270	437	0.00	0.54	98

For stations N05 to N08, Eq. (1.1) thus explains considerably more than half the variance in the 4°C-isotherm depths observed by the CTD profiles. As seen in the two top rows of Table 1.2, this is in most cases better than the simulations suggested by Hansen et al. (2015), but only marginally so. It appears, however, that at least some of the values for R^2 in Table 1.1 are much too pessimistic when used for monthly averages rather than the snapshot values provided by CTD profiles. This is seen when the fits developed from the CTD data (Eq. (1.1) with the coefficients in Table 1.1) are used on 28-day averaged isotherm depth from the PIES data (bottom row in Table 1.2).

Table 1.2. Explained variance (R^2) of the 4°C-isotherm depth at the five deep stations in the Atlantic part of the section. The top row lists R^2 in the fits by Hansen et al. (2015) based on CTD data (between 85 and 97 profiles for each station). The middle row lists R^2 in the fits by Eq. (1.1) based on updated CTD data (between 102 and 115 profiles for each station). The bottom row lists R^2 in the fits defined by Eq. (1.1) based on 28-day averaged PIES data from stations N05 (22 values) and N07 (20 values).

Station:	N04	N05	N06	N07	N08
H2015-CTD:	0.30	0.56	0.58	0.65	0.62
Eq.(1.1)-CTD:	0.31	0.62	0.58	0.66	0.63
Eq.(1.1)-PIES:		0.77		0.79	

Thus, the fits that were generated from the snapshot CTD profiles 1993-2019 for stations N05 and N07 have much higher explained variances when used on 28-day averaged altimetry in the PIES period than

when compared with the data, from which they were generated. For both stations, the difference between the 28-day averaged isotherm depth from PIES and the fit had a standard deviation less than 30 m and average (bias) not more than 2 m (Table 5.15).

Part of the explanation for this rather amazing result is, no doubt, that much of the variance of the CTD-derived isotherm depths stems from short-term variations such as internal waves and meso-scale features passing through the monitoring section (Sect. 2.3.1 and Sect. 5.4.1). An EOF analysis of the eastward surface velocity generated from altimetry shows that around one third (32%) of the variance in the surface velocity is explained by an "Eddy mode" representing (stronger cyclonic than anticyclonic) meso-scale (≈50 km) features (Sect. 5.4.1).

This Eddy mode is likely to affect the isotherm depths determined by snapshot CTD profiles strongly. The autocorrelation of its principal component (termed PcAU-2) rapidly decreases, however, and is essentially zero for lags of 3-4 weeks (Figure 5.5b). For monthly averages, its contribution ought therefore to be small. Also, altimetry data, as well as relationships based on geostrophy, should be more accurate when averaged over monthly, rather than daily, time scales. Since we have chosen only to include linear relationships in Eq. (1.1), it appears that much of the noise in the data from these sources is averaged out on monthly time scales. This can help understand how a relationship can explain more of the variance in monthly averages than in the snapshot CTD data, from which it was generated (Table 1.2).

Continuous isotherm depth data that allow monthly averaging are only available for N05 and N07, but there would not seem to be any reason that the fits developed for stations N06 and N08 from the CTD data 1993-2019 should perform substantially worse than the fits for N05 and N07 when used on 28-day averaged altimetry data. Thus, it may be concluded that: *Over most of its length (N05 to N08), the monthly averaged depth of the Atlantic layer on the section can be accurately determined from altimetry data alone*.

Unfortunately, this result does not necessarily apply to station N04 (Table 1.1), which usually is the station with the deepest Atlantic water layer and close to the Atlantic water core on the section. Hansen et al. (2015) showed that the fit for this station could be substantially improved by including the bottom temperature at site NE (Figure 1.1) and this is verified in Sect. 6.1.2 (R^2 increasing from 0.31 to 0.66), but in the period 1993 to 2019, the bottom temperature at NE was measured less than half the time (lower part of Figure 8.1a).

A more complete record exists for the ADCP at site NB, which has been operational 94% of the time from June 1997 until the end of the last deployment so far in May 2019. Attempts to use the back-scattering strength measured by the ADCP at this site to determine isotherm depth indicated a relationship, but the uncertainty is too high for isotherm depth determination from backscattering strength to be of use (Sect. 4.1).

Useful information on isotherm depth can, however, be gained from the velocity measurements at NB. Site NB is almost exactly midway between stations N04 and N05 (Figure 1.1b). Through the thermal wind equation, the vertical shear of the eastward velocity at this site is therefore related to the difference between the isotherm depths at the two stations (Sect. 4.2.3). Since the isotherm depth at N05 can be simulated with a fair degree of accuracy (Table 1.2), this also allows simulation of isotherm depth at N04 with increased accuracy relative to Table 1.1, whenever there was an ADCP at site NB (Sect. 6.2.1). When incorporated into volume transport estimates, it appears, however, that this method for isotherm determination at N04 produces unrealistic values for monthly averaged volume transport (Sect. 8.1.1) and it was therefore abandoned.

As previously mentioned, the 4°C-isotherm is no longer a good indicator of Atlantic water extent in the northern part of the section where it approaches the surface. Instead Hansen et al. (2015) suggested to use the 35.0-isohaline at 100 m depth as the northern boundary and developed algorithms to simulate the location of this boundary from altimetry data. This definition does not take into account the pronounced salinity variations of the Atlantic water core, especially after 2015 (Figure 2.2a) and the choice of the 35.0-isohaline at a specific depth also seems rather ad hoc.

As discussed in Chapter 7, a new definition of the northern Atlantic water boundary has therefore been developed. Rather than using the salinity at 100 m depth, the maximum salinity in the water column between 20 m and 300 m depth is used for this new definition. In the period since 1997 with the highest quality salinity measurements, there have been 80 cruises with CTD observations at all the standard stations from N04 to N10. From each of these cruises, the maximum salinity can therefore be determined at all of the stations.

To reduce the effect of long-term Atlantic water salinity variations (Figure 2.2a) these maximum salinity values were then "normalized", Eq. (7.2). From an EOF analysis of the normalized maximum salinity values, the dominant mode (explaining 45% of the variance, Table 7.1) seemed to be less affected by meso-scale variability than Mode 2 and Mode 3 (Figure 7.5b). The principal component of the first mode (termed PcS_1) was found to be significantly correlated with several altimetry parameters (Table 7.2) and a multiple regression analysis gave a relationship, which explains 58% of the variance in PcS_1.

Using this relationship, the variations of normalized maximum salinity associated with the first EOF mode can thus be simulated, Eq. (7.3), with a fairly high accuracy for every month of the altimetry period. Once a reference salinity, "S_{Bound}", has been defined, the location (latitude), where the normalized maximum salinity crosses this reference value can then be determined, which by definition is the northern boundary of the Atlantic water extent on the section. The choice of a value for S_{Bound} is not unambiguous (Sect. 7.1.4) and will affect the average transport value of Atlantic water. It ought not to have much influence on the temporal transport variations, however. The chosen value ($S_{Bound} = 35.075$) gives a northern boundary, which has a seasonal variation (Figure 7.9) that is consistent with the seasonal variation of the 4°C-isotherm and other information.

The final task is to incorporate the new algorithms for Atlantic water extent into the calculation of transport time series. For volume transport, the methodology of Hansen et al. (2015) is used, Eq. (8.1), although the definition of the 4°C-isotherm as the deep Atlantic water boundary has been slightly modified to account for changes in the temperature of the core of Atlantic water, as discussed in Sect 8.1.

For most of the period since January 1993, the availability of in situ observations that measure Atlantic water extent directly has been scarce. As was the case for Hansen et al. (2015), the "new" volume transport time series based on this report is thus to a very large extent based on altimetry data; not only for the velocity field, but also for the Atlantic water extent. The algorithms used to simulate Atlantic water extent from altimetry data were mainly developed from CTD data as discussed above and, a priori, the accuracy of monthly averaged transport values based on them is not well known.

It is therefore encouraging that Table 1.2 indicates that these algorithms might in fact be much more accurate when used for monthly averages rather than snapshot CTD observations and this is supported by the discussion in Sect. 8.1.1. There, monthly averaged transport values, based on altimetry data only, are compared with transport values using in situ observations to estimate Atlantic water depth at station N04 (Figure 8.2) and stations N05, N06, and N07 (Figure 8.3) for months with available in situ observations.

Unfortunately, we do not have in situ observations that allow estimation of Atlantic water extent over the whole section simultaneously on monthly time scales. When a future monitoring system hopefully has

provided such a data set, this question should be re-addressed and a more quantitative estimate should be obtained of the uncertainty involved in volume transport based on altimetry only. At the present stage, we can only repeat the message from Sect. 8.1.1 that monthly averaged volume transport, based on altimetry only, seems to be much more accurate than might have been expected. Part of the reason for that is, no doubt, that the Atlantic water boundary usually is located at depths or in regions where the velocity is considerably weaker than at the core (Sect. 4.3) so that variations in boundary location have limited effect on transport.

The "new" algorithms give almost the same average volume transport for the period 1993-2018 as the "old" algorithms and the two series are highly correlated as documented in Table 1.3 and Figure 1.3. This table and figure use updated algorithms for the velocity field compared with Hansen et al. (2015), but the changes in volume transport introduced by this were also small (Figure 13 in Hansen et al., 2019a).

Table 1.3. Comparison of volume and heat transport (relative to 0°C) as calculated by the "Old" (Hansen et al., 2015) algorithms for Atlantic water extent and the "New" algorithms, documented in this report. "Avg" is average. "Std" is standard deviation. "R" is the correlation coefficient. "Max" is the (numerically) maximal difference between the old and the new estimates. Based on monthly averages 1993-2018. The same velocity field (Hansen et al., 2019a) was used for both cases.

	Old		New		Old-New		
	Avg	Std	Avg	Std	R	Std	Max
Volume tr.:	3.83 Sv	0.58 Sv	3.82 Sv	0.55 Sv	0.96***	0.17 Sv	0.64 Sv
Heat tr.:	124.5 TW	21.7 TW	124.5 TW	19.6 TW	0.97***	5.6 TW	20.4 TW

Thus, the main conclusions drawn by Hansen et al. (2015) will not be affected by the modifications introduced in this report. For the period 1993 to 2018, the volume transport had a positive trend (0.013 ± 0.012) Sv yr^{-1} with 95% confidence interval.
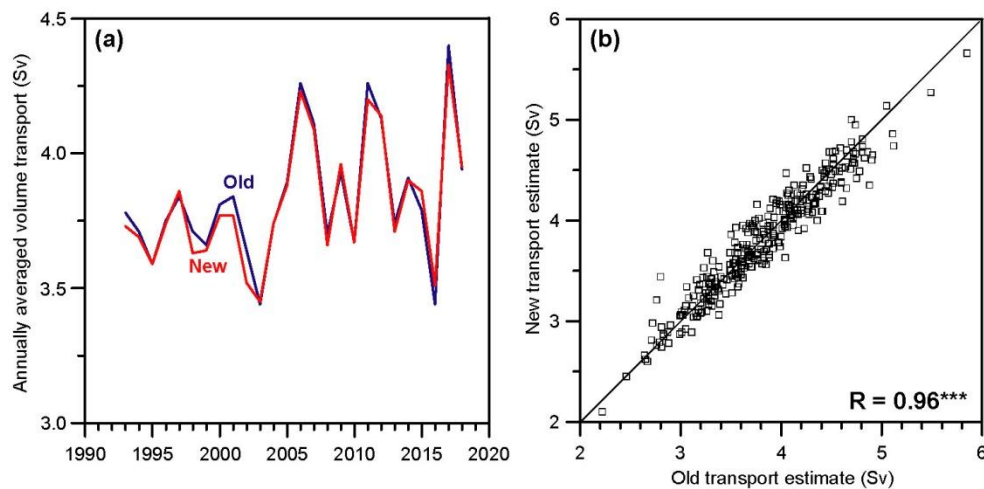
Figure 1.3. Comparison of volume transport of Atlantic water in the Faroe Current based on this work (New) with transport values calculated using the algorithms for Atlantic water extent in Hansen et al. (2015) (Old). **(a)** Annually averaged volume transport. **(b)** Monthly averaged volume transport. The same velocity field (Hansen et al., 2019a) was used for both cases.

With the same definition of heat transport (relative to 0°C) as used in Hansen et al. (2015), the "old" and the "new" time series also compare favourably (Table 1.3). It should be kept in mind, however, that this definition includes heat outside (below) the Atlantic layer, which is presumed to be from Atlantic water

that has been mixed out of the Atlantic water domain on the monitoring section (Sect. 8.2). To allow calculation of heat transport for the Atlantic water domain only, a time series of monthly values for transport-averaged temperature, Eq. (8.2), has been calculated (Figure 1.4a), which may be combined with volume transport to derive heat transport for the Atlantic water domain of the Faroe Current for any given reference temperature.
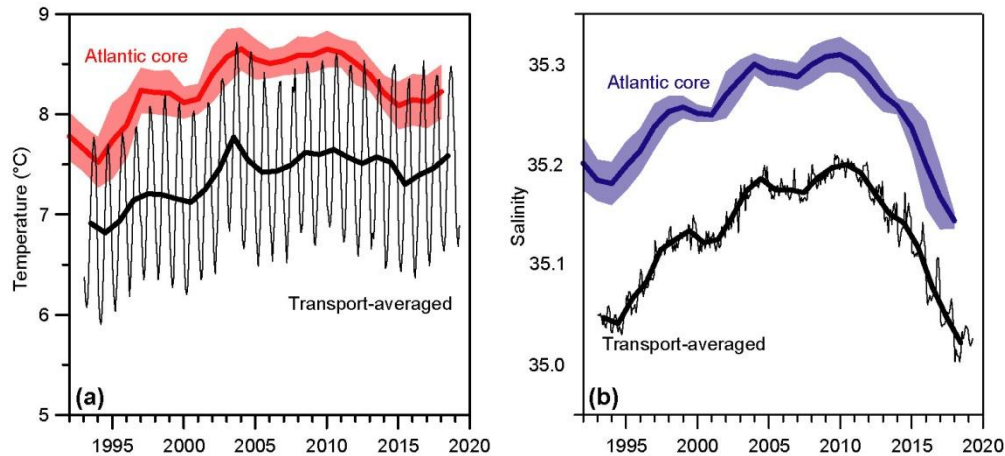
Figure 1.4. (a) Monthly (thin black line) and annual (thick black line) values of transport-averaged temperature plotted together with low-passed Atlantic core temperature (from Figure 2.2a). **(b)** Monthly (thin black line) and annual (thick black line) values of transport-averaged salinity plotted together with low-passed Atlantic core salinity (from Figure 2.2a).

As expected, the transport-averaged temperature (Figure 1.4a) exhibits strong seasonality and it is usually considerably lower than the low-passed temperature of the Atlantic water core, but the long-term variations are similar. Multiplying this temperature by the volume transport and specific heat (per volume), we obtain the heat transport within the Atlantic water domain of the Faroe Current. For the 1993-2018 period, the overall average heat transport relative to 0°C, defined in this way, was 115.4 TW, i.e., 7% less than the value in Table 1.3, obtained by using the definition in Hansen et al. (2015).

In the 1993 to 2018 period, heat transport (relative to 0°C) as defined by Hansen et al. (2015) increased by (0.62 ± 0.39) TW yr^{-1} while the heat transport of the Atlantic water domain increased by (0.76 ± 0.36) TW yr^{-1}.

In addition to heat, Hansen et al. (2015) reported time series of salt transport, which again include water outside the Atlantic water domain, presumed to be of Atlantic origin. These calculations were, however, based on a fairly arbitrary choice of a "boundary salinity" and have led to some confusion. We therefore no longer report salt transport. Instead, we report monthly values for transport-averaged salinity, Eq. (8.3), illustrated in Figure 1.4b, from which one can derive salt transport, Eq. (8.4), as well as the equivalent freshwater transport, Eq. (8.5), once a reference salinity has been specified.

2 Atlantic water on the monitoring section

2.1 Water masses on the section

In the CTD data set, there are 78 cruises with complete coverage at all fourteen standard stations. Although these cruises are not homogeneously distributed in time, the average temperature and salinity distributions based on all the cruises (Figure 2.1) ought to give a good picture of the general water mass distribution on the section.

In the literature, a number of different water masses have been discussed for this region, but we will only distinguish between two: *Atlantic water* and *Arctic water*. The Atlantic water is characterized by relatively high salinity and in deeper layers also with relatively high temperature. On the average distribution (Figure 2.1), the Atlantic water core is located close to 100 m depth around station N03, where the highest salinity is found, but it move with time.
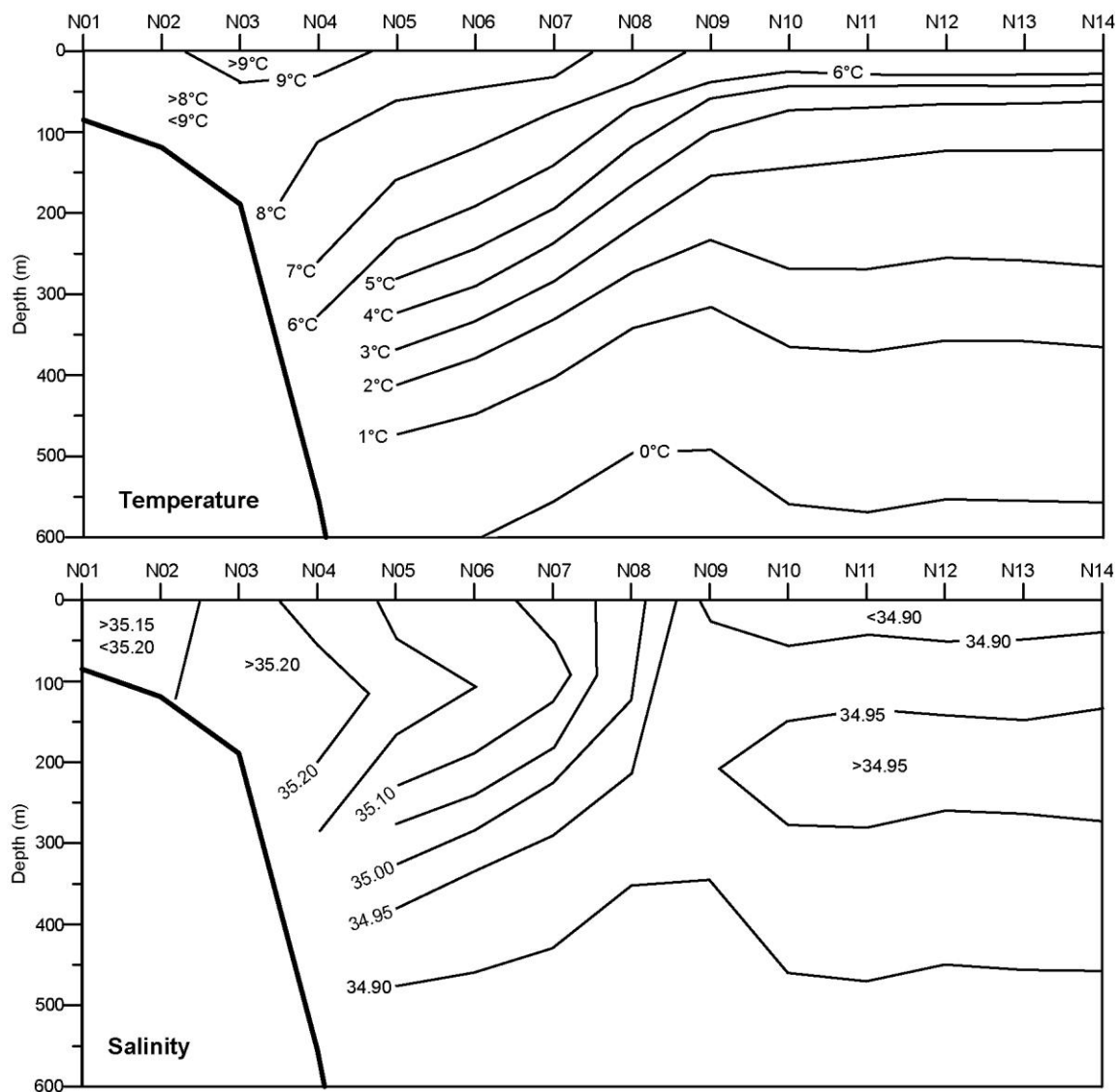
Figure 2.1. Average temperature (top) and salinity (bottom) distribution on the section based on 78 CTD cruises 1989-2018 with complete coverage at all the fourteen standard stations.

2.2 Temperature and salinity variations

2.2.1 Variations of Atlantic water properties

Traditionally, the Atlantic water core on a given CTD cruise is determined as that 50 m high layer between stations N03 and N07 which has the highest salinity averaged over the layer and the Atlantic water temperature and salinity for that cruise are determined as averages over the layer. Using an iterative procedure (Appendix A), the time series of these values, $T_A(t)$, may be split into seasonal and long-term variations:

$$T_A(t) \cong T_{A3yr}(t) + a_T \cdot cos\left[\frac{2\pi}{1\,year} \cdot (t - t_{Max})\right] \qquad (2.1)$$

where $T_{A3yr}(t)$, is the 3-year running mean of the Atlantic water temperature while a_T and t_{Max} are the seasonal amplitude and time of maximum, respectively. The original values established by Larsen et al. (2012) were: $a_T = 0.55°C$ and $t_{Max} = 244$ (day number in the year). With the more comprehensive data set available here (111 cruises), these values may be slightly modified: $a_T = 0.57°C$ and $t_{Max} = 247$ (day number in the year), i.e., early September (Figure 2.2b). The maximum correlation coefficient of the sinusoidal fit (Appendix A) was 0.86. For Atlantic water salinity, the seasonal variation is less pronounced (Appendix B), but its long-term variations were parallel to temperature until around 2015 (Figure 2.2a).
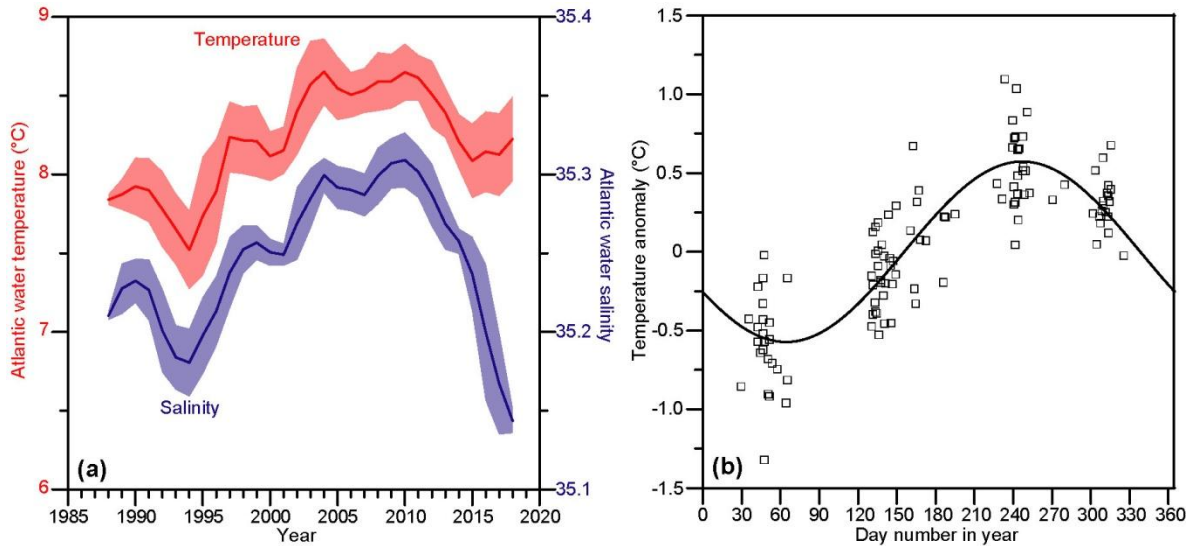
Figure 2.2. Atlantic water properties on the section. **(a)** Long-term (3-year running mean) temperature (red) and salinity (blue). The shaded areas represent ± twice the standard error computed for each 3-year period. **(b)** The temperature anomaly, defined as the deviation from the 3-year running mean, plotted against day number of the year. Each square is from one CTD cruise. The continuous line shows the sinusoidal fit to the temperature anomaly.

2.2.2 Temperature variations at fixed locations

The iterative procedure (Appendix A) has also been used to analyze temperature, salinity, and density variations close to the surface (10 m depth) and at 100 m depth intervals for all the standard stations. Details of the seasonal variation are listed in Appendix B and Table 2.1 lists the seasonal amplitude and time of maximum temperature (a_T and t_{Max} in Eq. (2.1)). As might be expected, the seasonal amplitudes are highest close to the surface, especially in the northern part of the section where a low-salinity layer may stimulate stratification in summer. Over most of the section, the maximum temperature occurs

around the same time or a bit later than the Atlantic water maximum. At mid-depth in the northernmost part of the section, on the other hand, maximum temperature occurs during the first months of the year.

Table 2.1a. Amplitudes (°C) of the seasonal temperature variation at selected depths for all the standard stations.

Depth	N01	N02	N03	N04	N05	N06	N07	N08	N09	N10	N11	N12	N13	N14
10m	1.78	1.66	1.64	1.81	1.85	1.98	2.30	2.55	2.75	3.12	3.32	3.46	3.52	3.56
100m		1.63	0.95	0.76	0.82	1.00	1.34	1.41	0.95	0.70	0.40	0.38	0.19	0.27
200m				0.75	0.97	1.16	1.51	1.08	0.48	0.16	0.16	0.16	0.10	0.06
300m				0.82	0.86	1.07	1.05	0.62	0.30	0.09	0.06	0.12	0.08	0.03
400m				0.60	0.40	0.49	0.53	0.29	0.13	0.09	0.05	0.08	0.06	0.03
500m				0.20	0.14	0.29	0.21	0.12	0.05	0.03	0.03	0.04	0.03	0.01
600m					0.07	0.12	0.08	0.05	0.01	0.01	0.02	0.02	0.02	0.01

Table 2.1b. Time of maximum (day number) of the seasonal temperature variation at selected depths for all the standard stations.

Depth	N01	N02	N03	N04	N05	N06	N07	N08	N09	N10	N11	N12	N13	N14
10m	254	252	244	238	234	236	231	231	234	241	244	242	242	241
100m		259	262	259	275	280	266	278	277	289	301	333	321	328
200m				273	296	281	270	276	264	287	351	51	23	12
300m				287	299	267	261	259	249	216	348	73	23	13
400m				307	302	263	248	249	255	238	319	53	13	22
500m				10	270	246	246	256	268	232	350	40	3	24
600m					273	256	247	248	262	289	362	56	20	355

The long-term temperature variation near the surface (10 m depth) is illustrated in Figure 2.3. In the southernmost part of the section (N01 to N05), the low-passed near-surface temperature varies in parallel with the Atlantic water temperature, although warmest at N03. Farther north on the section, the near-surface temperature seems to vary considerably more. The large seasonal variation in the northern part (Table 2.1a) implies that temporally inhomogeneous sampling may bias the long-term estimates considerably, but the figure indicates that the cooling after 2010 is mainly confined to the southern part of the section.
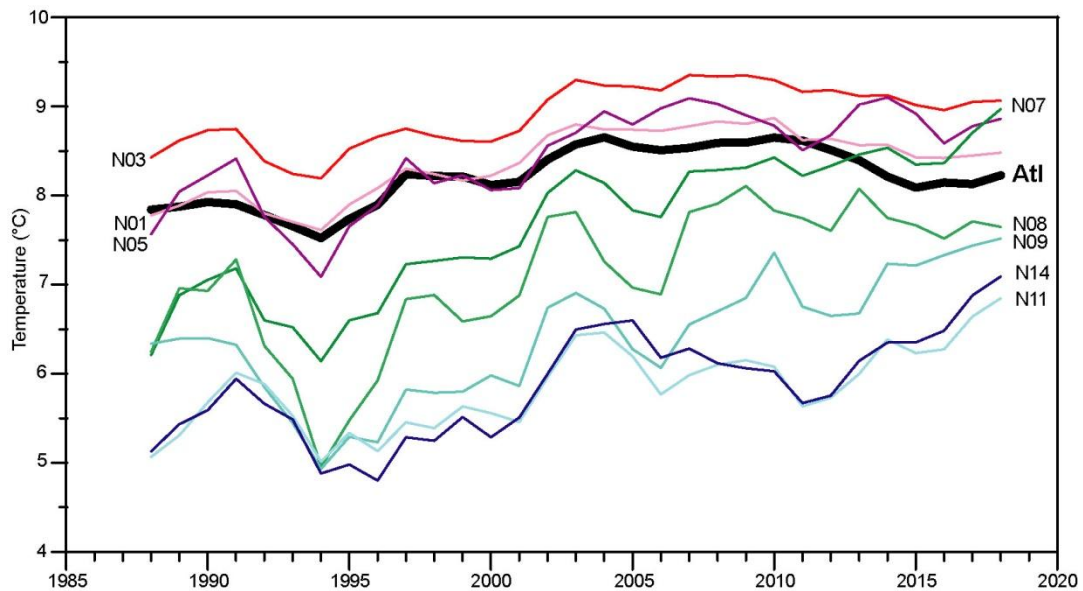
Figure 2.3. Long-term (3-year running mean) variation of the temperature at 10 m depth for selected standard stations. The thick black line shows the long-term variation of the Atlantic water temperature (copied from Figure 2.2a).

An impression of the long-term temperature variation at depth may be gained from Figure 2.4. At N05, the minimum around 1994 is seen at all levels down to at least 500 m depth. More northerly, this is much less pronounced and the deep levels at N09 seem to have been coldest in the early 2000s.
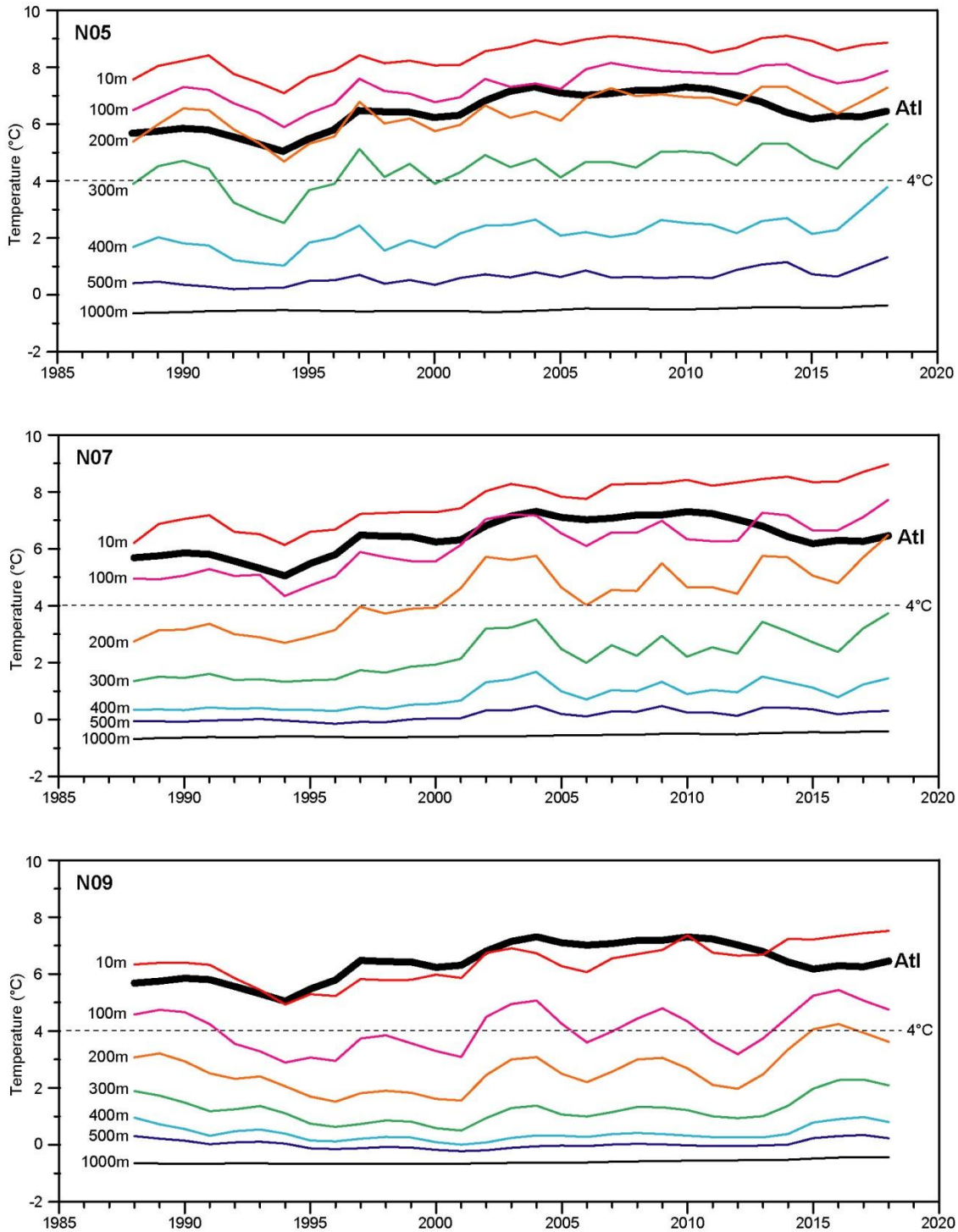
Figure 2.4. Long-term (3-year running mean) variation of the temperature at selected depths for three standard stations. The thick black lines show the long-term variation of the Atlantic water temperature (copied from Figure 2.2a). The dashed lines indicate 4°C.

2.3 Variations of the 4°C-isotherm depth

From the preceding discussion it is seen that the Atlantic water temperature has remained close to 8°C whereas the Arctic below the Atlantic layer is close to 0°C. This was the motivation for choosing the 4°C-isotherm as the lower boundary of the Atlantic layer over most of the section (Hansen et al., 2015). Determination of the depth variations of this isotherm is therefore an essential ingredient in transport estimates. In Appendix C, some essential features of this isotherm, which were tabulated in Hansen et al. (2019b), are listed for easy access (Tables C1, C2).

2.3.1 Short-term variations of the 4°C-isotherm

The isotherm depth, determined from the CTD profiles, is a snapshot, which in principle is valid only at the time when the CTD passes through the isotherm, but disturbances – such as internal waves – will distort the water and hence isotherms vertically. An impression of the uncertainty induced by this may be obtained by comparing the isotherm depth from the CTD down-profile with that from the following up-profile.

To illustrate this variability, we have focused on the two standard stations, N05 and N07. Since 2006, separate down- and up-profiles have been stored from 47 occupations at N05 and 45 occupations at N07. As seen in Figure 2.5, the difference is usually only a few meters and average differences are smaller than 10 m.

The typical duration between downward and upward passage of the CTD through the 4°C-isotherm is ≈30 minutes. Using the density gradient between the 4.5°C-isotherm and the 3.5°C-isotherm, the average buoyancy frequency around the 4°C-isotherm is ≈0.004 s^{-1}, equivalent to a period ≈26 minutes. We would therefore expect Figure 2.5 to be fairly representative for the effect of interval waves on the short-term variations of the 4°C-isotherm.
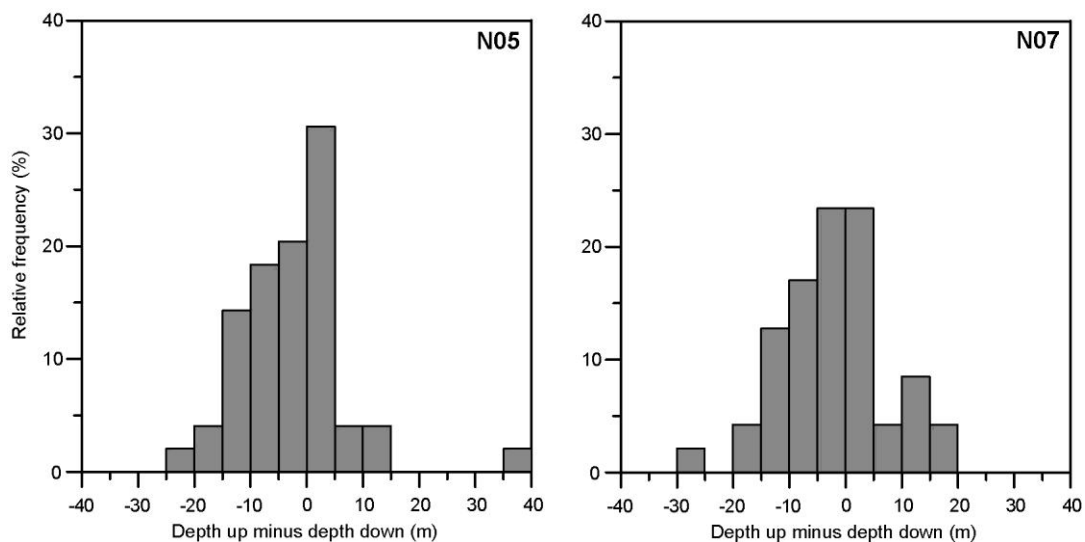
Figure 2.5. Frequency distribution of the difference in 4°C-isotherm depth as determined from up- and down- profiles measured by the CTD.

2.3.2 Seasonal and long-term variations of the 4°C-isotherm

On longer time scales, the depth of the 4°C-isotherm varies much more dramatically, which again may be illustrated for stations N05 and N07 (Figure 2.6). At N05, it seems difficult to identify any consistency, but N07 appears perhaps to have both a seasonal and a long-term variation.
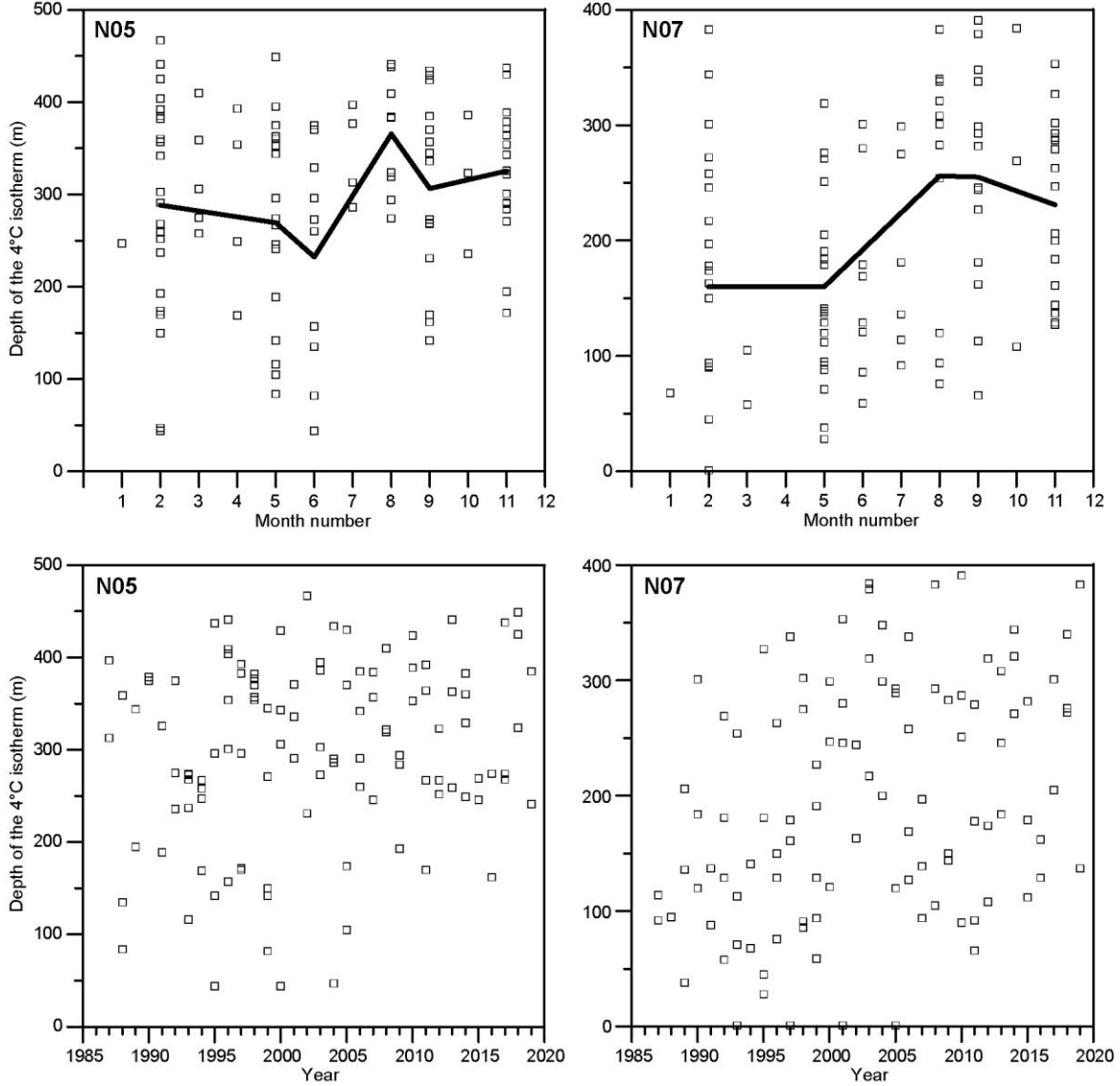
Figure 2.6. Depth of the 4°C-isotherm from CTD observations at N05 and N07 plotted against the month (top panels) and year (bottom panels) of observation. The thick black lines in the top panels show the average isotherm depth for months with at least 10 observations.

To provide a more systematic check and include all the stations that are sufficiently deep, we fit the 4°C-isotherm depth at station number j ($j = 4,...,14$), $D_j(t)$, to a function of time, which combines a linear trend with a sinusoidal seasonal variation:

$$D_j(t) \cong D_{0j} + \gamma_j \cdot t + A_j \cdot cos\left[2\pi \cdot (t - \frac{Day_j}{365})\right] \qquad (2.2)$$

where t is the time in years since 1st January 1993 (the start of satellite altimetry). To establish the fit, we first determine an approximate seasonal variation by ignoring the trend ($\gamma_j = 0$) and regressing $D_j(t)$ on the cosine in Eq. (2.2) where Day_j is varied from 1 to 365 to give maximum correlation. The trend is then found by regressing $D_j(t)$ minus the seasonal variation on time. Finally, $D_j(t)$ is de-trended and the seasonal analysis repeated. The correlation coefficient, R_{Max} (between de-trended $D_j(t)$ and the cosine in Eq. (2.2)) is an indicator of the quality of the fit. This correlation is fairly high for the northernmost stations, but not in the southern part of the section (Table 2.2).

Table 2.2. Total number of CTD profiles at each station (N CTD), number of profiles with surface temperature below 4°C (N<4°C), maximum correlation coefficient (R_{Max}) between 4°C-isotherm depth and the function defined by Eq. (2.2), and the parameters of the fit. Profiles with surface temperature below 4°C are included in the fits with 4°C-isotherm depth set to zero.

Station:	N04	N05	N06	N07	N08	N09	N10	N11	N12	N13	N14
N CTD:	127	133	120	122	117	116	114	110	100	98	100
N<4°C:	0	2	1	5	10	21	25	28	22	26	21
R_{Max} :	0.23	0.25	0.34	0.51	0.47	0.48	0.65	0.66	0.56	0.66	0.67
D_{0j} (m):	375	273	199	145	122	78	58	51	54	47	42
γ_j (m/year):	1.5	2.5	4.7	4.8	2.6	1.4	0.4	0.3	-0.1	0.1	0.6
A_j (m):	24	35	44	66	57	50	48	41	31	35	33
Day_j:	296	287	280	261	266	256	267	263	269	261	259

Both the seasonal and the long-term variations are likely to be linked to changes in the Atlantic water temperature, $T_A(t)$. To test that, Eq. (2.1) was used to assign a value for $T_A(t)$ to each isotherm depth observation and this value was correlated with the isotherm depth. Except for the two ends of the section (N04 and N14), the correlation coefficients were highly significant statistically[1] (Table 2.3). The magnitude of isotherm deepening per degree of warming was determined for each station by regression analyses (Table 2.3) and was highest in the middle of the section (N07). These results are consistent with Figure 2.4.

Table 2.3. Correlation coefficient (R_{Atl}) between 4°C-isotherm depth and Atlantic water temperature, defined by Eq. (2.1) and the isotherm deepening per degree of warming (γ_{Atl}) with 95% confidence limits. Profiles with surface temperature below 4°C are included in the calculations with 4°C-isotherm depth set to zero.

Station:	N04	N05	N06	N07	N08	N09	N10	N11	N12	N13	N14
R_{Atl} :	0.20*	0.28**	0.41**	0.55***	0.48***	0.45***	0.53***	0.53***	0.44***	0.50***	0.08
γ_{Atl} (m/°C):	28±24	53±32	81±34	110±31	86±29	67±25	55±17	46±14	35±14	38±13	2±5

It was noted by Hansen et al. (2019b) that the 4°C-isotherm depths at different stations are fairly well (positively) correlated. A more extensive analysis of this is presented in Table 2.4a, which verifies this, especially for the northern part of the section.

Table 2.4a. Correlation coefficients between 4°C-isotherm depth at different stations measured on the same or neighbouring day.

	N05	N06	N07	N08	N09	N10	N11	N12	N13	N14
N04	0.56***	0.25**	0.24*	0.20	0.23*	0.20*	0.14	0.12	0.08	0.03
N05		0.68***	0.46***	0.31**	0.26**	0.22*	0.11	0.06	0.15	0.09
N06			0.79***	0.36***	0.26**	0.29**	0.26**	0.18	0.30**	0.24*
N07				0.66***	0.51***	0.39***	0.40***	0.32**	0.37***	0.33**
N08					0.79***	0.52***	0.45***	0.33***	0.33**	0.33**
N09						0.68***	0.57***	0.47***	0.41***	0.47***
N10							0.77***	0.55***	0.54***	0.58***
N11								0.83***	0.76***	0.74***
N12									0.79***	0.76***
N13										0.88***

---

[1] Here and elsewhere in the report, statistical significance is indicated by asterixes: * means p < 0.05. ** means p < 0.01. *** means p < 0.001. No asterix means p > 0.05. Significance levels of correlation coefficients have been corrected for serial correlation by the modified Chelton method recommended by Pyper and Peterman (1998).

There is thus a tendency for the 4°C-isotherm to move up- or downwards as a whole over the section, especially its northern part. The question then arises whether this is simply because the isotherm depths at different stations have similar seasonal variations and/or trends. To investigate this question, the isotherm depths have been de-trended and de-seasoned based on Eq. (2.2) and Table 2.2 before correlation. The resulting correlation coefficients (Table 2.4b) are lower, but still fairly high for stations that are not too distant from one another and there are no indications of anticorrelations.

Table 2.4b. Same as Table 2.4a, but after the isotherm depths have been de-trended and de-seasoned.

	N05	N06	N07	N08	N09	N10	N11	N12	N13	N14
N04	0.50***	0.12	0.09	0.06	0.11	0.03	−0.04	−0.01	−0.10	−0.15
N05		0.66***	0.37***	0.20*	0.15	0.09	−0.05	−0.09	−0.00	−0.09
N06			0.72***	0.18	0.07	0.08	0.02	0.01	0.13	−0.01
N07				0.53***	0.32**	0.10	0.13	0.14	0.13	0.03
N08					0.72***	0.32**	0.24*	0.13	0.06	0.06
N09						0.55***	0.38***	0.30**	0.14	0.20
N10							0.59***	0.30**	0.19	0.28*
N11								0.75***	0.60***	0.58***
N12									0.69***	0.66***
N13										0.80***

2.3.3 The gradient layer around the 4°C-isotherm

As the temperature varies, isotherms will move up or down. The amount of vertical isotherm movement in relation to a given temperature change will depend upon the vertical temperature gradient at the location or, equivalently, the vertical distance between isotherms. For the 4°C-isotherm, the distance between the 4.5°C-isotherm and the 3.5°C-isotherm, $\Delta D_4(t)$, should be a fair measure of the appropriate (inverted) temperature gradient.
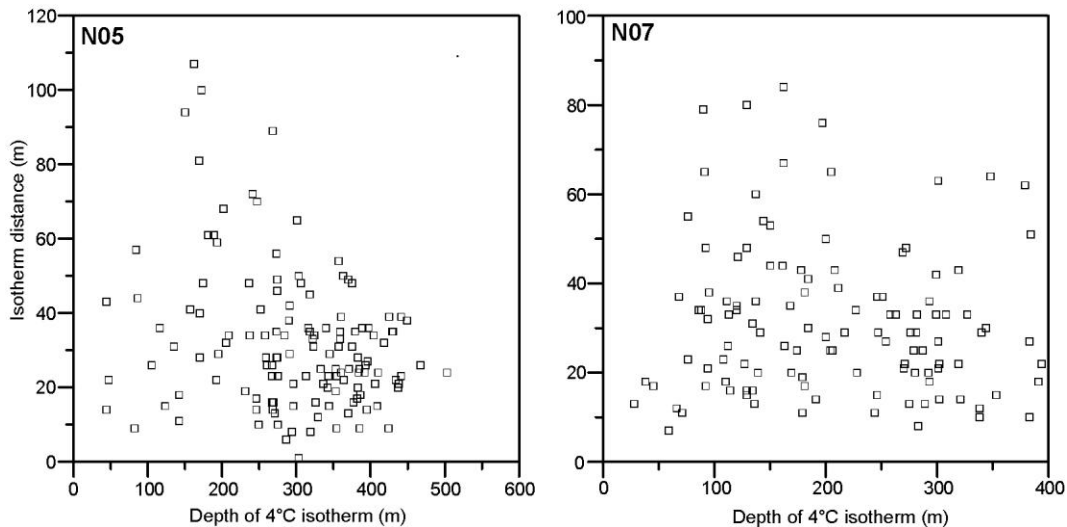
Figure 2.7. The vertical distance between the 4.5°C-isotherm and the 3.5°C-isotherm, $\Delta D_4(t)$, plotted against the depth of the 4°C-isotherm, $D_4(t)$, for sites N05 and N07. For N05, the regression line is drawn and its equation shown in the upper right corner.

The variability of this distance is illustrated in Figure 2.7 where we again have used N05 and N07 as examples. The scatter of values is high for both stations, but they have the same average, 32 m, for

$\Delta D_4(t)$, and this value is almost identically the same for all the stations from N05 to N13 (Table 2.5), with N04 having a lower, and N14 a higher average $\Delta D_4(t)$.

For N05, there is a tendency in Figure 2.7 for $\Delta D_4(t)$ to decrease and become less variable with increasing depth of the 4°C-isotherm. This tendency is verified by a correlation analysis and seems to occur for the four stations from N04 to N07, although weakly (Table 2.5). North of N07, there seems to be the opposite tendency, although again weak.

Table 2.5. Characteristics of the vertical distance between the 4.5°C-isotherm and the 3.5°C-isotherm, $\Delta D_4(t)$, for the sufficiently deep stations, listing the number of CTD profiles at each station with both isotherms in the water column, the average depth (Avg.), and the correlation coefficient (Corr.) between $\Delta D_4(t)$ and the depth of the 4°C-isotherm.

Station:	N04	N05	N06	N07	N08	N09	N10	N11	N12	N13	N14
Number:	127	132	120	115	106	94	79	71	67	64	69
Avg. (m):	29	32	31	32	32	33	32	32	33	33	38
Corr.:	-0.14	-0.26**	-0.24*	-0.08	0.11	0.15	0.04	0.27*	0.22	0.26	0.54***

2.4 Determination of isotherm depth from travel time

As mentioned in the Introduction, preliminary analysis of the observations from the PIES moored at sites N05 and N07 in the 2017-2019 period indicated that the (two-way) travel time measured by the PIES might be a good indicator of the depth of the 4°C-isotherm. A more detailed re-analysis of the PIES data is presented in Chapter 3, but here we discuss the relationship between these two parameters based on the CTD data set.

2.4.1 The relationship between isotherm depth and travel time

The relationship between the depth of the 4°C-isotherm and the (two-way) travel time between the surface and a given depth on the monitoring section was investigated by Hansen et al. (2019b) by using CTD data from the section. For the two standard sites N05 and N07, it was found that the data were fairly well explained (R^2 in Table 2.6) by a second order relationship:

$$D_4(t) \cong \alpha \cdot (\tau(t) - \langle \tau \rangle) + \beta \cdot (\tau(t) - \langle \tau \rangle)^2 + \gamma \qquad (2.3)$$

where $D_4(t)$ and $\tau(t)$ are isotherm depth and travel time at time t, respectively, $\langle \tau \rangle$ is the average travel time for all the profiles, and α, β, and γ are parameters that were fitted by least square multiple regression.

Table 2.6. Number of CTD profiles (N), explained variance (R^2), and values of the four parameters in Eq. (2.3) for various depths at sites N05 and N07 based on CTD profiles in the period 1987-2019. Since only few profiles reach close to the bottom, they are extended from 1281 m depth downwards as described in Hansen et al. (2019b)

Depth	N	R^2	$\langle \tau \rangle$	α	β	γ	N	R^2	$\langle \tau \rangle$	α	β	γ
m			ms	m ms^{-1}	m ms^{-2}	m			ms	m ms^{-1}	m ms^{-2}	m
1690	112	0.92	2302.88	-27.26	-0.79	307.09	105	0.93	2305.87	-30.06	-0.83	205.81
1693	112	0.92	2306.95	-27.25	-0.79	307.09	105	0.93	2309.94	-30.05	-0.83	205.84
1695	112	0.92	2309.66	-27.25	-0.79	307.09	105	0.93	2312.65	-30.05	-0.83	205.82
1700	112	0.92	2316.44	-27.24	-0.79	307.12	105	0.93	2319.44	-30.04	-0.83	205.82

(Table 2.6 columns: "N05" spanning first group, "N07" spanning second group)

In Hansen et al. (2019b), the parameters of the fit were derived assuming a depth of 1693 m, but most of the parameters are not very sensitive to the exact depth (Table 2.6). Within a depth interval of 10 m

(1690-1700), only the average travel time, $\langle\tau\rangle$, is seen to vary significantly and its variations are consistent with an average sound speed of 1475 m s^{-1}. As long as the depth is close to 1693 m, the only parameter that needs to be adjusted when the depth is changed is therefore $\langle\tau\rangle$ and adjustment of this parameter is the critical step in calibration of PIES data for a given deployment.

2.4.2 The effect of variable Atlantic water temperature

In deriving the parameters of Eq. (2.3), no account was taken of temporal water mass changes, but the Atlantic water has varied in temperature as well as salinity over the period of the CTD profiles (1987-2019) as well as seasonally, whereas the deeper water masses have varied much less. This might affect the relationship, especially for site N05 where the Atlantic layer is deep.

To check this, we correlate the Atlantic water temperature, $T_A(t)$, defined by Eq. (2.1), with the difference between the isotherm depth observed and the depth fitted by Eq. (2.3), where we have used the modified values for the parameters ($a_T = 0.57°C$ and $t_{Max} = 247$). For N05, the correlation coefficient was found to be significant (R = -0.42*). Thus the fit in Eq. (2.3) may be improved by adding a term:

$$D_4(t) \cong \alpha \cdot (\tau(t) - \langle\tau\rangle) + \beta \cdot (\tau(t) - \langle\tau\rangle)^2 + \gamma + \delta \cdot (T_A(t) - 8.25°C) \quad (2.4)$$

with δ = -21.1 m °C^{-1} determined by linear regression. As seen in Table 2.7, using Eq. (2.4) instead of Eq. (2.3) for site N05 reduced the standard deviation of the difference between observed and fitted isotherm depth by 10% and reduced the largest positive deviation from 79 m to 67 m, although it had almost no effect on the largest negative deviation. A similar analysis was made for site N07, but there the correlation between $T_A(t)$ and the difference between the isotherm depth observed and the depth fitted by Eq. (2.3) was almost zero (R = -0.02) and not significant. Consistent with that, Table 2.7 shows no improvement in using Eq. (2.4) rather than Eq. (2.3) for N07.

Table 2.7. Performance of the two fits, Eq. (2.3) and Eq. (2.4) for sites N05 and N07 based on CTD profiles 1987-2019. The table lists the standard deviation of the difference, ΔD, between observed and fitted isotherm depth ($\Delta D = D_{Obs} - D_{Fit}$), as well as the most negative difference, ΔD_{Low}, and the most positive difference, ΔD_{High}.

Fit	N05			N07		
	Std.dev.	ΔD_{Low}	ΔD_{High}	Std.dev.	ΔD_{Low}	ΔD_{High}
Eq.(2.3)	28.4m	-73.6m	79.2m	27.4m	-81.5m	62.4m
Eq.(2.4)	25.8m	-74.0m	67.0m	27.4m	-81.7m	62.5m

The performances of the two fits are illustrated in Figure 2.8 for both sites. In this figure, the open squares show observed isotherm depth plotted against travel time and they are seen to fit well to the expression given by the right side of Eq. (2.3). The red squares are observed isotherm depth minus the last term in Eq. (2.4). Generally, the red squares seem to fit a bit better to the continuous line for site N05, consistent with Table 2.7. For N07, most of the red squares are on top of the open squares indicating that the last term in Eq. (2.4) gives little improvement, again consistent with Table 2.7. An attempt was made to see whether further improvement could be gained by including a term with salinity variations analogous to the last term in Eq. (2.4), but no significant improvement was found.
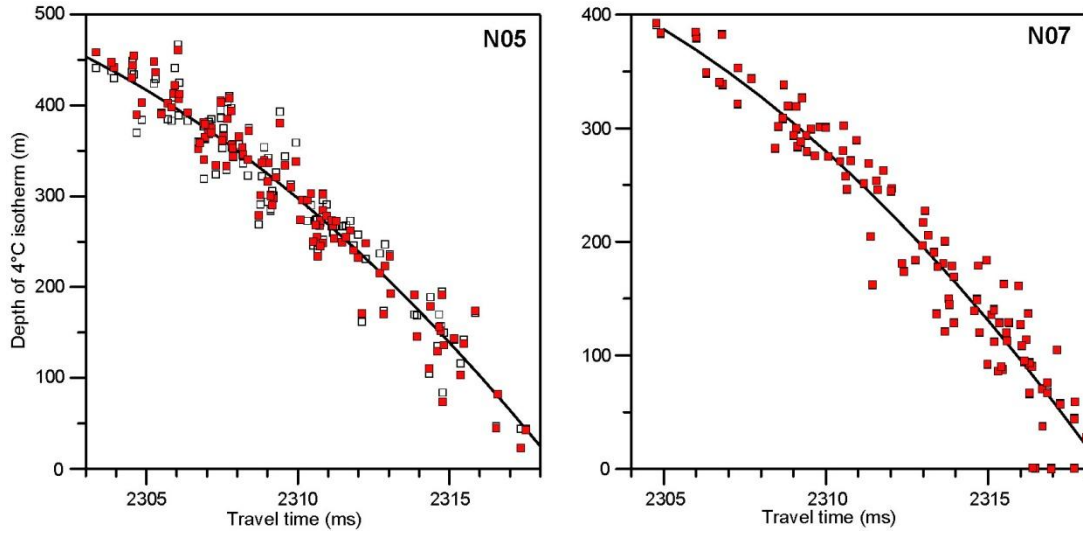
Figure 2.8. Depth of the 4°C-isotherm plotted against travel time for sites N05 and N07 assuming a bottom depth of 1695 m. Each open square represents a CTD profile. For the red squares, the last term in Eq. (2.4) has been subtracted from the observed isotherm depth. Continuous lines indicate the fits according to Eq. (2.3).

3 Isotherm depth from PIES measurements

In 2017, two PIES (Pressure Inverted Echo Sounders) were deployed on the monitoring section in cooperation with the University of Hamburg. The PIES were deployed at two of the long-term CTD standard stations, N05 and N07, and collected data until they were recovered in June 2019 (Table 3.1). A preliminary analysis of the data indicated that PIES would be a good tool for future monitoring (Hansen et al., 2019b), but the analysis also demonstrated that the PIES data were heavily contaminated by errors. In the present report, the data will be passed through a more detailed quality control and different methods for averaging will be tested.

Figure 3.1. One of the PIES (P-269) that was used in the 2017-2019 experiment. The PIES is mounted on an anchor frame and deployed on the bottom. The measurements are stored in the instrument and may be uploaded to a research vessel acoustically or retrieved after the PIES has been released from the frame and recovered.

It is not the intention in this report to repeat all the results from the preliminary analysis. Interested readers are referred to the technical report describing the results (Hansen et al., 2019b). Some of the main findings will, however, be repeated to provide a background for the further analysis.

Table 3.1. PIES data characteristics. For each of the PIES, the table lists the measurement period, the number of hours, the number of complete days, average values for bottom pressure (P_B) and for travel time (τ).

Site	YYYY/MM/DD HH – YYYY/MM/DD HH	Hours	Days	Average P_B	Average τ
N05	2017/08/31 11 – 2019/06/08 11	15505	645	1728.66 dbar	2309.14 ms
N07	2017/10/21 07 – 2019/06/08 15	14289	594	1727.58 dbar	2310.17 ms

3.1 The PIES pressure data

Each of the PIES measured pressure - interpreted as bottom pressure, p_B – every thirty minutes during the deployment. The pressure data indicated slow increases during the deployment period (Figure 3.2), which are assumed to be due to instrumental drift. On daily and longer time scales, the pressure seems to vary both from sea level changes and from changes in the hydrographic structure, but hourly variations appear to be tidal and are assumed to be mainly caused by tidal sea level variations (Figure 3.2).
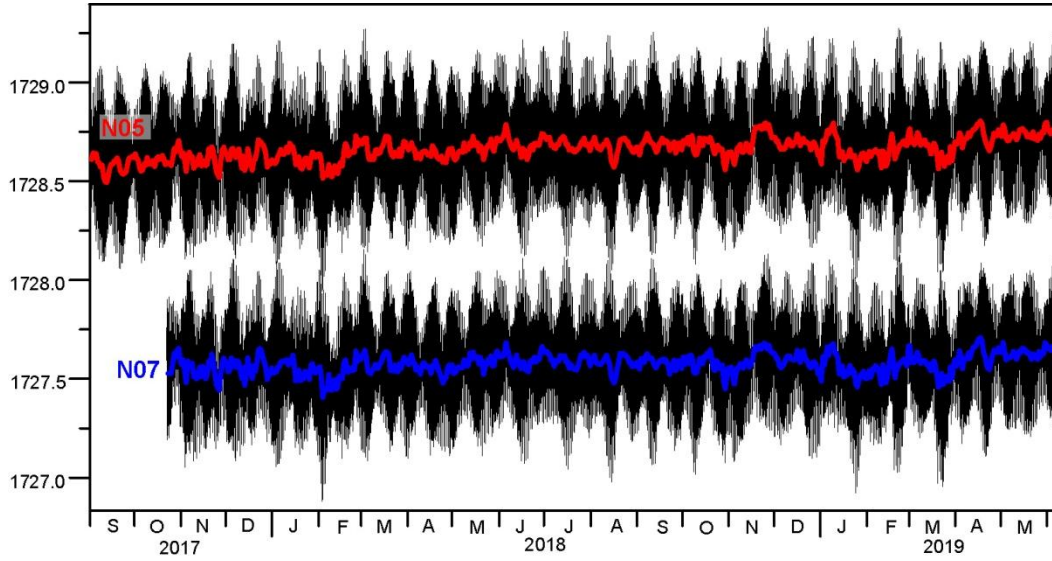
Figure 3.2. Bottom pressure measured by the two PIES through the deployment period. Thin black lines show raw (half-hourly) values. Thick coloured lines show daily averaged values. Based on Hansen et al. (2019b).

3.2 Processing of PIES travel time measurements

3.2.1 Correcting for sea level changes

The relationships between travel time and isotherm depth (Chapter 2) were made on the assumption that sea level height, *h(t)*, is constant and zero. This is not the case in reality and we need to correct for that to the extent possible. Partly, we do that by utilizing the pressure, *p(t)*, measured by the PIES. If the pressure measurements were exact and independent of the hydrography, we could use the relationship:

$$\Delta p(t) = g \cdot \rho_0 \cdot h(t) \qquad (3.1)$$

where $\Delta p(t)$ would be the pressure deviation from its average value during the deployment. In reality, the pressure sensors drift and the hydrography changes also, but both of these are fairly slow, as compared to the hourly travel time measurements. We therefore split *h(t)* into two components, a daily average, $h_D(t)$, and the hourly deviation from this, $\Delta h(t)$. For the daily average, we then use altimetry data whereas the hourly deviation is derived from the pressure data:

$$\Delta h(t) = \frac{1}{g \cdot \rho_0} \cdot [p(t) - \langle p(t) \rangle_D] \qquad (3.2)$$

where $\langle p(t) \rangle_D$ is daily averaged pressure. In the further data processing, corrected travel time, τ, is used, which is derived from the raw value, τ_{Raw}, by using sound velocity, *c*, in the surface (assumed to be 1500 m s^{-1}):

$$\tau = \tau_{Raw} - \frac{2}{c} \cdot [h_D + \Delta h] \qquad (3.3)$$

3.2.2 Errors in travel time measurement

The purpose of the travel time measurements of the PIES is to measure the (two-way) travel time between the PIES and the surface, but the returning echo often comes from within the water column rather than the

surface, although a "lockout time" limits this. To reduce the erroneous values caused by "false echoes", a window, the "τ-window", is defined and all τ-values outside of this are ignored. Since both PIES were at approximately the same depth, the same boundaries (2295 – 2330 ms) were used for the two τ-windows (Figure 3.3).
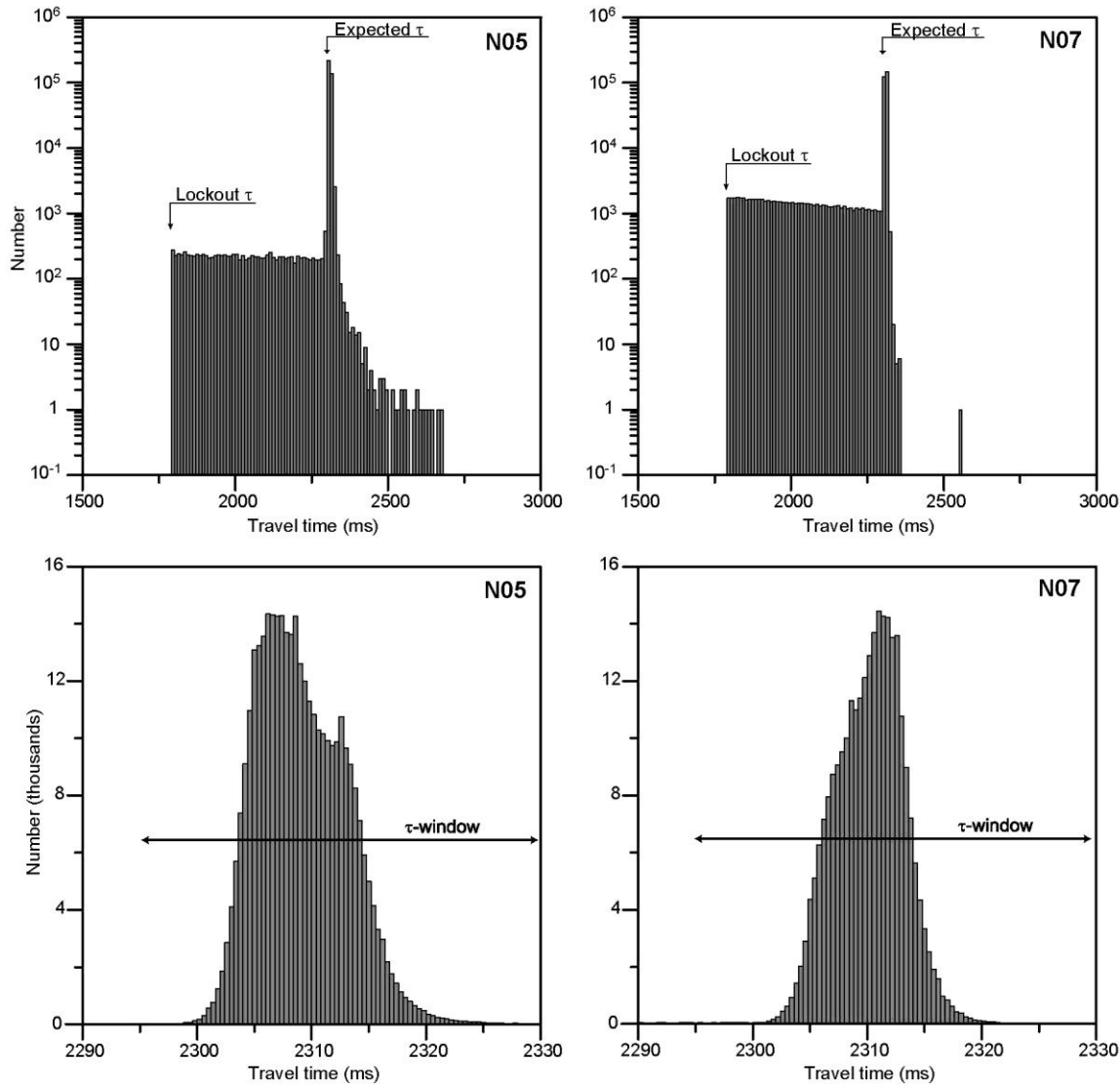
Figure 3.3. Histograms of travel time measurements by the two PIES for a wide interval (upper panels, note logarithmic scale) and for an interval around the expected values of τ (lower panels, note linear scale). In the upper panels, the lockout time and the expected travel time are indicated. In the lower panels, the chosen τ-window is indicated. Based on Hansen et al. (2019b).

For the PIES at N05, 11805 of the total 372120 pings were outside the τ-window and were excluded. This amounts to 3%. For N07, 71524 of the total 342936 were excluded, equivalent to 21%. The exclusion of these values means that some hours had less than 24 pings and that some days had less than 576 (24×24) pings. This is especially notable for the N07 travel time data (Figure 3.4). Consistent with this, the lowest number of τ-values per day was 317 for N05 and 254 for N07. For the number of τ-values per hour, the lowest number was 2 for N07, whereas there was one hour at N05 with no accepted τ-values.

This occurred on the day (7th Dec 2017) when there were only 317 accepted τ-values for the whole day (Figure 3.5). On that same day, there were 7 hours with less than 10 accepted τ-values and the day before also had several hours with reduced number of τ-values. This emphasizes the need to take the number of accepted τ-values into account when averaging and is the reason that the hourly τ-values are weighted before computing daily averages.
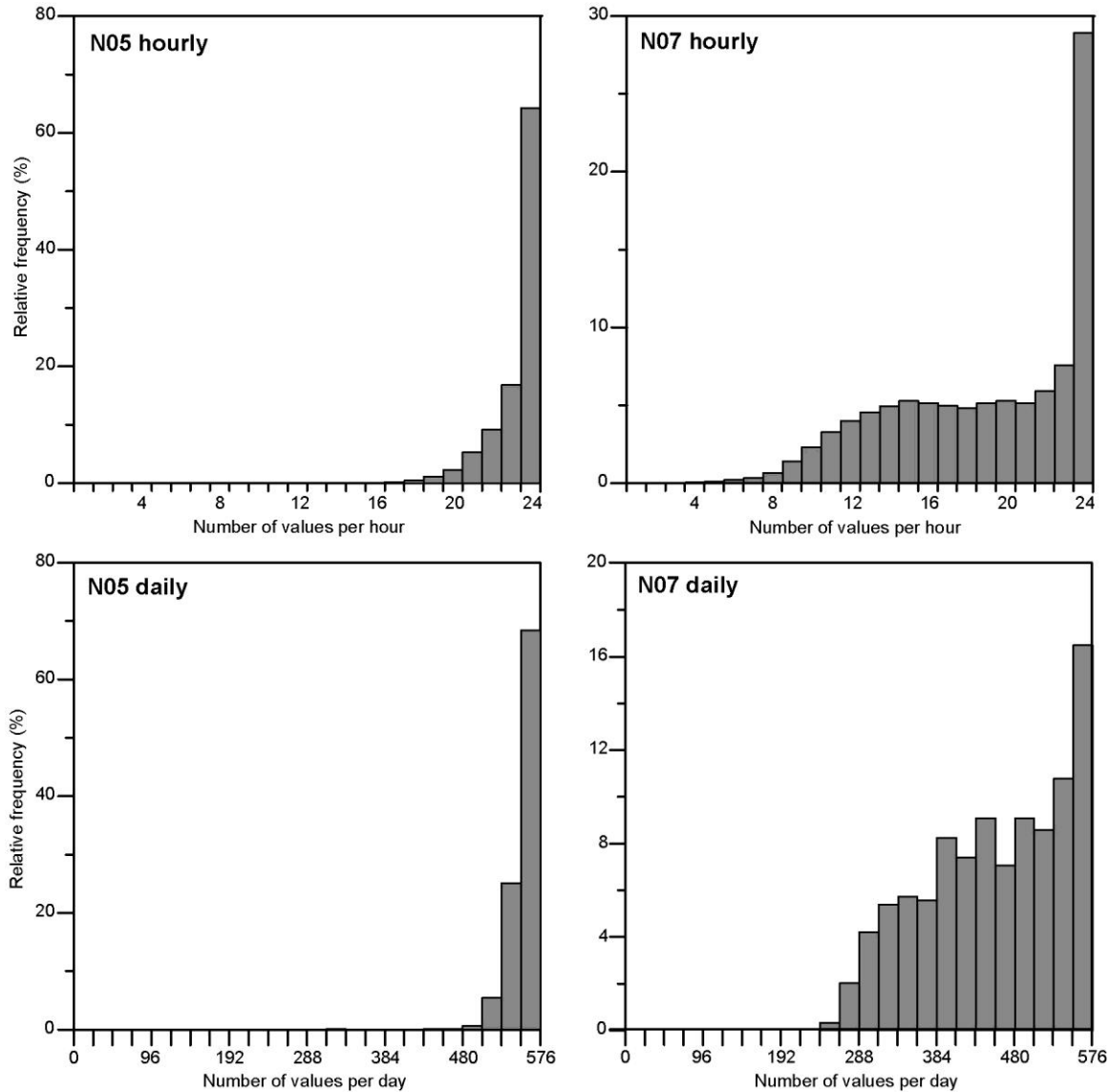
Figure 3.4. Relative occurrence of hours (top panels) and days (bottom panels) with various number of accepted τ-values (those that passed through the τ-window, Figure 3.3).

Even when the returning echo is from reflection at the surface, additional uncertainty is, however, introduced by the pulse duration. As seen in Figure 3.3, the useful range of travel time, τ, is on the order of 10-15 ms, whereas each pulse (ping) has a duration of 6 ms. Even for a fixed distance between PIES and surface, the recorded travel time may therefore vary depending on where on the returning echo pulse the counting is triggered. Fortunately, the PIES are designed so that they emit 24 pings in bursts every hour. This allows estimates with better statistical significance, but the distribution of recorded τ-values for

every hour is not symmetrical. Rather, it is skewed to higher values - longer travel time – (Kennelly et al., 2007), which makes the best method to estimate τ less obvious. In the "Inverted Echo Sounder Data Processing Manual" (Kennelly et al., 2007), it is recommended to use the rising front edge of the τ distribution for every hour to determine the τ-value for that hour. Below, we discuss methods for deriving hourly as well as daily values for travel time.

3.2.3 Estimating hourly travel time values

We have tested three different methods for estimating hourly travel time, which all are based on the description given by Kennelly et al. (2007) in the "Inverted Echo Sounder Data Processing Manual", although slightly modified.

After correcting for sea level and rejecting values outside the τ-window, the number of τ-values for each hour may vary between 0 and 24. In the first stage, the measurements in each burst are sorted and the first quartile value is calculated. For hours without any accepted measurements, the value is set equal to the value for the previous hour. This value is denoted "Tau-Qu1".

These hourly values are then smoothed with a 5 hour median filter (rather than the 4 hour median filter used by Kennelly et al. (2007) in order to make it symmetric). The output from this filter is denoted "Tau-Med".

The travel time measurements within each hourly burst are then windowed with an asymmetric window about these filtered values going from Tau-Med minus 5 ms to Tau-Med plus 2.5 ms. The n (0 – 24) measurements which fall within this asymmetric window are sorted and the first quartile is found for the n travel time measurements in each hourly burst. Next the n/6 travel times nearest the quartile value are averaged to obtain the third estimate of hourly travel time, denoted "Tau-Qu2".

Table 3.2. Average values and standard deviations (both in ms) for hourly travel time processed by the three different methods described.

Parameter	Site N05 (155505 hours)			Site N07 (14289 hours)		
	Tau-Qu1	Tau-Med	Tau-Qu2	Tau-Qu1	Tau-Med	Tau-Qu2
Average:	2307.73	2307.73	2307.66	2308.99	2309.00	2308.99
Std.dev.:	3.32	3.29	3.32	2.49	2.44	2.48

Averages of the hourly values for the whole deployment period are very similar as derived by the three different methods and standard deviations are also similar (Table 3.2). When we compare values from individual hours, we find high correlation coefficients, but there are clear differences between the methods, especially when focusing on the minimum or maximum differences (Table 3.3).

Table 3.3. Characteristics of the differences between hourly travel time processed by the three different method (all in ms) and correlation coefficients between them.

Site	Variable	Difference				Correlation
		Average	Std.dev.	Minimum	Maximum	
N05	(Tau-Qu1)-(Tau-Med):	0.00	0.41	-10.87	6.48	0.993
N05	(Tau-Qu1)-(Tau-Qu2):	0.07	0.30	-10.87	6.35	0.996
N05	(Tau-Med)-(Tau-Qu2):	0.07	0.36	-1.87	4.94	0.994
N07	(Tau-Qu1)-(Tau-Med):	-0.01	0.43	-6.44	3.30	0.985
N07	(Tau-Qu1)-(Tau-Qu2):	0.00	0.30	-6.98	5.74	0.993
N07	(Tau-Med)-(Tau-Qu2):	0.01	0.40	-1.88	3.87	0.987

3.2.4 Estimating daily travel time values

Most commonly, the PIES data will be used for time scales of a day or longer and daily averaged travel time will be the basic data set for further analysis. Due to the high error frequency and the skewed distribution, it is not obvious, however, which is the best way to generate the daily averages. We have

therefore tested four different methods for estimating these. The first two methods combine all the (sea-level corrected) τ-values for each day into one set, which is then analyzed. The last two methods use the hourly values discussed above so that the value for each day is the average of all the (up to 24) hourly values, but weighted with the number of accepted τ-values for each hour.

- **Method 1**, which is included mainly as a benchmark, produces a simple average of all the (sea-level corrected) τ-values that passed through the τ-window for that day.

- **Method 2** also produces a simple average and uses the same basic data set as Method 1, but before averaging, an automatic error correcting routine is run, during which 200 τ-values are error flagged and excluded from the averaging. This routine is structured as 200 iterations. During each iteration, that τ-value, which deviates most from the average, is excluded.

- **Method 3** produces daily (weighted) averages based on the hourly "Tau-Med" values.

- **Method 4** produces daily (weighted) averages based on the hourly "Tau-Qu2" values.

Results from the four methods are compared in Table 3.4 and Table 3.5. When comparing average travel times for the whole deployment (Table 3.4), Method 2 is seen to have considerably lower τ-average than Method 1. With a skew distribution, this was to be expected, since the iterative error correction in Method 2 will tend to remove high values preferentially. We would also have expected Methods 3 and 4 to have lower averages since they are using the rising edge (first quartile) of the τ-distribution, rather than an arithmetic mean as in Methods 1 and 2. The standard deviations in Table 3.4 do not show any obvious differences between the four methods, but the table also includes values for two other parameters:

$$Noise = \sqrt{\frac{\sum[\tau_i - \frac{1}{2}(\tau_{i-1} + \tau_{i+1})]^2}{n-2}} \qquad Max.dev. = Max[|\tau_i - \frac{1}{2}(\tau_{i-1} + \tau_{i+1})|] \qquad (3.4)$$

where τ_i (i = 1,…,n) are all the τ-values for the day. Both of the parameters in Eq. (3.4) measure the difference in τ-value for a day from that of the two neighbouring days and it seems reasonable to use minimum values for both parameters as indications of high quality. Thus, it was not unexpected that Method 1 had the highest values for both parameters for N05 (Table 3.4). For N07, Method 1 actually had the lowest "Noise" value, but the highest "Max-dev." value. Except for excluding Method 1 (as expected), Table 3.4 does not indicate any of the methods as much better than the others.

Table 3.4. Average values, standard deviations, "Noise", and "Max.dev.", defined by Eq. (3.4), (all in ms) for daily travel time processed by the four different methods described.

Parameter	Site N05 (645 days)				Site N07 (594 days)			
	Meth.-1	Meth.-2	Meth.-3	Meth.-4	Meth.-1	Meth.-2	Meth.-3	Meth.-4
Average:	2309.02	2308.22	2307.70	2307.63	2310.05	2309.60	2309.00	2309.01
Std.dev.:	3.24	3.24	3.24	3.25	2.41	2.43	2.41	2.42
Noise:	0.82	0.76	0.74	0.75	0.46	0.53	0.47	0.50
Max.dev.:	5.18	3.23	3.76	3.41	2.99	2.53	2.18	2.34

A different approach is pursued in Table 3.5, which compares the four methods pair-wise. Perhaps not surprisingly, Methods 3 and 4 produce the most similar results. If the standard deviation of the difference in daily τ-value is used as criterion for average deviation, then Methods 2, 3, and 4 only deviate by about

0.3 ms, equivalent to ≈10 m in isotherm depth (Figure 2.8). For individual days, the difference may, however be much higher as shown by the minimum and maximum values in Table 3.5.

Table 3.5. Characteristics of the differences between daily travel time processed by the four different methods (all in ms) and correlation coefficients between them.

Site	Variable	Difference				Correlation
		Average	Std.dev.	Minimum	Maximum	
N05	(Meth.-1)-(Meth.-2):	0.80	0.34	-0.57	5.56	0.995
N05	(Meth.-1)-(Meth.-3):	1.32	0.34	0.69	4.21	0.995
N05	(Meth.-1)-(Meth.-4):	1.39	0.46	0.63	5.55	0.990
N05	(Meth.-2)-(Meth.-3):	0.52	0.27	-1.38	1.94	0.997
N05	(Meth.-2)-(Meth.-4):	0.59	0.33	-0.05	2.20	0.995
N05	(Meth.-3)-(Meth.-4):	0.07	0.14	-0.12	1.34	0.999
N07	(Meth.-1)-(Meth.-2):	0.45	0.23	-0.59	1.46	0.996
N07	(Meth.-1)-(Meth.-3):	1.04	0.19	0.67	2.64	0.997
N07	(Meth.-1)-(Meth.-4):	1.04	0.27	0.64	3.43	0.994
N07	(Meth.-2)-(Meth.-3):	0.60	0.29	0.02	2.29	0.993
N07	(Meth.-2)-(Meth.-4):	0.60	0.34	0.08	2.55	0.990
N07	(Meth.-3)-(Meth.-4):	0.00	0.10	-0.16	0.80	0.999

To illustrate the different methods for estimating daily averaged τ-values, Figure 3.5 shows the values at N05 during the month of December 2017, which includes the day (Dec. 7th), with the lowest number of accepted pings for this site as indicated by the dashed line in the figure. To a large extent, the curves in the figure are parallel with biases consistent with the averages in Table 3.4. On special occasions, notably on Dec 7th, there are larger differences, which seem to be associated with an increased number of erroneous τ-values. A priori, we do not know, however, what the correct τ-value would be during these extreme events, and so it is difficult to use this as a criterion to choose between methods.
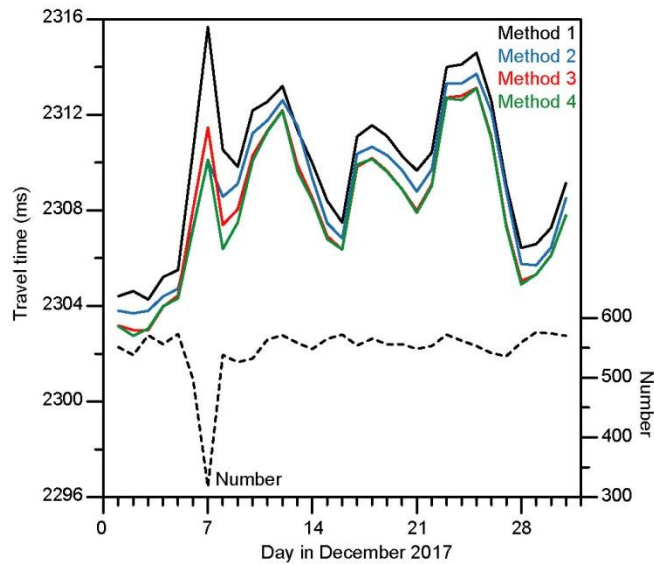
Figure 3.5. Daily averaged travel time (left scale) at N05 produced by the four listed methods for the month of December 2017. The dashed curve shows the number of accepted τ-values for each day (right scale).

3.2.5 Calibrating the PIES data for isotherm depth determination

Since we know the depths of the two PIES within a few meters, most of the parameters in Eq. (2.3) are known, as listed in Table 2.6. The one unknown parameter is $\langle\tau\rangle$, which requires knowledge of the exact depths of the sound transducers of the two PIES within a few centimeters (relative to the zero level of altimetry) for its values to be determined from the historical CTD data set. Two strategies may be adopted for choosing the appropriate value for $\langle\tau\rangle$.

The first strategy is to use one of the values for average τ measured by the PIES (Table 3.2 or Table 3.4). Since we will focus on daily averaged values for the isotherm depth, the chosen value should be from Table 3.4, but will depend on, which of the four methods is used (Sect. 3.2.4). Use of this method presupposes, however, that average 4°C-isotherm depth during the PIES deployment period (2017-2019) equals the average isotherm depth based on the more than hundred CTD profiles, each one of which is a snapshot from the period 1987-2019.

The second strategy involves using the CTD observations made during the PIES deployment period to determine appropriate values for $\langle\tau\rangle$ at the two sites. To implement this strategy, the CTD profile from each cruise is used to calculate the (two-way) travel time, τ_{1695}, down to 1695 m depth - using the method for extending profiles below 1281 m described in Hansen et al. (2019b). This value is compared to the travel time measured by the PIES at the time of the CTD profile, τ_{PIES}, and the difference, $\Delta\tau$, determined:

$$\Delta\tau \equiv \tau_{PIES} - \tau_{1695} \qquad (3.5)$$

The value of $\Delta\tau$ at one of the sites may vary from one cruise to another, but also depends on, which one of the three hourly or four daily averaging methods is used, as summarized in Table 3.6. From the discussion in Sect. 3.2.3 and Sect. 3.2.4, none of the methods showed any clear advantage over the others, except that Method-1 was scrapped, as expected. If the measurements were perfect, the $\Delta\tau$ values at one site ought to be the same for all the cruises when determined with the same method. From that, it seems reasonable to prefer the method with the lowest standard deviation and/or the lowest maximum deviation (excluding daily average by Method-1, as previously argued).

The methods that do minimize these deviations are underlined and bold in Table 3.6. For N05, the hourly estimates based on the 5-hour median, Tau-Med, have both the lowest standard deviation and the lowest maximum deviation (bottom two rows in Table 3.6). For N07, the message is less clear, but the averages based on the median had lowest deviations for hourly values (Tau-Med) and the lowest maximum deviation for daily values (Method-3).

Table 3.6. Travel time calibration data based on five CTD cruises in the PIES deployment period. For each cruise and PIES site, the table lists the travel time offset, $\Delta\tau$, defined by Eq. (3.5) (in ms) for each of the four methods to calculate daily averages ("Mt-1" = "Method-1", etc.) and each of the three methods to calculate hourly averages ("T-Qu1" = "Tau-Qu1", etc.). The three bottom rows list the average $\Delta\tau$, the standard deviation, and the maximum deviation (numerically) from the average for each of the seven methods for each site. The CTD profiles are extended to 1695 m depth as described in Hansen et al. (2019b). The smallest standard deviations and maximum deviations for each site are in bold and underlined.

| | N05 | | | | | | | N07 | | | | | | |
| | Daily Δτ | | | | Hourly Δτ | | | Daily Δτ | | | | Hourly Δτ | | |
Cruise	Mt-1	Mt-2	Mt-3	Mt-4	T-Qu1	T-Med	T-Qu2	Mt-1	Mt-2	Mt-3	Mt-4	T-Qu1	T-Med	T-Qu2
1802:	0.25	-0.13	-1.31	-1.43	-1.51	-0.91	-1.85	-2.28	-2.61	-3.54	-3.56	-4.46	-3.83	-4.16
1821:	0.78	0.00	-0.20	-0.16	-0.72	-0.72	-0.49	-1.87	-2.43	-2.77	-2.74	-3.01	-2.70	-2.80
1838:	-0.34	-1.23	-1.52	-1.53	-1.70	-1.18	-1.59	-2.36	-2.82	-3.31	-3.29	-2.93	-2.93	-2.90
1902:	0.33	-0.40	-0.87	-0.92	-1.60	-1.43	-1.68	-1.30	-2.00	-2.53	-2.49	-3.25	-3.20	-3.33
1919:	0.09	-0.74	-1.03	-1.01	-0.60	-0.82	-0.94	-2.31	-2.94	-3.26	-3.19	-3.74	-3.52	-3.59
Average :	0.22	-0.50	-0.99	-1.01	-1.23	-1.01	-1.31	-2.02	-2.56	-3.08	-3.05	-3.48	-3.24	-3.36
Std.dev.:	0.41	0.50	0.51	0.54	0.52	**0.29**	0.57	0.45	**0.37**	0.42	0.43	0.63	0.45	0.55
Max.dev.:	0.56	0.73	0.79	0.85	0.63	**0.42**	0.82	0.72	0.56	**0.55**	0.56	0.98	0.59	0.80

Based on this, we will in the following use these two (Tau-Med and Method-3) methods for further processing of the PIES data and the chosen value for $\Delta\tau$ is determined as the mean of the two estimates (hourly and daily) in Table 3.6: -1.00 ms for N05 and -3.16 ms for N07. The values for $\langle\tau\rangle$ to use in Eq. (2.4) are then found by adding these values for $\Delta\tau$ to the values, $\langle\tau\rangle_{1695}$, for 1695 m depth in Table 2.6:

$$\langle\tau\rangle = \langle\tau\rangle_{1695} + \Delta\tau \qquad (3.6)$$

The resulting values for $\langle\tau\rangle$ (Table 3.7) are somewhat higher than the values for Tau-Med in Table 3.2 and for Method-3 in Table 3.4, equivalent to differences in 4°C-isotherm depth of ≈25 m for N05 and ≈15 m for N07. Such a difference in average isotherm depth between the PIES deployment period and the CTD snapshots from the 1987-2019 period does not seem unreasonable, especially taking into account the effect of varying Atlantic water temperature (Sect. 2.1).

Table 3.7. Parameters to use in Eq. (2.4) to calculate 4°C-isotherm data based on the Tau-Med method for daily averages and Method-3 for daily averages.

	N05					N07			
$\langle\tau\rangle$	α	β	γ	δ	$\langle\tau\rangle$	α	β	γ	δ
ms	$m \cdot ms^{-1}$	$m \cdot ms^{-2}$	m	$m \cdot (°C)^{-1}$	ms	$m \cdot ms^{-1}$	$m \cdot ms^{-2}$	m	$m \cdot (°C)^{-1}$
2308.66	−27.25	−0.79	307.09	−21.1	2309.49	−30.05	−0.83	205.82	0

3.2.6 Validating isotherm depths determined from PIES data

To evaluate the ability of PIES data to generate values for isotherm depth, Figure 3.6 compares the 4°C-isotherm depths determined from CTD profiles during the PIES deployment period with the values determined from the PIES data. The same CTD profiles were also used to calibrate the PIES data (Sect. 3.2.5) so, averages based on all the cruises should be similar, but the comparisons are much better than that for both N05 and N07 (Figure 3.6).
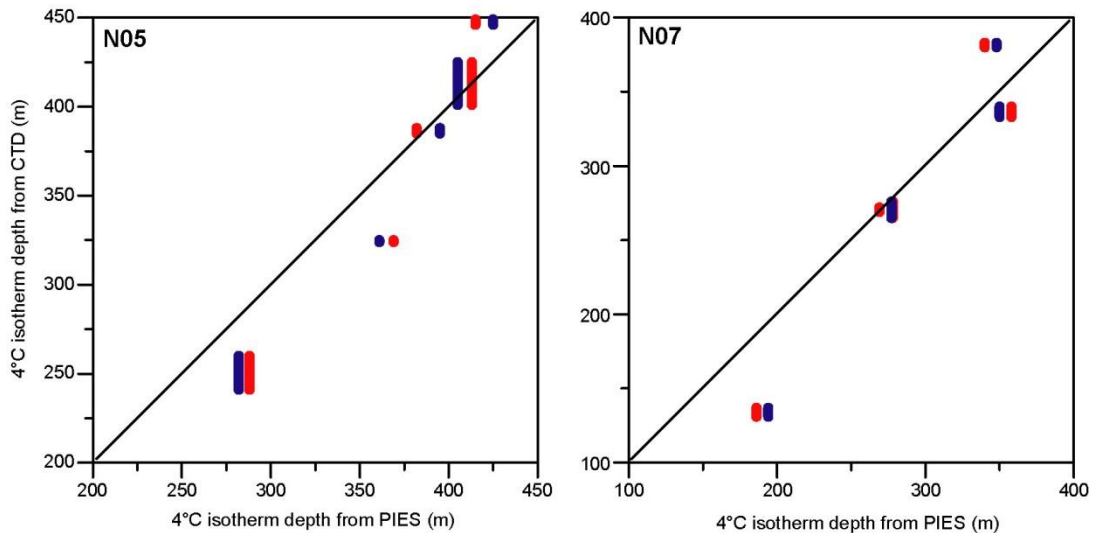
Figure 3.6. Comparison of 4°C-isotherm depth as observed by CTD and as calculated from PIES data. Coloured vertical lines indicate the span between down- and up- CTD profiles. Red lines show the isotherm depths based on daily averaged PIES from the same day as the CTD profiles, whereas the blue lines are from hourly averages for the same hour as the CTD.

If we use the (down- versus up-) CTD profile that fits best with the PIES data, the (numerical) average difference between the two methods was 24 m for N05 and 22 m for N07, when using daily averaged PIES data. Using hourly averaged PIES data gave slightly smaller differences. It is not obvious, how much of these differences is due to uncertainty in the PIES-derived isotherm depths since the depths may change appreciably over a day (Figure 3.7). On average, the numerical difference between the isotherm

depth on one day and the next was 24 m at N05 and 17 m at N07 according to the daily averaged PIES data.

3.3 Characteristics of isotherm depths determined from PIES data

The depth of the 4°C-isotherm based on daily averaged PIES data during the whole deployment period of each of the PIES shows some similarity between the two sites (Figure 3.7). At both sites, there are abrupt changes of isotherm depth and they often seem to occur synchronously, but not always.
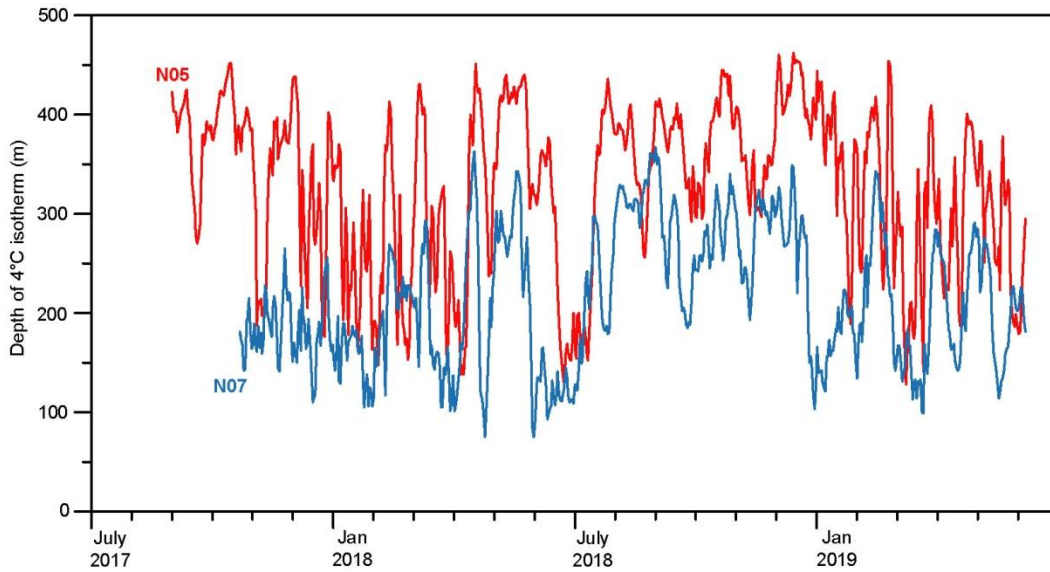
Figure 3.7. Daily averaged depth of the 4°C-isotherm at N05 (red) and at N07 (blue) based on the PIES data.

4 Isotherm depth from ADCP measurements at site NB

Since the beginning of ADCP measurements on the monitoring section, deployments have been made at several sites along the section (Hansen et al., 2003; 2015), but the best covered ADCP site is site "NB". At this site, there was one deployment from October 1994 to February 1995, but then there was a pause, until the regular deployments started in June 1997. From that time, it has been attempted to keep this site instrumented, except for annual servicing periods that typically have lasted 3 weeks (Table 4.1).

From summer 1994 to summer 2019, there have altogether been 25 deployments at site NB with a total of 7606 days (Table 4.1). Counting from the time of regular monitoring in June 1997 until the end of the last deployment so far in May 2019, an ADCP has been at site NB 94% of the time.

Table 4.1. ADCP deployments at site NB listing deployment id (Deploym.), position, bottom depth (Botm), period, duration (Dur.), bin length (Lgt), last (highest) bin, and Top bin, which is the highest bin with 100% good daily averaged data. The last three columns list the depths of the deepest bin (Bin1), the highest bin (Last), and the highest bin with 100% good data (Top).

| Deploym.	Position		Botm	Period	Dur.	Bins			Depths(m)		
	Lat.	Long.	(m)	yyyymmdd-yyyymmdd	Days	Lgt	Last	Top	Bin1	Last	Top
NWNB9410	62.9181	-6.0772	962	19941023-19950216	117	25	23	21	624	74	124
NWNB9706	62.9136	-6.0826	907	19970614-19980612	364	25	23	18	623	73	198
NWNB9807	62.9193	-6.0807	961	19980705-19990618	349	25	25	20	672	72	197
NWNB9907	62.9169	-6.0875	947	19990703-19990706	4	25	24	24	669	94	94
NWNB9908	62.9189	-6.0842	957	19990821-20000615	300	25	25	19	679	79	229
NWNB0007	62.9184	-6.0837	954	20000708-20010615	343	25	24	19	676	101	226
NWNB0107	62.9210	-6.0852	980	20010707-20020614	343	25	25	19	702	102	252
NWNB0207	62.9211	-6.0853	981	20020706-20030613	343	25	25	21	703	103	203
NWNB0307	62.9171	-6.0852	955	20030706-20040610	341	25	24	20	665	90	190
NWNB0407	62.9214	-6.0817	987	20040703-20050519	321	25	25	20	697	97	222
NWNB0506	62.9174	-6.0841	956	20050612-20060126	229	25	23	19	666	116	216
NWNB0602	62.9157	-6.0900	942	20060217-20060521	94	25	19	18	652	202	227
NWNB0606	62.9080	-6.0827	958	20060610-20070517	342	25	22	19	669	144	219
NWNB0706	62.9166	-6.0828	955	20070609-20080517	344	25	23	20	666	116	191
NWNB0806	62.9183	-6.0867	953	20080607-20090514	342	25	23	19	664	114	214
NWNB0906	62.9183	-6.0850	959	20090606-20100513	342	25	23	20	670	120	195
NWNB1006	62.9177	-6.0858	961	20100605-20110519	349	25	23	18	672	122	247
NWNB1106	62.9158	-6.0834	951	20110611-20120519	344	25	23	17	662	112	262
NWNB1206	62.9200	-6.0800	961	20120609-20130516	342	25	23	19	671	121	221
NWNB1306	62.9117	-6.0822	964	20130610-20140514	339	10	63	55	691	71	151
NWNB1406	62.9160	-6.0835	958	20140607-20150524	352	10	63	54	686	66	156
NWNB1506	62.9167	-6.0833	947	20150615-20160518	339	25	22	19	657	132	207
NWNB1606	62.9178	-6.0829	968	20160609-20170521	347	25	24	21	678	103	178
NWNB1706	62.9185	-6.0817	961	20170610-20180517	342	25	23	19	674	124	224
NWNB1806	62.9187	-6.0806	961	20180617-20190516	334	25	21	17	672	172	272

The ADCP data are time series of observations at regular intervals, termed "ensembles". For most deployments at NB, the time between ensembles has been 20 minutes and there have always been at least 72 pings a day. Within each ensemble, the information is structured vertically into "bins", which have either been 10 or 25 m in height. For most applications, we use daily averaged data (Hansen et al., 2015).

Site NB is on a steep slope, so that even with quite similar positions, there has been a variation of 80 m in bottom depth between the shallowest and the deepest deployment (Table 4.1). Consistent with that, the deepest bin, Bin 1, has varied between 623 m and 703 m. In addition to this variation, the various deployments have had different ranges, so that the last bin with acceptable data for some of the days in the deployment ("Last" in Table 4.1) has varied between 66 m and 202 m. The highest bin with 100% good data (all days acceptable) is denoted the "Top" bin in Table 4.1 and it is seen to have varied between 94 m and 272 m.

Site NB is almost midway between CTD standard stations N04 and N05, (Figure 1.1). From Table 2.4 it is seen that the 4°C-isotherm depths at the two stations are significantly correlated, but the correlation coefficient is only 0.56. Since regular ADCP measurements were initiated at NB in June 1997, there have been 92 CTD cruises with occupations at both N04 and N05 and Table C3 in Appendix C lists 4°C-isotherm depth at both stations as well as their average value and difference. The information in this table is summarized in Table 4.2, which demonstrates that the difference in isotherm depth between the two stations has almost as large a standard deviation as its average.

Table 4.2. Average (Avg), standard deviation (Std), minimum (Min), and maximum (Max) of the depth of the 4°C-isotherm at stations N04, N05, average of depths at N04 and N05, and difference between depths at N04 and N05. Based on 92 CTD cruises between June 1997 and May 2019. All values in m.

Depth at N04 (m)				Depth at N05 (m)				Average N04, N05				Difference N04-N05			
Avg	Std	Min	Max	Avg	Std	Min	Max	Avg	Std	Min	Max	Avg	Std	Min	Max
396	69	91	527	308	98	44	503	352	75	116	480	88	81	-128	270

From this, it is not obvious that the 4°C-isotherm depth at site NB is accurately related to the isotherm depths at N04 and N05, which will be termed $D_{N04}(t)$ and $D_{N05}(t)$, respectively. Nevertheless, the average value of these two depths is our best guess for the isotherm depth at NB for any given time and we define:

$$D_{NB}(t) = \frac{1}{2} \cdot (D_{N04}(t) + D_{N05}(t)) \qquad (4.1)$$

If we compare the depth of the 4°C-isotherm at either of the two CTD stations with simultaneous depths of other isotherms at the same station, we find that the isotherm depths are highly correlated (Table 4.3).

Table 4.3. Relationships between the depth of the 4°C-isotherm and the depths of isotherms for other temperatures (*T*) at stations N04 and N05. D_{NB} is the average isotherm depth at site NB estimated as the average of the depths at N04 and N05. For each of the stations, D_{Av} is the average depth, *N* the number of data points, *R* the correlation coefficient, and α and β are the regression coefficients in the equation: $D_T = \alpha \cdot D_4 + \beta$.

T	D_{NB}	Station N04					Station N05				
		D_{Av}	N	R	α	β	D_{Av}	N	R	α	β
°C	m	m				m	m				m
0	514	476	38	0.677	0.225	401	553	126	0.770	0.635	375
1	443	461	82	0.812	0.540	265	424	132	0.904	0.813	192
2	402	439	106	0.899	0.708	174	365	134	0.950	0.872	117
3	368	414	122	0.971	0.892	72	321	134	0.979	0.923	58
5	308	359	127	0.976	1.023	-38	257	134	0.986	1.003	-29
6	274	325	127	0.940	1.089	-97	223	134	0.943	1.033	-72

4.1 Determination of isotherm depth from ADCP backscattering strength

The backscattering strength measured by the ADCP at site NB is typically enhanced at depths within the depth range of the 4°C-isotherm and there might conceivably be a link between the two depths, either from physical or biological causes. To investigate this question, we may compare observed values of the 4°C-isotherm depth from CTD cruises with observed ADCP backscattering strength.

The ADCP deployments at site NB (Table 4.1) have been made with different instruments and even different models of RDI ADCPs. Most deployments were made with RDI 75 kHz BroadBand ADCPs of two different versions, but two deployments used an RDI Long Ranger ADCP. We use the "Intensity"

generated by the standard RDI software. According to the RDI ADCP Users Manual, the intensity at a distance R from the instrument, $I(R)$, is given by:

$$I(R) = A + B(R) - 20 \cdot log_{10}(R) - 2\alpha \cdot R \qquad (4.2)$$

where A is an instrument-dependent constant and α the absorption coefficient. $B(R)$ is the backscattering strength (in dB). Figure 4.1 shows average (continuous lines) and minimum (dashed) daily averaged intensity profiles from 19 ADCP deployments 1997-2016 that lasted more than 200 days (Table C4) and we see that the backscattering strength typically has a maximum close to – although somewhat deeper than - the average depth of the 4°C-isotherm.
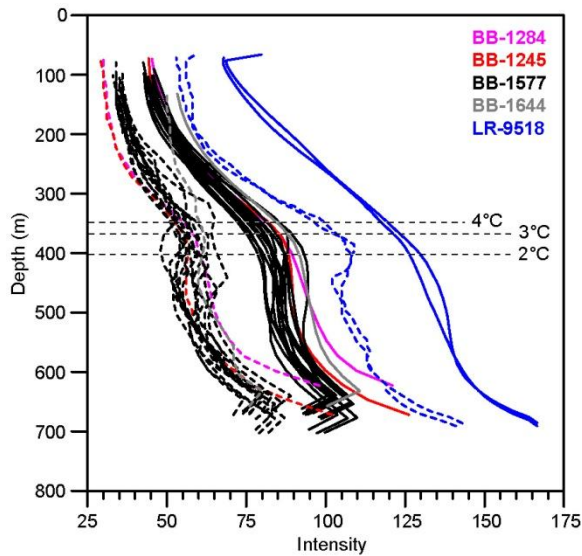
Figure 4.1. Average (continuous lines) and minimum (dashed lines) ADCP intensity profiles based on daily averages from 19 deployments at site NB (Table C4). Different colours represent different instruments. BB = BroadBand ADCP. LR = Long Ranger ADCP. Dashed horizontal lines indicate average depths of three isotherms at site NB.

If we assume that the minimum profiles in Figure 4.1 represent situations with $B(R) \approx 0$, then we can derive values for A and 2α from these profiles. Apparently, instrument BB-1577, which has been most frequently used at site NB, has a problem with bin 1, probably due to an inappropriate choice of setup parameters and the data from one of the LR-9518 deployments have been extended too far up. The values for 2α in Table C4 were therefore derived by inserting values for Bin 2 and Topbin - 1 for the minimum profiles into Eq. (4.2) with $B(R)=0$.

Most of the values for the BroadBand deployments are in the range (0.044 m^{-1} to 0.056 m^{-1}) reported by RDI for a 75 kHz ADCP. We will use a fixed value of $2\alpha = 0.05$ m^{-1} for these instruments. For the Long Ranger, the values fit better with the values for a 150 kHz instrument (0.078 m^{-1} to 0.10 m^{-1}) and we use the value $2\alpha = 0.09$ m^{-1} for the Long Ranger. The values for A in Table C4 are derived using these fixed values for 2α. The values are consistent, perhaps with a slow reduction in A over the more than 10 years for BB-1577 indicating a weakening of transmitted power.

Once values for A and 2α have been determined for a deployment, the backscattering strength $B(R)$ may be determined for each day based on the daily averaged intensity profiles and we may determine the depth at which the backscattering strength is maximum. Comparing these depths with the depths of the 4°C-isotherm determined from the CTD profiles for the same day, a relationship is not very obvious (Figure 4.2a) and the correlation coefficient (R=0.28) is low and barely significant statistically.

In Figure 4.2b, the depth variation of the backscattering strength is plotted relative to the depth of the 4°C-isotherm for the same day. There are a few negative values for backscattering strength, which indicate inappropriate values for A and/or 2α, since backscattering strength should always be positive. The negative values are only few and only slightly negative, however. The value for A, moreover, does not affect the depth variation of backscattering strength, which is the important factor.
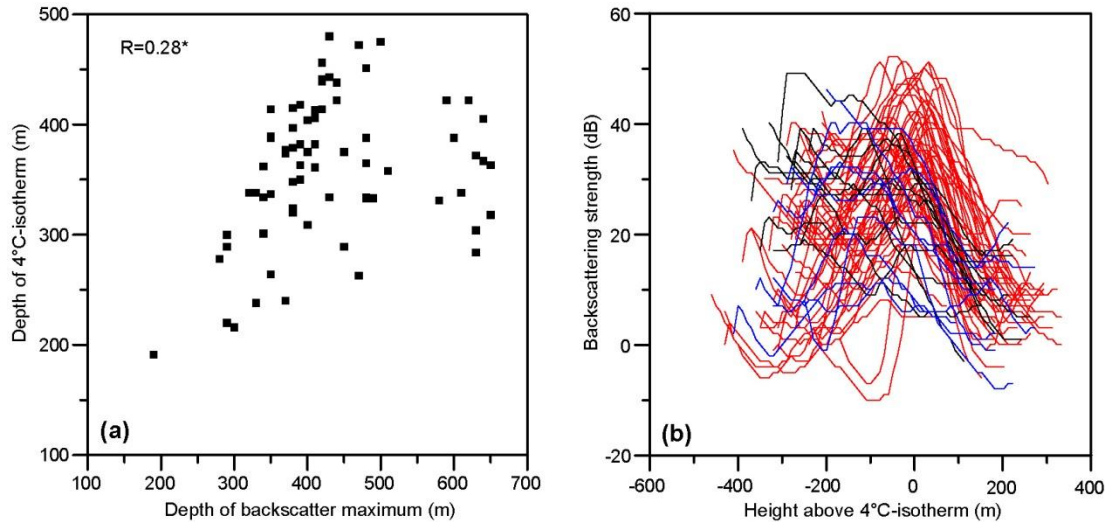
Figure 4.2. Comparison between the depth of the 4°C-isotherm at site NB (determined from CTD profiles as the average depth between stations N04 and N05) with the backscattering strength at site NB averaged over the same day as the CTD profiles. **(a)** Depth of the 4°C-isotherm plotted against the depth of the backscattering maximum. The correlation coefficient is shown with * indicating statistical significance $p < 0.05$. **(b)** Vertical variation of backscattering strength plotted relative to the depth of the 4°C-isotherm. Different colours indicate the depth difference ΔD between the 4°C-isotherm and the maximum backscattering strength. Red: $\Delta D < 100$ m. Blue: $100\,\text{m} < \Delta D < 200$ m. Black: $\Delta D > 200$ m.

The red curves in Figure 4.2b are those, for which the maximum backscattering was less than 100 m deeper or shallower than the 4°C-isotherm. These occasions seem to include some of the most pronounced backscattering maxima, but the difference between isotherm depth and backscattering maximum still varies by ±100 m for the red curves, which is more than the isotherm depth standard deviation (Table 4.2), and for the blue and black curves in Figure 4.2b, the difference is even higher.

Thus, it appears that there is not a clear relationship between the depths of the backscattering maximum and the 4°C-isotherm when using daily averaged ADCP intensity profiles. Alternatively, we might compare the isotherm depths with backscattering strength from individual ADCP ensembles rather than daily averages. Since the isotherm depth at site NB is calculated as the average of the depths observed at stations N04 and N05, the ADCP ensemble is chosen to be midway in time (within one hour) between the times of the CTD profiles at the two stations (Figure 4.3).

The impression from Figure 4.3 is not better than from Figure 4.2. The correlation coefficient remained low (R = 0.29*) and barely significant. It appears that there is not a very consistent relationship between the 4°C-isotherm and backscattering strength. A conceivable explanation for this negative result might be that the backscattering strength is related to the temperature (density) field but rather to another isotherm than 4°C. From Figure 4.1 it appears that the maximum backscattering strength on average is deeper than the 4°C-isotherm and might be better related to the 3°C-isotherm or the 2°C-isotherm.
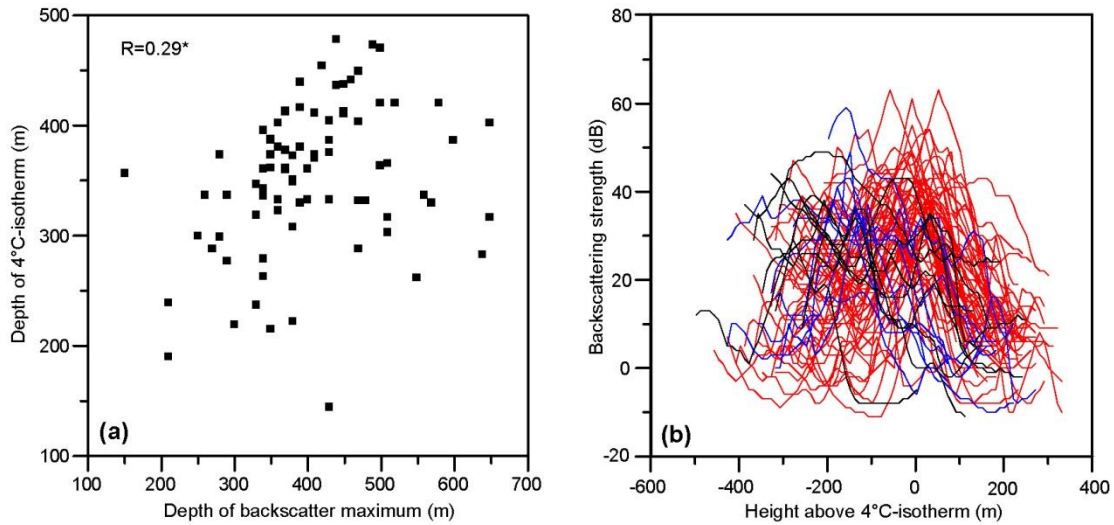
Figure 4.3. Same as Figure 4.2 except that the backscattering strength is not from daily averages but from individual ensembles at the same time (within 1 hour) as the CTD profiles.

From Table 4.3, we know that depths of other isotherms at either N04 or N05 are highly correlated with the simultaneous depth of the 4°C-isotherm at the site. If the backscattering strength was highly correlated with the isotherm for any temperature between 1°C and 6°C, the correlation with the 4°C-isotherm depth ought to have been better than observed. This was verified by running the analysis of Figure 4.3 with the 2°C-isotherm instead of the 4°C-isotherm. The correlation coefficient for this case was still only 0.28* (with a statistical significance level $p < 0.05$).

The seasonal variation of the backscattering strength was fairly similar at all depths sampled by the ADCP with a minimum in April-May and maximum during winter (Figure 4.4a). Intermediate depths had the highest backscattering strength for all months consistent with Figure 4.1 although this depends on having the correct value for 2α.
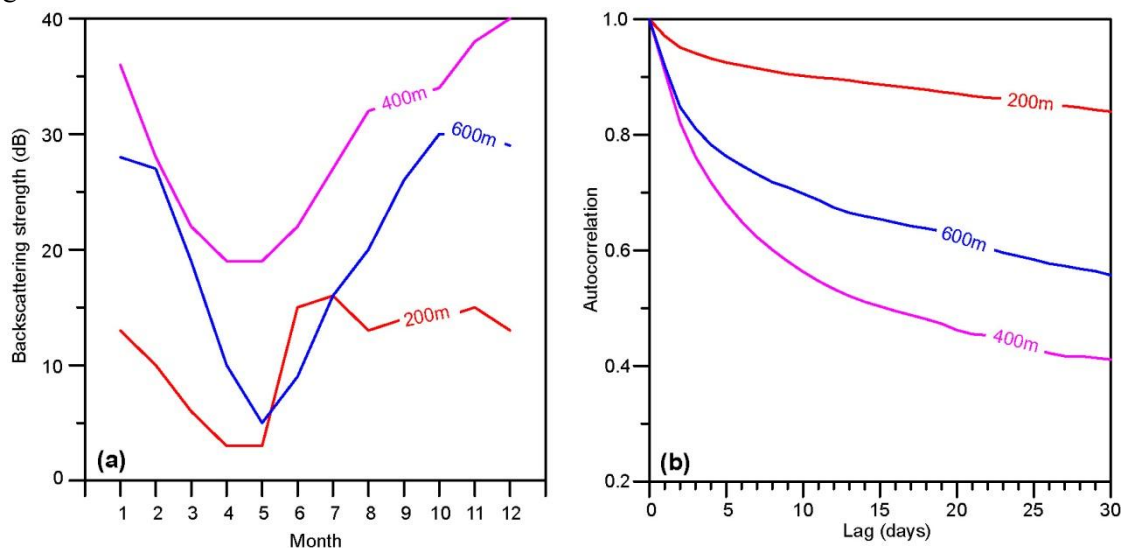
Figure 4.4. Variations of backscattering strength at three different depths. **(a)** Monthly averaged backscattering strength. **(b)** Autocorrelation function of the backscattering strength for lags 0 to 30 days.

An indication of shorter-term variability may be had from Figure 4.4b, which shows the autocorrelation function of backscattering strength for three different depths. At 200 m depth, the autocorrelation was high even at a lag of 30 days, perhaps indicating dominance of the seasonal signal. At larger depths, the autocorrelation for high lags was smaller especially at depths (400m) close to the boundary between the Atlantic and deeper water masses. Even at these depths, the autocorrelation for lag 1 day was, however, never less than 0.89. In spite of the diurnal rhythm, the daily averaged backscattering values therefore should be fairly representative.

4.2 Determination of isotherm depth from ADCP velocity profiles

4.2.1 Characteristics of the velocity at site NB

From Table 4.1, it is clear that there are many gaps in the time series of velocity measured by the ADCP at NB, but there are also large differences in the vertical coverage. In addition, there have been differences in bin length ("Lgt" in Table 4.1) and the same bin usually changes centre depth from one deployment to the next.

To get a homogeneous data set for the whole ADCP period at NB, we have therefore first interpolated linearly between bin centre depths and sampled the velocity data at 10 m depth intervals, starting at 80 m depth and ending at 600 m depth. Since only a few deployments have had observations above 80 m (Table 4.1), the number of days with acceptable data is small in the upper part, but increases with depth to reach 7606 days at 280 m depth (black curve in Figure 4.5).
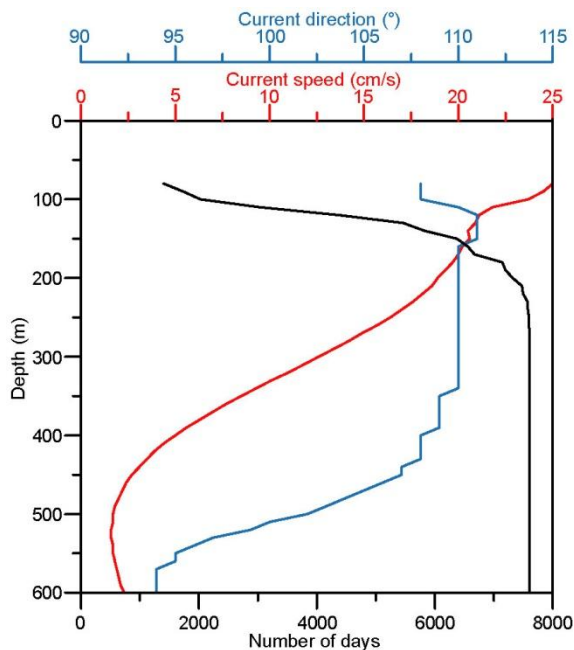
Figure 4.5. Speed (red) and direction (blue) of the vectorially averaged velocity profile and number of days with acceptable velocity data at each depth (black).

When considering the average velocity profile in Figure 4.5, it must be kept in mind that the uppermost part of the profile may be biased by the greatly reduced number of days on which the average is formed. From 200 m depth, downwards, the temporal coverage exceeds 96% and this part of the profile should be a fair representation of the long-term average, showing decreasing speed down to ≈500 m depth and a

northward turning of the current direction around this depth so that it flows almost directly eastwards at this depth on average.

At 200 m depth, the water is usually close to being pure Atlantic water and Figure 4.6 illustrates the characteristics of the velocity vector at this depth. The typical current speed is between 10 and 30 cm s^{-1} and the typical direction is slightly south of due east. Flow reversals do occur, however, and the daily averaged current had a westward component 15% of the time.
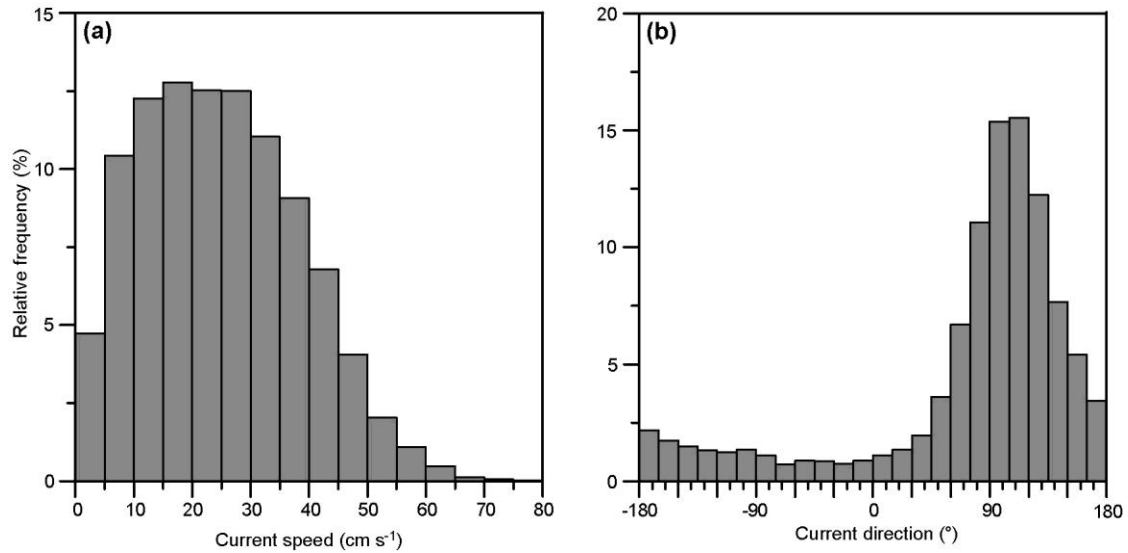
Figure 4.6. Histograms of daily averaged current speed **(a)** and current direction (from North) **(b)** at 200 m depth on site NB.

In spite of the spread in current direction (Figure 4.6b), the current at 200 m depth at NB is in fact fairly rectilinear. This may be demonstrated by sorting the daily averaged current vectors into bins where each bin covers an interval of 5 cm s^{-1} for eastward velocity (Figure 4.7).
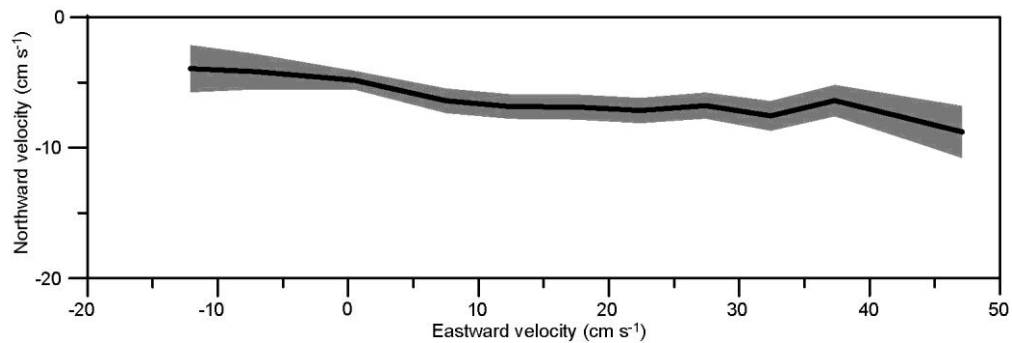
Figure 4.7. Current direction at 200 m depth on NB. The thick curve shows average northward velocity plotted against average eastward velocity. The shaded area shows ± two standard errors of the northward velocity based on 5 cm s^{-1} bins for the eastward velocity where bins with less than 100 days are excluded.

The velocity at NB exhibits strong seasonal variation with similar phase relationships at all depths and an almost barotropic variation (Figure 4.8). In the Atlantic water at 200 m depth (red curves), the speed is approximately twice as strong in March as in August while the direction remains almost constant. Below

the Atlantic layer, at 600 m depth, the current reverses and changes direction by ≈180° during summer at the same time as the eastward velocity at 200 m is weak.
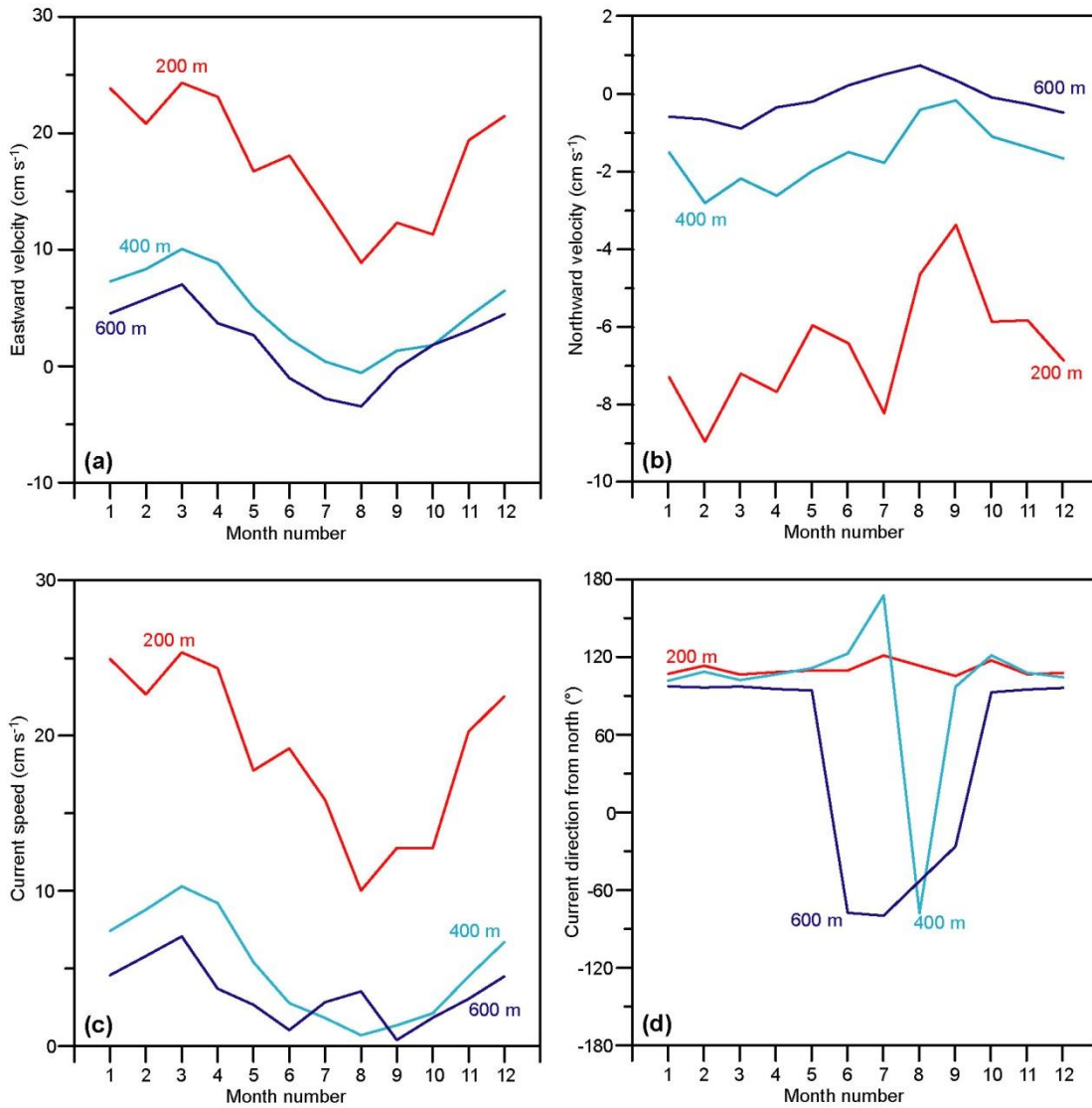
Figure 4.8. Monthly averaged eastward velocity **(a)**, northward velocity **(b)**, current speed **(c)**, and current direction **(d)** at three different depths at NB. Note that the averages are based on considerably fewer values during the annual servicing periods in summer, especially for 200 m depth in May and June.

On shorter time scales, the velocity components retain fairly high autocorrelations for lags of several days. This is especially the case for the eastward velocity at 200 m depth (Figure 4.9a), which has an autocorrelation of 0.34 for a lag of 7 days.

When different velocity parameters (speed, direction, east, north components) are compared, cross-correlations also show fairly (numerically) high values for lags up to several days, but not all of them seem to be in phase. This seems primarily to be associated with meso-scale activity.
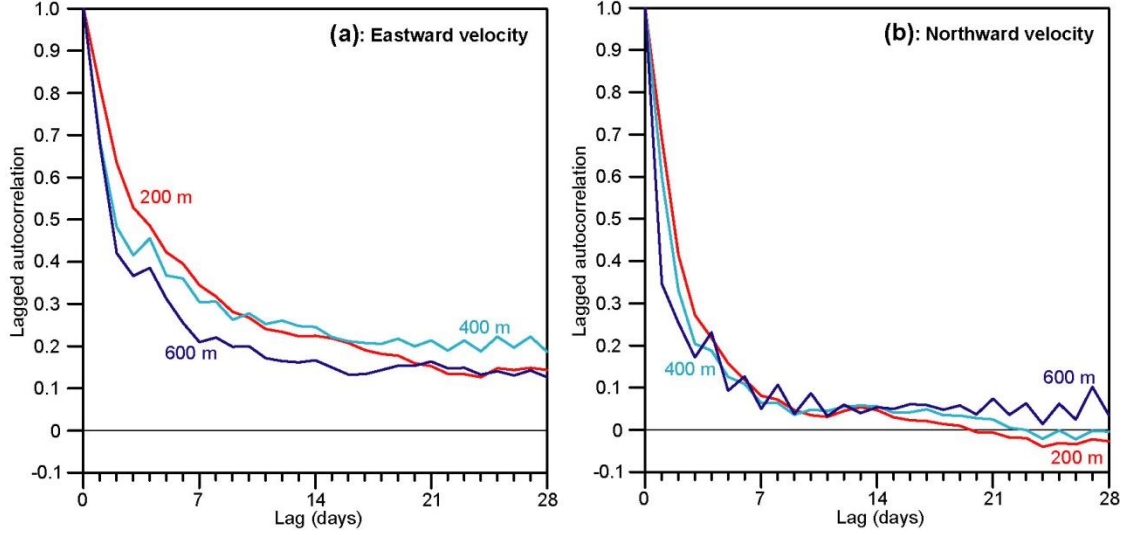
Figure 4.9. Lagged autocorrelation of eastward **(a)** and northward **(b)** velocity at 200 m depth (red), 400 m depth (cyan), and at 600 m depth (dark blue).

4.2.2 EOF analysis of the velocity profile at site NB

To separate the spatial and temporal variations of the velocity profile at NB, we have expressed each of the two velocity components (eastward and northward) in terms of Empirical Orthogonal Functions (EOF). Since the focus is on the Atlantic water and its lower boundary, we only include levels above 500 m depth. The analysis requires full data coverage spatially and we chose the uppermost level to be at 200 m depth, which implies that days with gaps above this level had to be excluded. This reduced the temporal coverage from 7606 to 7321 days.

Including three modes for each velocity component explained ≈99% of the variances (Table 4.4). The modes and their associated principal components were normalized so that all modes were positive in the top, at 200 m depth and the principal components had a standard deviation equal to 1. Thus, the eastward velocity is approximated as:

$$U_k(t) \cong \overline{U_k} + MU1_k \cdot PCU1(t) + MU2_k \cdot PCU2(t) + MU3_k \cdot PCU3(t) \qquad (4.3)$$

and similar for the northward velocity, where the index k ($k = 1,...,31$) refers to the depth levels between 200 m and 500 m depth in steps of 10 m, $\overline{U_k}$ is the average eastward velocity profile, $MU1_k$ is the first mode of the eastward velocity and $PCU1(t)$ its principal component, etc.

Table 4.4. Explained variance for each of the three EOF modes and the sum of the three (Total) for eastward and northward velocity.

	Eastward velocity				Northward velocity			
	MU1	MU2	MU3	Total	MV1	MV2	MV3	Total
Expl. var.:	0.829	0.138	0.024	0.990	0.927	0.047	0.014	0.988

For both velocity components, the first mode (red curves in Figure 4.10) retains the same sign (positive) for all depths and may be termed a barotropic mode, whereas the other modes change sign and are of more baroclinic character.
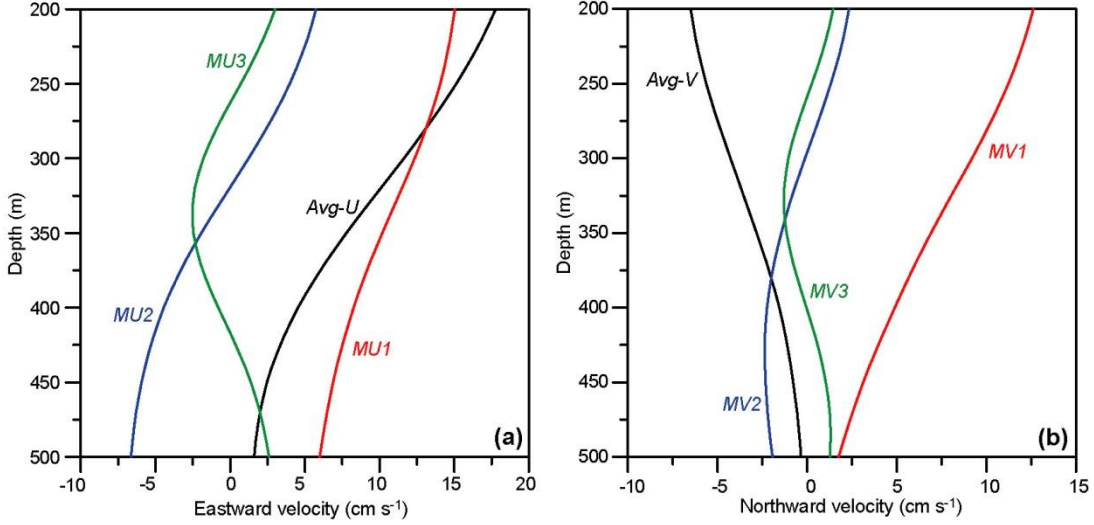
Figure 4.10. Average velocity profile (black) and vertical variation of three modes (red, blue, and green) for the eastward and northward velocity components.

By choosing the uppermost level for the EOF analysis to be at 200 m depth, 285 days had to be excluded because they were error-flagged at this level, and some of them below it. This means that there are no principal components for these days but, to some extent, they can still be recovered. To that end, we utilize the fact that the modes are orthogonal to one another in space (depth), which for the first mode of the eastward (U) component means that Eq. (4.3) leads to:

$$\sum_{k=1}^{31}\left[U_k(t) - \overline{U_k}\right] \cdot MU1_k \cong PCU1(t) \cdot \sum_{k=1}^{31} MU1_k \cdot MU1_k \qquad (4.4)$$

and similar for all the other modes. This equation allows the derivation of the principal component *PCU1(t)* from $U_k(t)$ and all the values for $MU1_k$. The motivation for doing this is that Eq. (4.4) should still be approximately valid if we sum; not from $k = 1$ (i.e., 200 m depth), but from $k = 2$ (210 m depth) or some higher number, k_s, which will allow determination of principal components for days with error-flagged data at and deeper than 200 m. To see how good the approximations are, we have used Eq. (4.4) to derive alternative values for *PCU1(t)* with $k_s = 1,...,8$ and then correlated these alternative principal components with the original ones, and similarly for the other principal components (Table 4.4).

Table 4.4. The last six columns list correlation coefficients between the original principal components and principal components determined by Eq. (4.4) and its analogues with the sums starting at $k = k_s$ instead of $k = 1$. The second column (Depth) lists the depths associated with each k_s value while the third column (N_D) lists the number of days that are error-flagged for this depth.

k_s	Depth	N_D	Eastward velocity			Northward velocity		
			PCU1	PCU2	PCU3	PCV1	PCV2	PCV3
1	200	285	1.000	1.000	1.000	1.000	1.000	1.000
2	210	130	1.000	0.988	0.888	1.000	0.953	0.814
3	220	109	0.998	0.953	0.692	0.999	0.840	0.579
4	230	35	0.996	0.900	0.548	0.998	0.719	0.442
5	240	28	0.992	0.838	0.461	0.996	0.618	0.369
6	250	11	0.987	0.776	0.413	0.993	0.544	0.332
7	260	7	0.981	0.720	0.391	0.990	0.492	0.319
8	270	6	0.973	0.673	0.387	0.986	0.457	0.320

For $k_s = 1$, we ought to reproduce the original principal components according to Eq. (4.4). Correlation coefficients equal to 1 are therefore to be expected for that case, but the principal components associated with the first modes are seen to retain high values all the way up to $k_s = 8$, which is the deepest level for which days had to be excluded before the EOF analysis. For the principal components associated with higher modes, the correlation coefficients in Table 4.4 decrease more rapidly with increasing k_s values.

From this, it appears that the principal components associated with the first modes for both velocity components may be generated with this procedure for all the days that were error-flagged at 200 m depth, whereas the principal components associated with higher modes would only be approximately correct for days that were error-flagged at 200 m depth; but not at 210 m.

An alternative procedure for recovering error-flagged days would be interpolation in time, which will work best if only single days are error-flagged with good data on the preceding and the following day. For interpolation to succeed, there has to be appreciable autocorrelation at least for a lag of one day. As seen in Figure 4.11, most of the principal components unfortunately have rapidly decreasing auto-correlations. Consistent with this, interpolation of gaps even as short as just one day are not very accurate (Table 4.5).
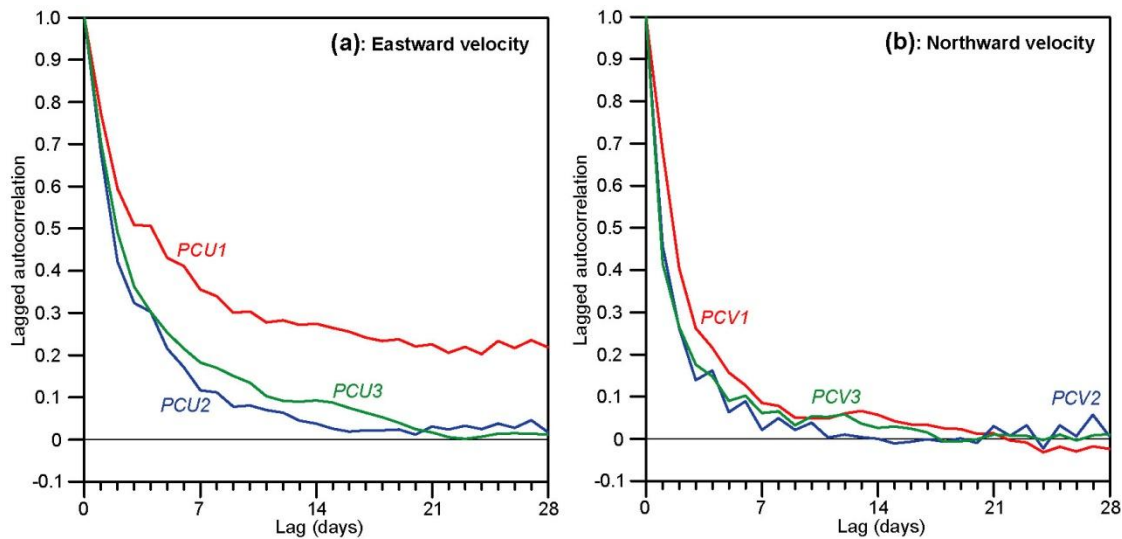
Figure 4.11. Lagged autocorrelation of principal components for eastward **(a)** and northward **(b)** velocity.

Table 4.5. Number of days with principal components on the day, the preceding, and the following day (*N*), and correlation coefficients between the principal components on that day and the averages of the preceding and the following day.

	Eastward velocity			Northward velocity		
N	*PCU1*	*PCU2*	*PCU3*	*PCV1*	*PCV2*	*PCV3*
7111	0.865***	0.807***	0.816***	0.816***	0.578***	0.525***

4.2.3 Using the thermal wind equation at site NB

Since the ADCP site NB is located almost exactly midways between stations N04 and N05, the thermal wind equation implies that the tilt of the 4°C-isotherm between N04 and N05 ought to be related to the vertical gradient of the eastward velocity at NB in the depth interval between isotherms at both stations. If

the vertical density gradient ($\partial \rho / \partial z$) were to be constant, the difference in isotherm depth between the two stations should be:

$$D_{N04} - D_{N05} = -\frac{\rho \cdot f \cdot L}{g \cdot \left(\frac{\partial \rho}{\partial z}\right)} \cdot \frac{\partial U}{\partial z} \qquad (4.5)$$

where L is the horizontal distance between stations N04 and N05 and U is eastward velocity. There are altogether 85 CTD occupations at both N04 and N05 while the ADCP site was instrumented. After some experimentation, we chose to use an 80 m depth interval to estimate $\partial U / \partial z$. From Figure 4.12a, there appears to be a fairly good linear relationship between this velocity gradient and the depth difference ($D_{N04} - D_{N05}$). The regression line in Figure 4.12a would be consistent with Eq. (4.5) with a value of -0.003 kg m^{-3} m^{-1} for ($\partial \rho / \partial z$), which seems reasonable.
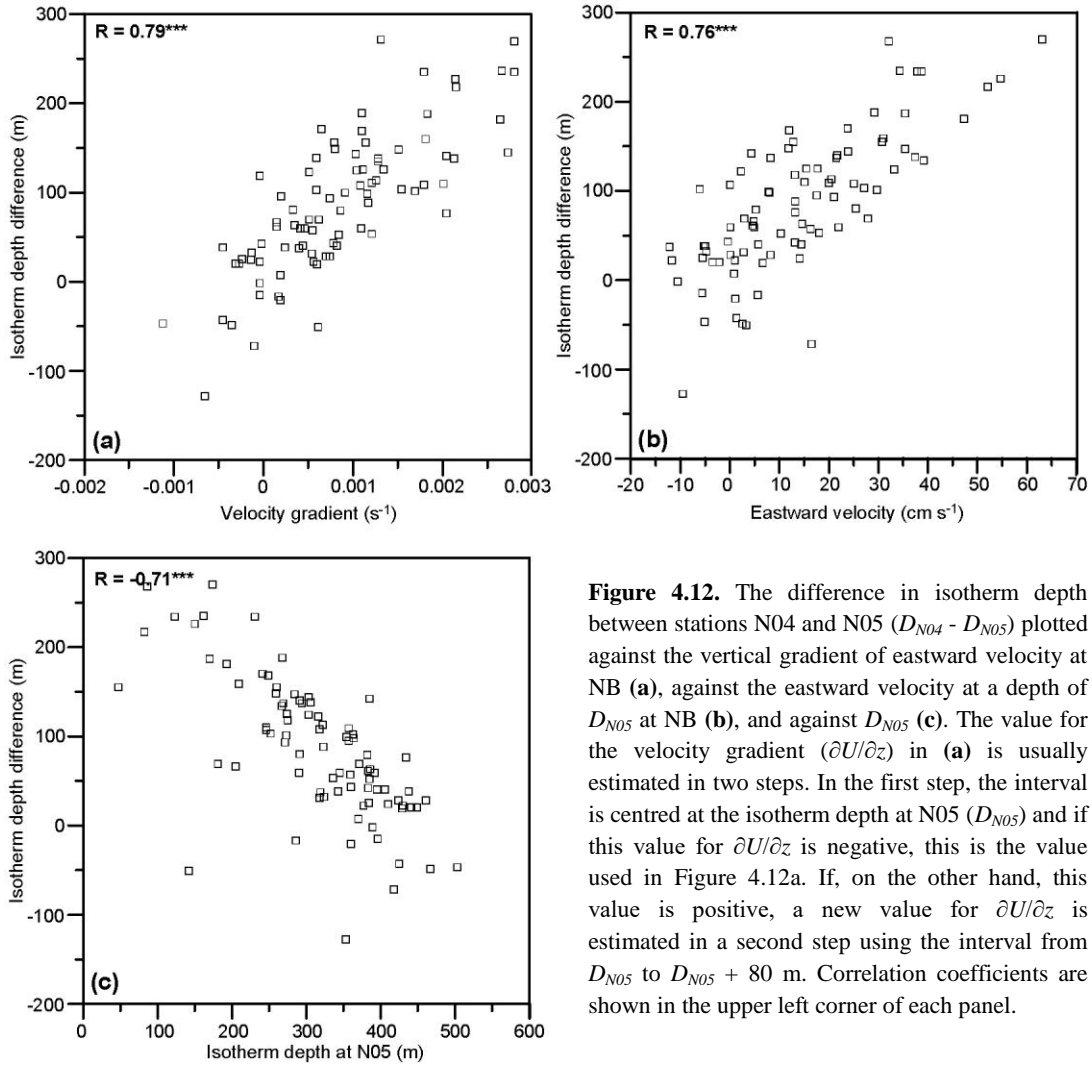
Figure 4.12. The difference in isotherm depth between stations N04 and N05 ($D_{N04} - D_{N05}$) plotted against the vertical gradient of eastward velocity at NB **(a)**, against the eastward velocity at a depth of D_{N05} at NB **(b)**, and against D_{N05} **(c)**. The value for the velocity gradient ($\partial U / \partial z$) in **(a)** is usually estimated in two steps. In the first step, the interval is centred at the isotherm depth at N05 (D_{N05}) and if this value for $\partial U / \partial z$ is negative, this is the value used in Figure 4.12a. If, on the other hand, this value is positive, a new value for $\partial U / \partial z$ is estimated in a second step using the interval from D_{N05} to $D_{N05} + 80$ m. Correlation coefficients are shown in the upper left corner of each panel.

In reality, ($\partial \rho / \partial z$) is not constant, especially in the upper layers (Figure 2.7) and ($D_{N04} - D_{N05}$) is also seen to be related to the eastward velocity at depth D_{N05} (Figure 4.12b), as well as to D_{N05} (Figure 4.12c) (which of course is not surprising).

If the depth of the 4°C-isotherm at N05 (D_{N05}) is known at a time when there was an ADCP at site NB, then these relationships may be used to estimate the isotherm depth at N04 (D_{N04}). Two different equations may be used for this purpose:

$$D_{N04} \cong a_U \cdot \frac{\partial U}{\partial z} + b_U \cdot U(D_{N05}) + c_U + D_{N05} \qquad (4.6)$$

and:

$$D_{N04} \cong a_D \cdot \frac{\partial U}{\partial z} + b_D \cdot D_{N05} + c_D \qquad (4.7)$$

where $\partial U/\partial z$ is estimated as described in the caption of Figure 4.12 and the coefficients have been determined by multiple linear regression on the 85 occasions for which we have data (Table 4.6).

Table 4.6. Parameters in Eq. (4.6) and Eq. (4.7) determined by multiple linear regression.

Parameters for Eq. (4.6)			Parameters for Eq. (4.7)		
a_U	b_U	c_U	a_D	b_D	c_D
45851m·s	206s	18m	52143m·s	0.711	132m

The performances of the two fits in Eq. (4.6) and Eq. (4.7) are illustrated in Figure 4.13, which shows that the Root-mean-Square errors (RMS) are very similar. The largest error was, however, considerably higher (174 m) for Eq. (4.7) than for Eq. (4.6) (119 m) and Eq. (4.7) generally seems to overestimate D_{N04} when it is low (shallow isotherm). Multiple linear regression involving all three parameters ($\partial U/\partial z$, $U(D_{N05})$, and D_{N05}) did not improve the fit and using non-linear regression without some theoretical justification does not seem appropriate.
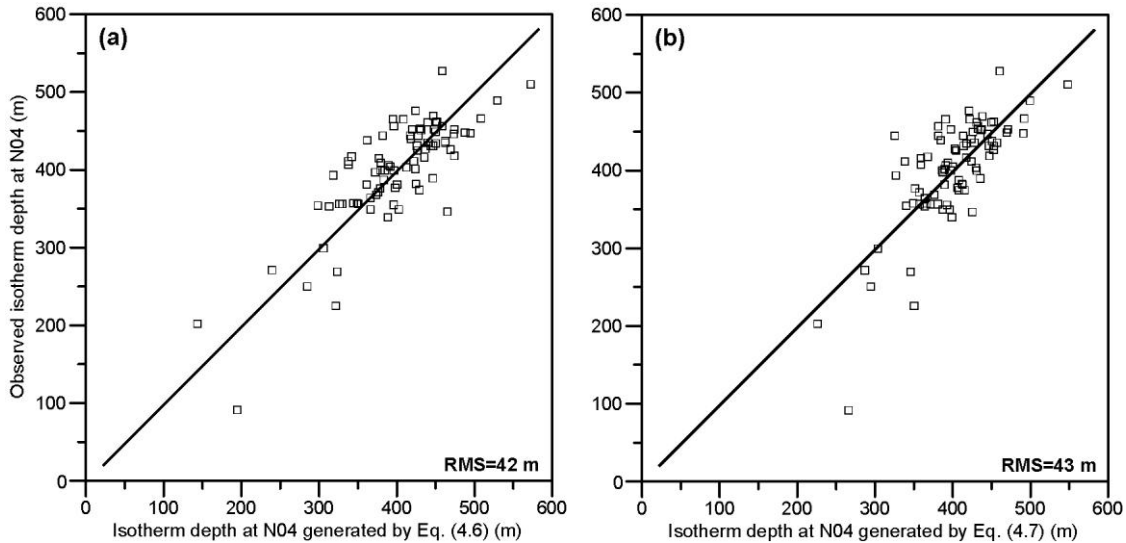
Figure 4.13. Observed (by CTD) depth of the 4°C-isotherm at station N04 plotted against isotherm depth as generated by Eq. (4.6) **(a)** and by Eq. (4.7) **(b)**. The diagonal lines indicate equality and Root-mean-Square errors (RMS) are indicated.

4.2.4 Using EOF principal components at site NB to estimate isotherm depth

The main motivation for introducing EOF modes was the hope that their principal components could be used to estimate isotherm depth especially for the neighbouring stations N04 and/or N05. To investigate that possibility, we have correlated all the principal components with the 4°C-isotherm depth at N04,

N05, their average, and their difference. The result is not very encouraging, however. Only the isotherm depth difference (ΔD) has correlation coefficients above 0.5 and the variations of this difference seem better described by the observed velocity shear (Figure 4.12a) than by principal components.

Table 4.7. Number of days with 4°C-isotherm depths at both N04 and N05 from CTD and with principal components (*N*), and correlation coefficients between the principal components and the isotherm depth at N04 (D_{N04}), at N05 (D_{N05}), at NB (D_{NB}) as defined by Eq. (4.1), and the difference (ΔD) in isotherm depth at N04 and N05 (D_{N04} - D_{N05}).

PC	N	Eastward velocity				Northward velocity			
		D_{N04}	D_{N05}	D_{NB}	ΔD	D_{N04}	D_{N05}	D_{NB}	ΔD
1	83	0.23*	-0.28*	-0.08	0.53***	0.27*	0.20	0.25*	-0.01
2	83	0.22*	-0.25*	-0.06	0.50***	-0.14	-0.23*	-0.21	0.16
3	83	-0.33**	-0.44***	-0.44***	0.24*	0.18	0.15	0.18	-0.03

Instead of comparing the principal components to isotherm depth from CTD observations, we can use the isotherm depths derived from the PIES at station N05. The result is, however, just as discouraging for this comparison (Table 4.8).

Table 4.8. Number of days with PIES estimate of isotherm depth at N05 and principal components (*N*), and correlation coefficients between the principal components and the 4°C-isotherm depth derived from PIES data (Chapter 3).

N	Eastward velocity			Northward velocity		
	PCU1	PCU2	PCU3	PCV1	PCV2	PCV3
544	-0.20	-0.39***	-0.36***	0.07	0.07	0.27***

4.2.5 Using the velocity profile at site NB to estimate isotherm depth

It seems reasonable to expect some relationship between the velocity profile at NB and isotherm depths at the neighbouring stations N04 and N05 in addition to the thermal wind relationship addressed in Sect. 4.2.3. To get a first impression, we considered all the 84 CTD occupations at N05 for which there were ADCP velocity profiles for the same day. These profiles span a wide range both in speed (top left panel in Figure D1) and in the two velocity components (top left panels in Figure D2 and Figure D3).

We then sorted the velocity profiles into groups according to the depth of the 4°C-isotherm for the same day (remaining panels in Figure D1, D2, and D3). In these figures, there seems to be a tendency that very strong (> 50 cm s^{-1}) flow in the upper layers with a pronounced and shallow weakening of the flow only occurs when the isotherm is shallow (< 300 m). The opposite is, however, not true. Weak flow at all depths may apparently occur independently of isotherm depth.

From these figures it appears that daily averaged velocity profiles at NB may be too noisy to be very useful. For the monitoring of the Faroe Current, we are, however, focusing on monthly time scales and have therefore plotted similar figures for 28-day averaged data. The CTD data are snapshots so the only available data on isotherm depth that can be averaged are the PIES data. In the period with PIES observations at N05 (1st August 2017 to 7th June 2019), there were two ADCP deployments at NB from which we can generate 20 contiguous 28-day periods. In these 20 periods, the average 4°C-isotherm depth varied between 180 m and 425 m and in Figure 4.14, the 20 velocity profiles have been sorted into four differently coloured groups based on this.

In Figure 4.14 there are some indications of links between isotherm depth and velocity profile, but there is no clear one-to-one grouping. The most obvious links to be expected would be the eastward velocity of the Atlantic water and the depth of the velocity transition layer. Unfortunately, the last ADCP deployment in the PIES deployment period (NWNB1806, Table 4.1) had technical problems and only reached 272 m depth for 100% good daily averaged data (Top in Table 4.1). Therefore, several of the

profiles in Figure 4.14 only reached depths below 200 m. We therefore use the eastward velocity at 250 m depth (U_{250}) as a measure of Atlantic water flow. With this choice, 19 of the 20 periods could be included.
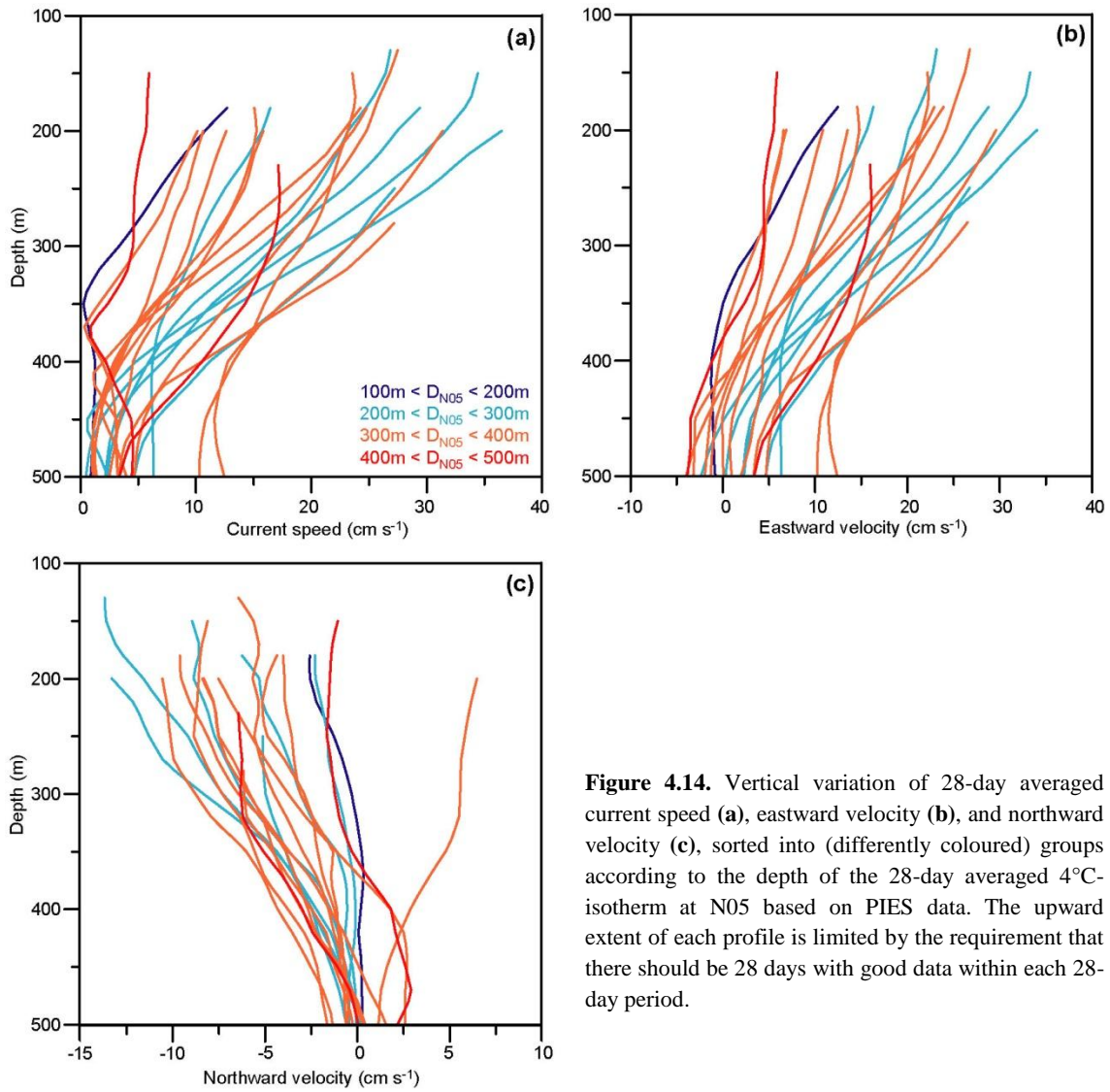
Figure 4.14. Vertical variation of 28-day averaged current speed (**a**), eastward velocity (**b**), and northward velocity (**c**), sorted into (differently coloured) groups according to the depth of the 28-day averaged 4°C-isotherm at N05 based on PIES data. The upward extent of each profile is limited by the requirement that there should be 28 days with good data within each 28-day period.

For a robust (inverse) measure of the depth of the velocity transition layer (β_{tr}), we use the ratio between the eastward velocity at 250 m depth and the average eastward velocity between 250 m and 400 m depth ($U_{250\text{-}400}$):

$$\beta_{tr} \equiv {U_{250}}/{U_{250-400}} \qquad (4.8)$$

As seen in Table 4.9, this measure of the velocity transition layer depth is significantly correlated with the 4°C-isotherm depth and a linear combination of this measure with the eastward velocity at 250 m depth explains 61% of the variance in isotherm depth.

Table 4.9. Relationships between 28-day averaged 4°C-isotherm depth at N05 (D_{N05}) based on PIES data and parameters derived from the velocity profile at NB. The first three columns list correlation coefficients (R) with D_4. The remaining columns list explained variance (R^2) and coefficients in the multiple regression equation shown.

U_{250}	$U_{250-400}$	β_{tr}	$D_{N05} = a \cdot U_{250} + b \cdot \beta_{tr} + c$		
R	R	R	R^2	a	b	c
-0.38	-0.22	-0.50*	o.61	-545s	-99.2m	576m

The ability of this linear combination to reproduce the isotherm depth variations is illustrated in Figure 4.15. If we consider the isotherm depths based on PIES data to be exact, the RMS-error of the values generated by the regression equation is 39 m with the largest deviation being 87 m.
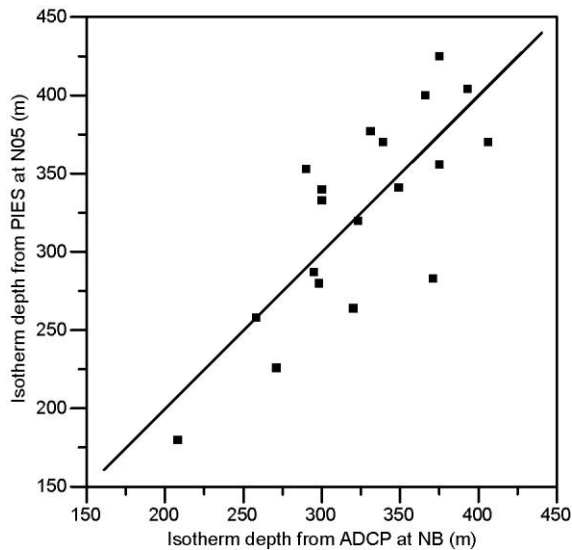
Figure 4.15. 28-day averaged depth of the 4°C-isotherm at N05 as derived from PIES data plotted against the isotherm depth as determined by the regression equation and its parameters listed in Table 4.9. The diagonal line represents equality.

4.3 The velocity transition depth at NB and isotherm depth

To investigate in more detail the relationship between 4°C-isotherm depth at N05 and the velocity profile at NB, we selected all isotherm depth values for which there was an ADCP profile reaching at least up to 150 m depth on the same day (72 cases). These data confirm that the isotherm tends to become shallower when the eastward velocity at 150 m depth increases (Figure 4.16) although the relationship is noisy.
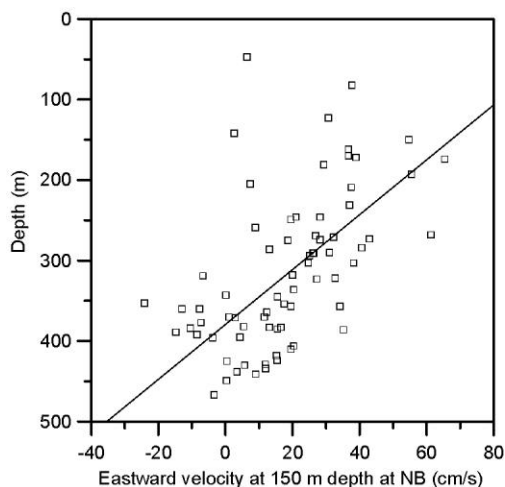
Figure 4.16. Depth of the 4°C-isotherm at N05 plotted against the eastward velocity at 150 m depth at NB on the same day. The thin line is the regression line for values with the velocity positive and at least 5 cm/s.

The 4°C-isotherm is considered a good indicator of the boundary between the fast-flowing Atlantic water on top and the more slowly flowing Arctic water below. It therefore seems reasonable to expect the isotherm depth to be associated with the transition depth of the velocity profile, i.e., the depth at which the velocity has decreased appreciably compared to the near-surface velocity.

If that is the case, it means that the Atlantic water flow becomes shallower when it speeds up. A priori, this might seem to indicate that when the upper layers speed up, the deeper layers should slow down. But, that is in conflict with previous results indicating that the temporal velocity variations are highly barotropic (e.g., Hansen et al., 2019a).

To get a better understanding of this, we analyzed all the daily averaged velocity profiles at NB with good data from 150 m downwards (6375 days in total). As illustrated in Figure 4.17a, the correlation coefficient between the velocity at 150 m depth and at deeper levels remains positive all the way down to 600 m depth (and highly significant, p<0.001).

The regression coefficient also remains positive, but falls below 0.5 slightly deeper than 300 m. To see the effect of this, all of the profiles with the eastward velocity at 150 m depth being at least 5 cm/s were split into six groups according to the velocity (Figure 4.17b). The figure verifies the barotropic character of the velocity variations, but also that the transition depth does tend to become shallower when the upper layer flow speeds up.

In Figure 4.17b, we have used two different indicators of transition depth. One of these, the "50%-depth", is the depth at which the eastward velocity has been reduced to being half that at 150 m depth. The other, "Maximal gradient", is the depth at which the vertical gradient of eastward velocity (at 10 m intervals) is maximal. Both of these depths tend to be between 300 and 400 m depth and become shallower when the upper layer speeds up
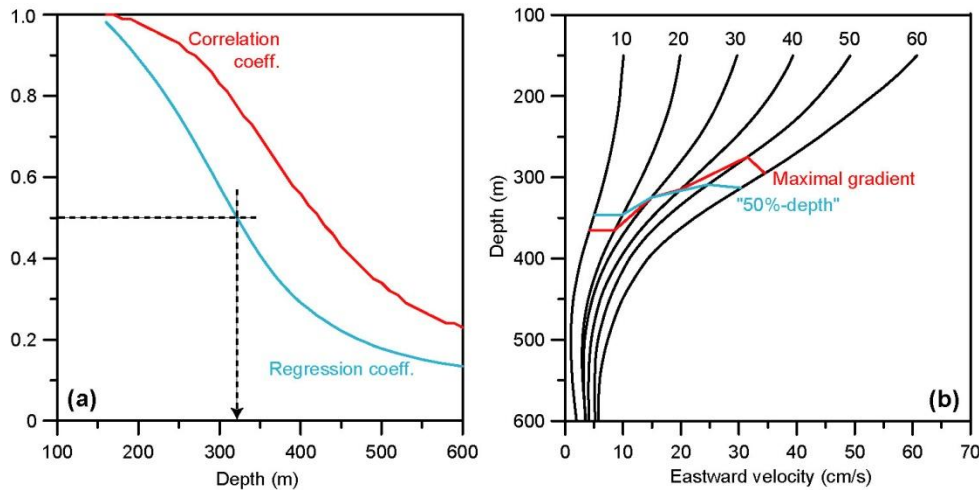
Figure 4.17. (a) The red curve shows the correlation coefficient between the eastward velocity at 150 m depth, $U_{150}(t)$, and at depth D, $U_D(t)$, for D = 150 – 600 m. The cyan curve shows the regression coefficient, α, in the equation: $U_D(t)= \alpha \cdot U_{150}(t)+ \beta$. The dashed vertical arrow indicates the depth at which α has decreased below 0.5. **(b)** Average eastward velocity profiles split into six groups according to the velocity at 150 m depth. Each group contains all velocity profiles within a ±5 cm/s interval around the number above each profile (in cm/s). Thus, the profile labeled "10" is the average of all profiles for which (5 cm/s ≤ $U_{150}(t) <$ 15 cm/s), etc. A few profiles with $U_{150}(t) >$ 65 cm/s were included in the 60 cm/s group. All groups contained more than one hundred profiles.

This confirms that there is no conflict between barotropic velocity variations and transition depths decreasing with increasing upper-layer velocity. It also indicates that the 4°C-isotherm depth at N05 may vary synchronously with the transition depth of the eastward velocity at NB, which is verified in Figure 4.18. On average, the isotherm is 47 m shallower than the 50%-depth and 14 m shallower than the maximal gradient depth.
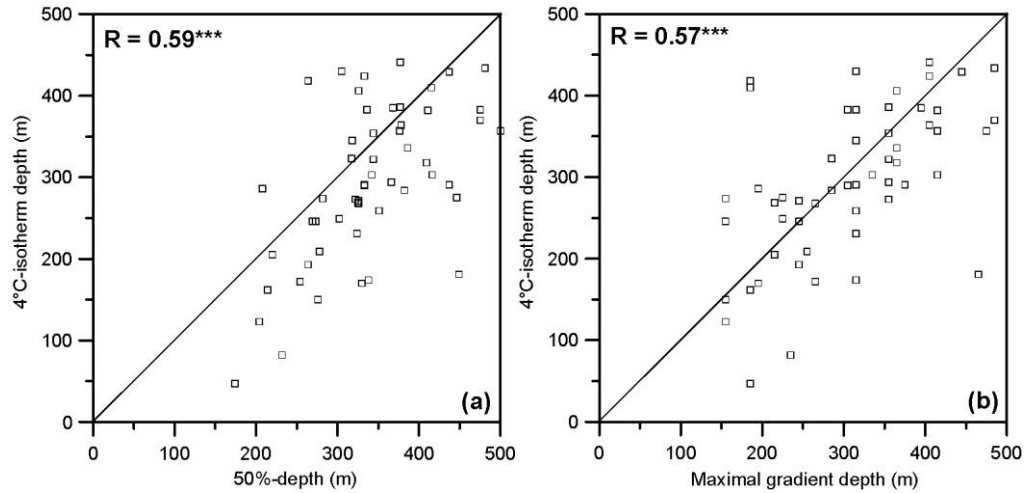
Figure 4.18. The depth of the 4°C-isotherm at N05 plotted against the two different indicators of transition depth for the velocity at NB including all profiles with the eastward velocity at 150 m depth exceeding 5 cm/s. Correlation coefficients are indicated in the upper left corners of the panels.

So far, we have only considered relationships between the velocity profile at NB and the isotherm depth at N05. Table 4.10 demonstrates that statistically significant relationships are seen for stations N04 to N07, especially between isotherm depth and the Maximal gradient depth (R_{Max}). When the transition depth of the velocity at NB deepens, the isotherms in the southern part of the section tend to do the same. Although significant, the correlation coefficients are not very high, but meso-scale activity may perhaps bear some of the blame for that.

Table 4.10. Relationships between 4°C-isotherm depths at stations N04 to N10 and various characteristics of the velocity profile at NB on the same day. "Number" is the number of cases for each station. "R_{U150}" is the correlation coefficient between isotherm depth and the eastward velocity at 150 m depth. "$R_{50\%}$" is the correlation coefficient between isotherm depth and the 50%-depth. "R_{Max}" is the correlation coefficient between isotherm depth and the Maximal gradient depth. "$\Delta_{50\%}$" is the average difference between isotherm depth and the 50%-depth. "Δ_{Max}" is the average difference between isotherm depth and the maximal gradient depth. Only days with the eastward velocity at 150 m depth exceeding 5 cm/s are included.

Station:	N04	N05	N06	N07	N08	N09	N10
Number:	54	54	53	52	53	51	51
R_{U150}:	-0.02	-0.50***	-0.44**	-0.31*	-0.05	0.07	-0.14
$R_{50\%}$:	0.56***	0.59***	0.26	0.04	0.09	-0.08	-0.06
R_{Max} :	0.57***	0.57***	0.40**	0.36*	0.24	0.08	0.12
$\Delta_{50\%}$:	65m	-47m	-82m	-119m	-158m	-213m	-256m
Δ_{Max} :	98m	-14m	-55m	-98m	-137m	-191m	-235m

5 Isotherm depth from satellite altimetry

5.1 The altimetry data set

5.1.1 Sea level and surface velocity

We use the Sea Level Anomaly (SLA) data set released by Copernicus, from which we have extracted daily values for sea level height at eight grid points A_1 to A_8 (Figure 1.1) along 6.125°W extending from 62.125°N to 63.875°N. Sea level height at point A_k will be labelled $H_k(t)$, $k = 1,...,8$.

Most of the Atlantic water flow on the section is located between grid points A_3 and A_7 and the average sea level based on the five grid points within this region shows both an increasing trend and a seasonal variation (Figure 5.1). Even when including the abnormal year 2003, the annually averaged sea level has a positive trend, which is statistically significant: (0.29 ± 0.13) cm year^{-1} where the $\pm$ indicates the 95% confidence limit. This is close to the global average for the same period. The seasonal variation has an average range exceeding 12 cm (Figure 5.1b).
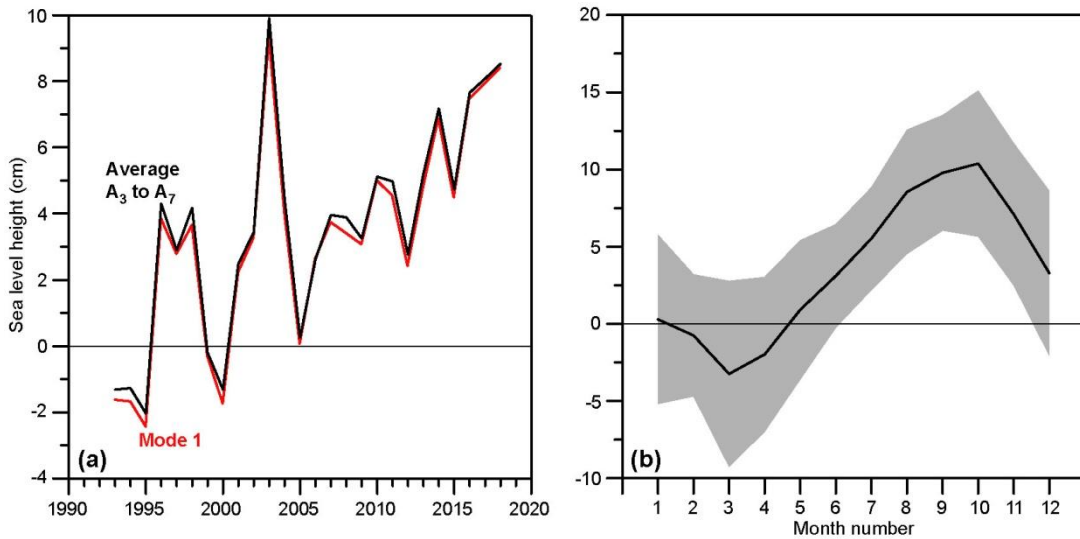
Figure 5.1. Black curves show long-term and seasonal variations of the average sea level between points A_3 and A_7. **(a)** Annual average plotted against the year. **(b)** Monthly averages plotted against the month number. Black curve shows overall average for each month. Shaded area shows average ± one standard deviation. The red curve in **(a)** shows the annually averaged principal component associated with the first sea level mode (Figure 5.4a) multiplied by the average value for the mode (Figure 5.2a) between points A_3 and A_7 (vertical offset random).

On the assumption of geostrophy, the (horizontally averaged) eastward surface velocity in each interval between two altimetry points is proportional to the sea level tilt between the two points:

$$U_k(t) = \frac{g}{f \cdot L} \cdot [H_k(t) - H_{k+1}(t)] \quad (k = 1, ...,7) \qquad (5.1)$$

5.1.2 Altimetry data coverage

At the time of processing for this report, the high-quality "Delayed-time" altimetry data had only been released for the period from 1st January 1993 to 13th May 2019. The series might have been extended by using the "Near-real-time" data set, which is, however, of lower quality. To evaluate the uncertainties induced by that, a comparison between the two data sets was made for 74 days in 2019 (January + February + May).

The correlation coefficients between the two data sets (R in Table 5.1) are generally high, but in many cases still well below 1, especially for the differences between neighbouring points (last seven

columns in table), which should be proportional to surface velocities. Perhaps more importantly, the maximum difference between the two data sets (Max Δ in Table 5.1) in many cases exceeds the standard deviation for the Delayed-time series (Std D in the table). It was therefore decided to restrict the use of altimetry data to the period of the Delayed-time series.

Table 5.1. Comparison between Near-real-time and Delayed-time altimetry data for the eight altimetry points along the monitoring section during 74 days in 2019, listing correlation coefficients between the two data sets (R), the standard deviation for the Delayed-time data (Std D), and average (Avg Δ), standard deviation (Std Δ), and maximum (absolute) value (Max Δ) for the difference between the two data sets. The first eight columns compare sea level height at individual points. The last seven columns compare sea level difference between neighbouring points.

	A_1	A_2	A_3	A_4	A_5	A_6	A_7	A_8	A_1-A_2	A_2-A_3	A_3-A_4	A_4-A_5	A_5-A_6	A_6-A_7	A_7-A_8
R:	0.89	0.89	0.92	0.92	0.89	0.93	0.95	0.94	0.91	0.80	0.93	0.98	0.99	0.79	0.93
Std D:	2.67	2.41	2.49	3.26	3.82	4.34	4.00	3.59	0.57	0.84	1.20	2.06	2.04	0.75	0.85
Avg Δ:	0.36	0.55	0.36	0.10	0.09	0.14	0.00	-0.17	-0.19	0.18	0.26	0.01	-0.05	0.13	0.18
Std Δ:	1.30	1.19	1.31	1.64	1.78	1.57	1.31	1.27	0.32	0.64	0.52	0.39	0.34	0.49	0.32
Max Δ:	3.16	2.88	2.96	3.12	3.13	2.89	2.73	2.71	0.96	2.02	1.67	0.88	0.86	1.14	0.89

5.2 EOF analysis of the altimetry data

From the time series of sea level height, $H_k(t)$, and eastward surface velocity, $U_k(t)$, we can determine the dominant EOF (Empirical Orthogonal Function) modes. To avoid ending in the middle of a year, we terminate the analysis on 31st December 2018. Together, the three most dominant modes for sea level height, termed MAH-1, MAH-2, and MAH-3, explain almost 99% of the variance, whereas the first three modes for $U_k(t)$, termed MAU-1, MAU-2, and MAU-3, explain close to 92% (Table 5.2). The modes and their associated principal components have been normalized so that the standard deviation of each principal component is 1. The latitudinal variation of these modes is shown in Figure 5.2.

Table 5.2. Explained variance by each of the first three modes for sea level height (first three columns) and for eastward surface velocity determined by Eq. (5.1) (last three columns).

Sea level height			Eastward surface velocity		
MAH-1	MAH-2	MAH-3	MAU-1	MAU-2	MAU-3
0.881	0.072	0.035	0.518	0.323	0.077
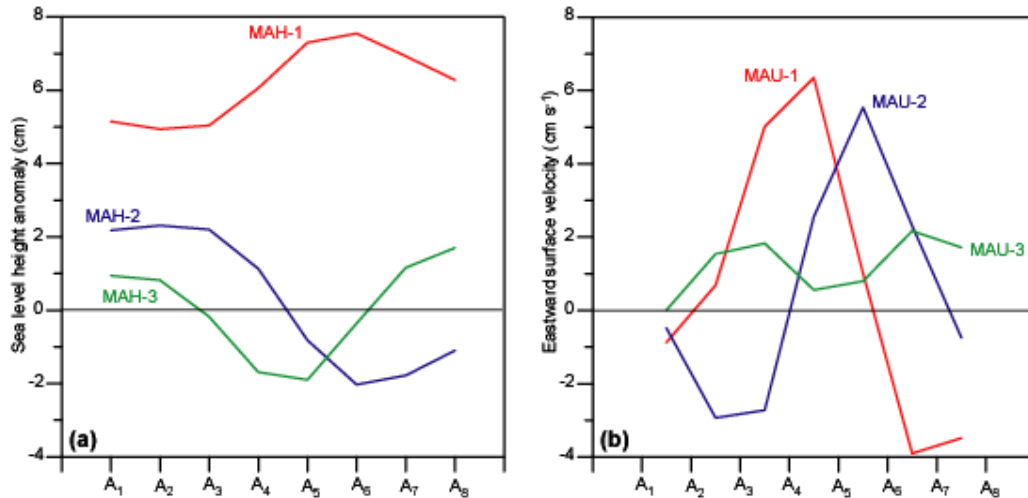
Figure 5.2. The first three EOF modes for sea level height **(a)** and for eastward surface velocity **(b)** along the monitoring section based on daily altimetry data 1993-2018.

The first – and highly dominant – EOF mode of sea level height (MAH-1) retains the same sign (positive by choice) all along the section (Figure 5.2a). In contrast, the first mode of eastward surface velocity (MAU-1) is less dominant (Table 5.2) and changes sign with latitude (Figure 5.2b).

Most of the principal components for the first three modes of both sea level height (termed PcAH-1, PcAH-2, and PcAH-3) and eastward surface velocity (termed PcAU-1, PcAU-2, and PcAU-3) show clear seasonality (Figure 5.3), but this is most pronounced for sea level height (Figure 5.3a).
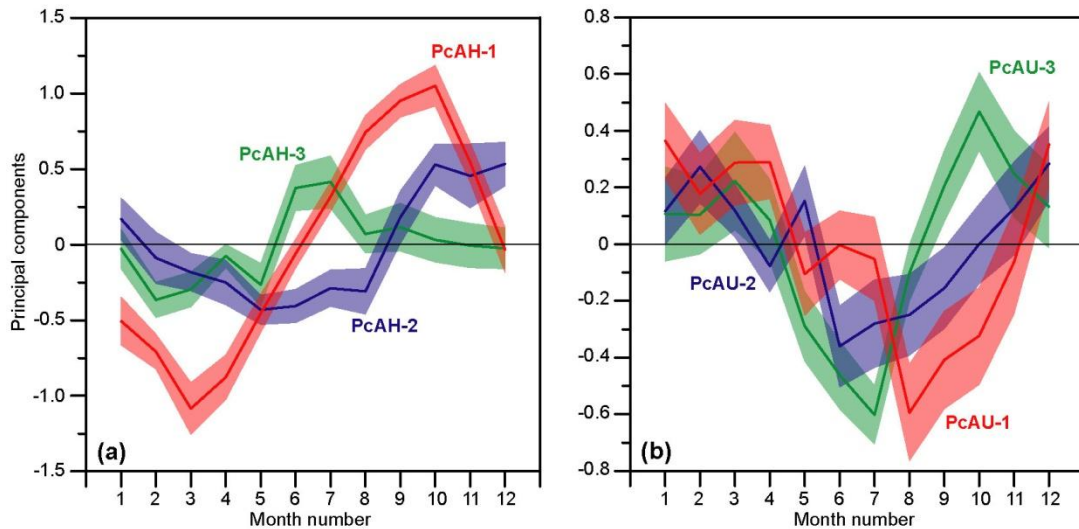
Figure 5.3. Seasonal variations of the principal components associated with the first three EOF modes for sea level height **(a)** and for eastward surface velocity **(b)** along the monitoring section based on daily altimetry data 1993-2018. The coloured lines show the average while the coloured areas show average ± one standard error.

The almost uniform latitudinal variation and the pronounced seasonality of the first sea level mode (red curves in Figure 5.2a and Figure 5.3a) indicates that this mode contains much of the seasonal warming and cooling (and hence expansion and contraction) of the water column. Comparing the red curve in Figure 5.3a with the curve in Figure 5.1b, we see a similar seasonal variation

.
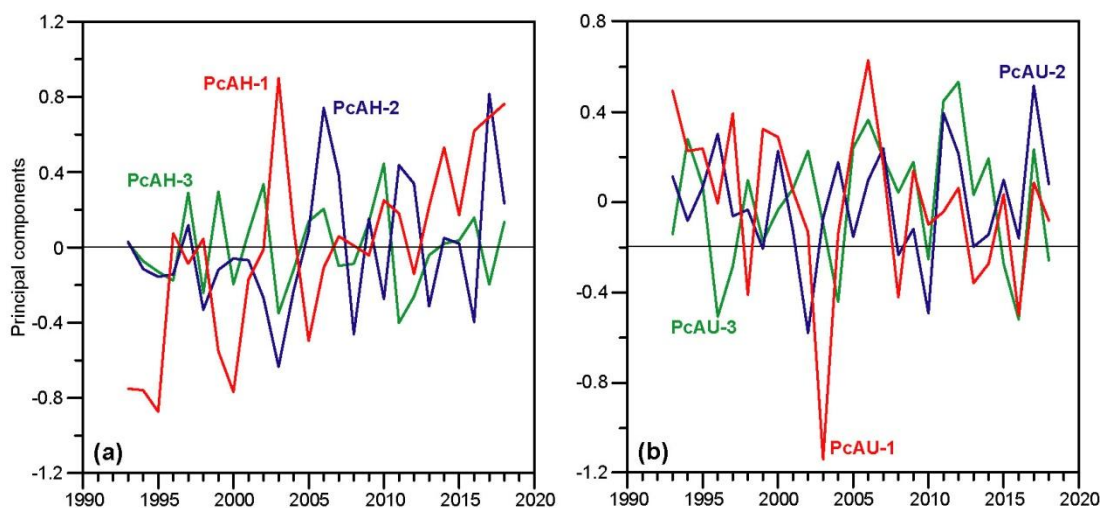
Figure 5.4. Annually averaged principal components associated with the first three EOF modes for sea level height **(a)** and for eastward surface velocity **(b)** along the monitoring section based on daily altimetry data 1993-2018.

On long time scales, the principal component associated with this mode, PcAH-1, has an increasing trend, although disrupted by the abnormal year 2003 (Figure 5.4a). None of the other sea level or velocity modes exhibit clear trends (Figure 5.4), and if we multiply the annually averaged PcAH-1 by the average values for MAH-1 (red curve in Figure 5.2a) between points A3 and A7, then the resulting curve (red curve in Figure 5.1a) is almost identical to the annually averaged sea level variation between these two points (black curve in Figure 5.1a). Thus this mode seems to contain almost all the sea level rise in the region.

On short time scales, the principal components of all modes retain fairly high autocorrelation up to lags of a week, especially the first mode for sea level (Figure 5.5). Correlating the principal components of the sea level modes with the velocity modes (Table 5.3), we see that the first sea level mode is only correlated with the first velocity mode, whereas the two other sea level modes are significantly correlated with all the velocity modes.

Table 5.3. Correlation coefficients between the principal components of the sea level modes and the velocity modes.

PcAH-1			PcAH-2			PcAH-3		
PcAU-1	PcAU-2	PcAU-3	PcAU-1	PcAU-2	PcAU-3	PcAU-1	PcAU-2	PcAU-3
-0.52***	-0.03	-0.08	0.64***	0.38***	0.47***	0.45***	-0.83***	-0.19***
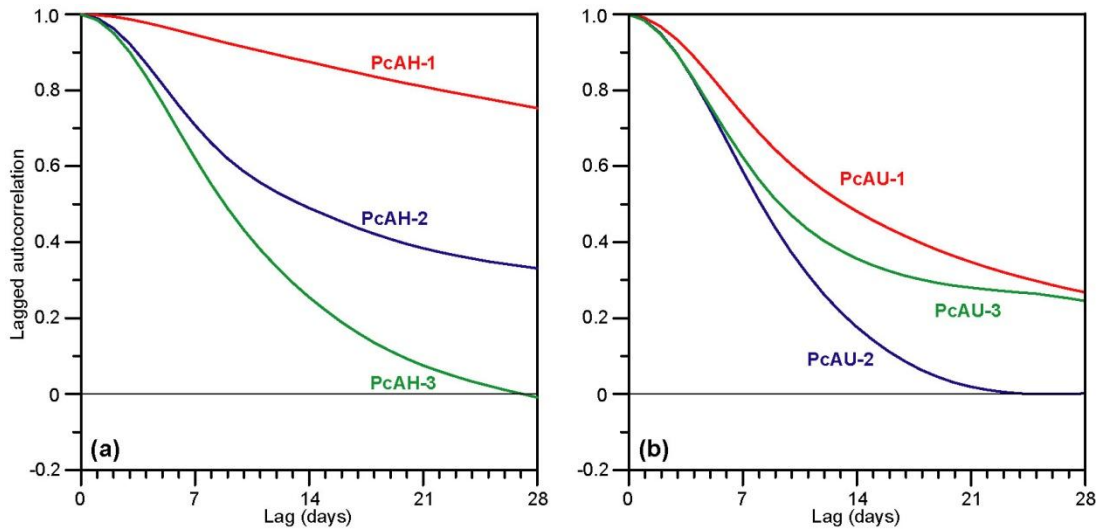
Figure 5.5. Lagged autocorrelation of the principal components associated with the first three EOF modes for sea level height **(a)** and for eastward surface velocity **(b)** along the monitoring section based on daily altimetry data 1993-2018.

5.3 Seasonal and long-term variations of altimetry parameters

From the altimetry data, we have generated 21 different time series of parameters in three groups: 8 sea level, 7 surface velocities, and 6 principal components. The trends and seasonal variations of these parameters may be determined in a combined procedure similar to Sect 2.3.2. Thus, parameter $p_k(t)$ ($k = 1,…,21$) is fitted to the equation:

$$p_k(t) = p_{0k} + \gamma_k \cdot t + A_k \cdot cos\left[2\pi \cdot (t - \frac{Day_k}{365})\right] \qquad (5.1)$$

in a step-wise manner, where t is the time in years since 1st January 1993. As seen in Table 5.4, Eq. (5.1) provides a good fit to the sea level parameters and PcAH-1, explaining around half the variance.

Table 5.4. Coefficients of the fits of the 21 selected altimetry parameters to Eq. (5.1) listing maximum correlation coefficient (R_{Max}) and the parameters of the fit. The trend γ_k is per year.

Parm:	Sea level height (cm)								Surface velocity (cm s^{-1})							PcAH-			PcAU-		
	h_1	h_2	h_3	h_4	h_5	h_6	h_7	h_8	U_1	U_2	U_3	U_4	U_5	U_6	U_7	1	2	3	1	2	3
R_{Max}:	0.77	0.75	0.71	0.67	0.65	0.66	0.68	0.69	0.26	0.14	0.20	0.34	0.23	0.16	0.20	0.73	0.34	0.16	0.28	0.19	0.23
γ_k:	0.28	0.26	0.27	0.30	0.33	0.32	0.30	0.28	0.04	-0.02	-0.08	-0.07	0.00	0.06	0.06	0.05	0.01	0.00	-0.01	0.00	0.00
A_k:	5.83	5.47	5.19	5.70	6.62	6.93	6.57	6.13	0.98	0.79	1.67	3.28	1.87	1.12	1.19	0.96	0.47	0.23	0.39	0.27	0.33
Day_k:	271	271	272	268	261	255	254	253	270	257	53	41	11	285	260	262	328	224	53	18	344

5.4 Altimetry and isotherm depth

Information on isotherm depth comes from two sources: CTD profiles and PIES data. The depths determined from CTD profiles have the benefit that they are direct measurements, but they are snapshots representing only the time that the CTD passes (usually on its way down) through the isotherm. As illustrated in Figure 2.5, the isotherms move vertically even on time scales less than an hour, although usually only a few tens of meters.

The isotherm depths from PIES data, on the other hand, are indirect and based on calibration with CTD data, but they are quasi-continuous and we can generate isotherm depths averaged over a day or longer periods for comparison with altimetry data.

5.4.1 Altimetry and isotherm depth from CTD profiles

To investigate links between altimetry and the depth of the 4°C-isotherm, isotherm depths from each CTD occupation of one of the sufficiently deep standard stations since 1993 have been correlated with sea level height at each of the eight altimetry points, surface velocity in each of the seven altimetry intervals, and the six principal components discussed in Sect. 5.2. Since the southernmost stations are shallow and usually filled by water warmer than 4°C all the way to the bottom, the correlation analyses were only made from station N04 northwards (Table 5.5a). For most of the stations, the highest correlations are with sea level at an altimetry point more or less directly above the station. This might be simply due to the fact that isotherm depth and sea level have similar seasonal variations (Figure 5.6) and to some extent also trends.
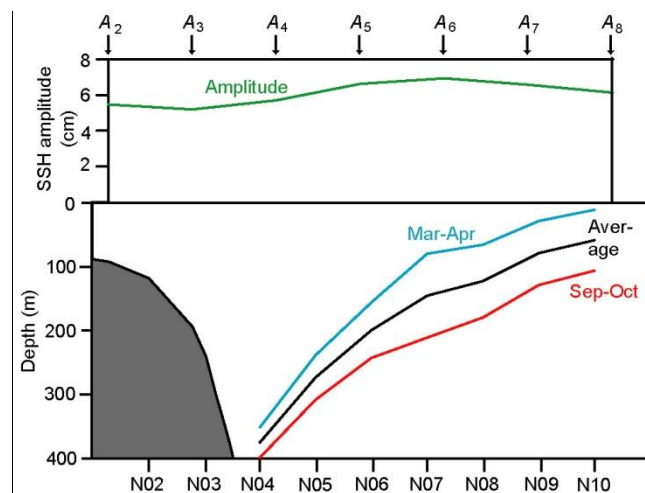
Figure 5.6. Seasonal variation of the 4°C-isotherm depth at stations N04-N10 (lower part) and sea level at points A_2-A_8 (upper part). The time of maximum (Day_j in Table 2.2 and Day_k in Table 5.4) varies somewhat, but is in September-October for most of the parameters (e.g., minimum is in March-April), which is illustrated by the red and cyan curves, respectively in the lower part of the figure. The green curve in the upper part illustrates the latitudinal variation of the seasonal amplitude in sea level.

Table 5.5a. Number of CTD profiles at stations N04 to N14 in the altimetry period and correlation coefficients between 4°C-isotherm depth from the profiles and various altimetry parameters. Profiles with surface temperature < 4°C are included with isotherm depth set to zero (ignoring CTD profiles with surface water colder that 4°C would generally have given slightly lower correlation coefficients). The highest correlation coefficients for each station and each of the three groups of parameters are bold while the overall maximum is bold and underlined.

Station:	N04	N05	N06	N07	N08	N09	N10	N11	N12	N13	N14
Number:	112	115	102	105	102	101	98	94	85	85	84
h_1:	0.33***	0.39***	0.39***	0.51***	0.55***	0.56***	0.60***	0.63***	**0.57*****	**0.61*****	**0.62*****
h_2:	0.34***	0.38***	0.38***	0.49***	0.52***	0.54***	0.58***	0.60***	0.54***	0.57***	0.59***
h_3:	0.43***	0.49***	0.44***	0.52***	0.51***	0.53***	0.55***	0.56***	0.50***	0.54***	0.55***
h_4:	**0.47*****	**0.66*****	0.61***	0.64***	0.55***	0.54***	0.56***	0.55***	0.45***	0.51***	0.50***
h_5:	0.39***	0.65***	**0.68*****	0.76***	0.66***	0.60***	0.60***	0.59***	0.44***	0.49***	0.50***
h_6:	0.28**	0.51***	0.59***	**0.77*****	**0.75*****	0.69***	0.65***	0.65***	0.47***	0.50***	0.53***
h_7:	0.23*	0.40***	0.45***	0.68***	0.75***	**0.74*****	0.68***	0.68***	0.50***	0.51***	0.56***
h_8:	0.22*	0.38***	0.38***	0.57***	0.67***	0.70***	**0.69*****	**0.69*****	0.55***	0.53***	0.59***
U_1:	0.05	0.19*	0.16	0.26**	0.31**	0.26**	0.27**	0.33**	**0.33****	**0.39*****	**0.35****
U_2:	-0.31***	-0.42***	-0.18	-0.07	0.11	0.09	0.15	0.20	0.18	0.15	0.23*
U_3:	-0.32***	**-0.69*****	-0.58***	-0.51***	-0.26**	-0.20	-0.21*	-0.13	-0.05	-0.08	-0.04
U_4:	0.01	-0.31**	-0.50***	-0.66***	-0.56***	-0.44***	-0.40***	-0.37***	-0.20	-0.20	-0.22*
U_5:	**0.33*****	0.42***	0.17	-0.15	-0.42***	-0.40***	-0.26*	-0.25*	-0.13	-0.08	-0.16
U_6:	0.30**	0.59***	**0.67*****	0.57***	0.23*	0.05	0.09	0.12	0.01	0.10	0.03
U_7:	0.15	0.27**	0.47***	**0.67*****	0.61***	0.42***	0.27*	0.24*	0.02	0.11	0.10
PcAH-1:	0.35***	0.53***	0.55***	**0.70*****	**0.69*****	**0.68*****	**0.67*****	**0.67*****	0.53***	0.57***	0.59***
PcAH-2:	0.22*	-0.00	-0.11	-0.25*	-0.24*	-0.19	-0.09	0.00	0.11	0.16	0.14
PcAH-3:	-0.34***	-0.55***	-0.44***	-0.24*	0.11	0.21*	0.18	0.19	0.21	0.14	0.22*
PcAU-1:	-0.17	-0.52***	**-0.63*****	-0.70***	-0.51***	-0.37***	-0.33**	-0.29**	-0.12	-0.16	-0.15
PcAU-2:	**0.37*****	0.50***	0.25*	-0.04	-0.33***	-0.32**	-0.22*	-0.23*	-0.15	-0.10	-0.18
PcAU-3:	0.06	-0.06	0.18	0.18	0.06	-0.10	-0.08	0.03	-0.03	0.06	0.03

To check how much of the correlations in Table 5.5a can be explained by similar seasonal variations and trends, both isotherm depth and the altimetry parameters have been de-trended and de-seasoned based on Eq. (2.2) with parameters in Table 2.2 and on Eq. (5.1) with parameters in Table 5.4. After this, the correlations were recalculated (Table 5.5b).

Table 5.5b. The same as Table 5.5a except that the trends and seasonal variations have been removed from both isotherm depth and the altimetry parameters before correlation.

Station:	N04	N05	N06	N07	N08	N09	N10	N11	N12	N13	N14
Number:	112	115	102	105	102	101	98	94	85	85	84
h_1:	0.18	0.22*	0.13	0.15	0.24*	0.25*	0.16	0.22*	0.30**	**0.26***	**0.23***
h_2:	0.19*	0.20*	0.11	0.12	0.19	0.22*	0.13	0.17	0.25*	0.19	0.17
h_3:	0.34***	0.38***	0.22*	0.19	0.18	0.22	0.12	0.13	0.21	0.17	0.12
h_4:	**0.42*****	**0.65*****	0.49***	0.42***	0.28*	0.25*	0.19	0.15	0.18	0.15	0.08
h_5:	0.31***	0.65***	**0.62*****	0.62***	0.47***	0.36**	0.30**	0.25*	0.19	0.15	0.10
h_6:	0.15	0.44***	0.50***	**0.65*****	**0.64*****	0.51***	0.38***	0.34**	0.22	0.15	0.13
h_7:	0.07	0.28**	0.27**	0.48***	0.64***	**0.59*****	**0.43*****	0.38***	0.27*	0.14	0.16
h_8:	0.06	0.25*	0.15	0.28**	0.50***	0.54***	0.43***	**0.40*****	**0.34****	0.17	0.21
U_1:	-0.03	0.10	0.06	0.13	0.18	0.12	0.10	0.18	**0.21**	**0.25***	**0.21**
U_2:	-0.37***	-0.50***	-0.27**	-0.19	-0.01	-0.00	0.03	0.10	0.08	0.05	0.12
U_3:	-0.30**	**-0.69*****	-0.59***	-0.52***	-0.25*	-0.14	-0.18	-0.09	-0.03	-0.03	0.02
U_4:	0.08	-0.25*	-0.46***	-0.62***	-0.52***	-0.33**	**-0.31****	-0.28**	-0.10	-0.06	-0.06
U_5:	0.36***	0.49***	0.27**	-0.06	-0.40***	**-0.36*****	-0.20	-0.21*	-0.07	0.01	-0.07
U_6:	0.25**	0.56***	**0.66*****	0.60***	0.19	-0.05	-0.01	0.00	-0.04	0.05	-0.04
U_7:	0.06	0.17	0.38***	**0.64*****	0.56***	0.32**	0.13	0.08	-0.11	-0.03	-0.06
PcAH-1:	0.24*	0.48***	0.43***	0.51***	**0.52*****	**0.47*****	**0.35****	**0.32****	**0.28***	0.20	0.17
PcAH-2:	0.15	-0.08	-0.21*	-0.40***	-0.43***	-0.33**	-0.28**	-0.21*	-0.02	0.05	0.01
PcAH-3:	-0.37***	-0.62***	-0.56***	-0.40***	0.02	0.16	0.09	0.13	0.13	0.03	0.12
PcAU-1:	-0.11	-0.48***	**-0.60*****	**-0.69*****	-0.47***	-0.26**	-0.23*	-0.18	-0.03	-0.05	-0.01
PcAU-2:	**0.41*****	0.57***	0.34***	0.07	-0.27**	-0.27*	-0.15	-0.19	-0.08	-0.01	-0.09
PcAU-3:	-0.02	-0.13	0.14	0.18	-0.02	-0.19	-0.21*	-0.12	-0.13	0.00	-0.04

Comparing Table 5.5a and Table 5.5b, we see that the correlation coefficients generally decrease after de-trending and de-seasoning, but most of them remain fairly high and highly significant. For N04, the

already weak link between isotherm depth and altimetry is weakened further, but stations N05, N06, N07, and N08 retain correlation coefficients above 0.6.

Even after de-trending and de-seasoning, the correlations with sea level remain positive. To some extent, this may be because our method does not cover non-linear long-term variations or non-sinusoidal seasonal variations, but the irregular character of the isotherm depth data (Figure 2.6) does not allow many alternatives.

For stations N05, N06, and N07, the highest de-trended and de-seasoned correlations are with some aspect of surface velocity and they are generally negative. When the surface velocity in the core of the current (represented by U_3 and U_4, Hansen et al., 2019a) speeds up, the 4°C-isotherm tends to become shallower throughout the southern part of the section, reducing the effect of velocity variations on Atlantic water volume transport (cf., Sect. 4.3).

In addition to these negative correlations between isotherm depth at a station and surface velocity above or inside of the station, we see highly significant positive correlations between isotherm depth and surface velocity farther north on the section (e.g., between isotherm depth at N06 and U_6). The reason for these positive correlations is, no doubt, that the surface velocities in the southern and the northern parts of the section are anti-correlated (Table 5.6), which again will tend to reduce the effect on Atlantic water volume transport.

Table 5.6. Correlation coefficients between eastward surface velocities in different altimetry intervals. Using de-trended and de-seasoned values would not change the correlations notably.

	U_2	U_3	U_4	U_5	U_6	U_7
U_1:	0.37***	-0.25***	-0.37***	-0.13**	0.14***	0.13***
U_2:		0.58***	-0.13**	-0.57***	-0.32***	-0.02
U_3:			0.62***	-0.26***	-0.72***	-0.46***
U_4:				0.51***	-0.52***	-0.73***
U_5:					0.36***	-0.31***
U_6:						0.69***

When the surface velocity in one of the altimetry intervals (e.g., U_3) is strong towards the east, the eastward velocity two intervals (i.e. ≈50 km) farther north is weaker or towards the west. This may partly be due to meso-scale activity, which has a long history in this region (Hansen and Meincke, 1979).

Associated with the spatial correlations in Table 5.6, we would expect temporal correlations, as well, and they are indeed to be found as exemplified in Figure 5.7, which illustrates the relationships between U_3 and surface velocities in the other altimetry intervals (Figure 5.7a), as well as between U_3 and sea level height at all the altimetry points (Figure 5.7b).

As shown by the black curve in Figure 5.7a, the autocorrelation of U_3 decreases from 1 to 0.5 at a lag ≈ 10 days and this is the dominant time scale of Figure 5.7. This is also the time scale of the principal component (PcAU-2, Figure 5.5b) of the second EOF mode of the eastward surface velocity (MAU-2, Figure 5.2b), which has the structure of a circulating eddy with a spatial scale somewhat larger than 50 km. In contrast to the two other velocity modes, the autocorrelation of PcAU-2 is ≈ 0 for lags of 3-4 weeks (Figure 5.5b) so that it should not contribute much to monthly averages.

This "Eddy mode" explained 32% of the variance of the eastward surface velocity (Table 5.2) and a histogram of its principal component is seen to be asymmetrical with substantially higher occurrence of strongly negative than positive values (Figure 5.8a). Since the principal component is to be multiplied by the mode (blue curve in Figure 5.2b) to get the eastward surface velocity anomaly associated with the mode, this implies stronger cyclonic than anti-cyclonic meso-scale features.
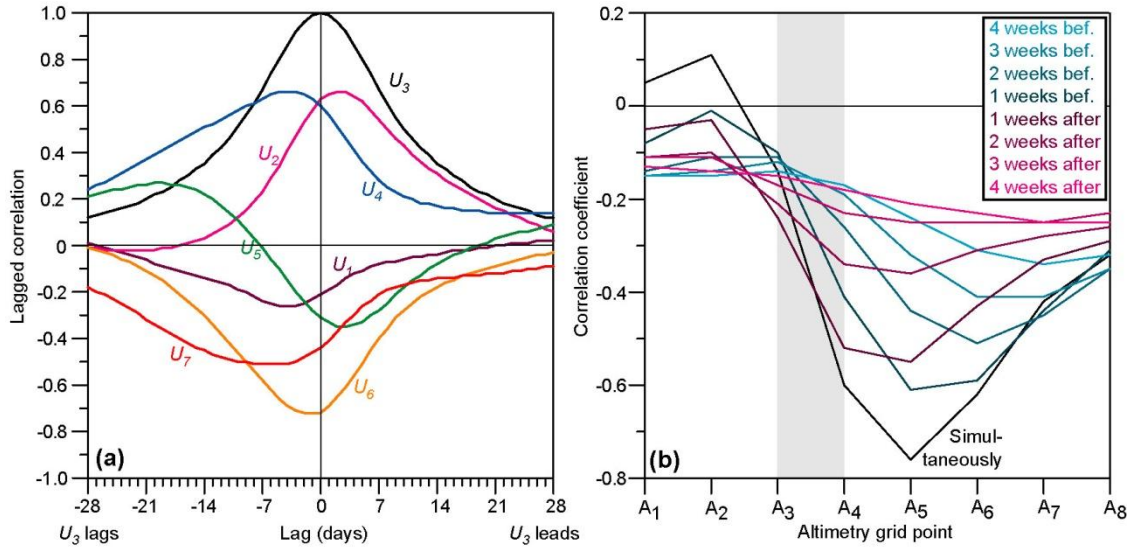
Figure 5.7. (a) Lagged correlation between U_3 and the surface velocities in all the altimetry intervals. **(b)** Correlation between U_3 and sea level height at all the altimetry points from 4 weeks before to 4 weeks after. The grey area indicates the altimetry interval for U_3. All the data have been de-trended and de-seasoned before correlation.

We define an "eddy" to be an occurrence of $|\text{PcAU-2}| > 2$ (Figure 5.8a). By this definition, there were considerably more and longer lasting cyclonic than anti-cyclonic eddies. Of the 9629 days in our altimetry data set, there were 331 days with PcAU-2 < -2 compared to 173 days with PcAU-2 > +2. If an eddy passage through the section is defined as a period of contiguous days satisfying one of the two eddy-criteria, there were 43 cyclonic and 32 anti-cyclonic eddies passing through the section. Most of the eddy passages lasted less than a week, but two of the cyclonic eddies used more than 3 weeks to pass (Figure 5.8b).
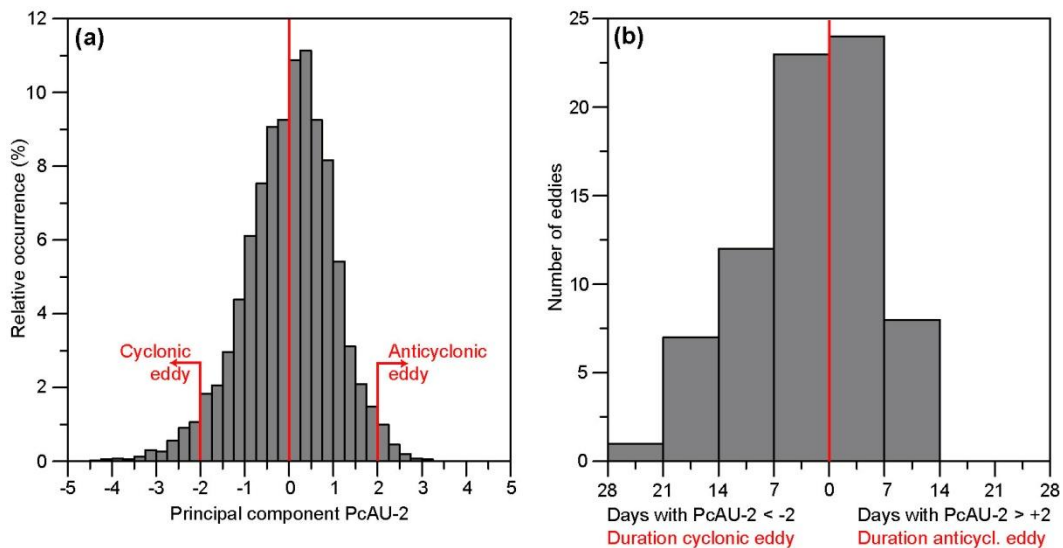
Figure 5.8. (a) Histogram of the principal component PcAU-2. Eddies are defined as having PcAU-2 < -2 (cyclonic eddy) or PcAU-2 > +2 (anticyclonic eddy). **(b)** Number of eddies passing through the section with duration of 1, 2, 3, or 4 weeks.

Returning to Table 5.5b, we find significant positive correlations between PcAU-2 and 4°C-isotherm depth for stations N04, N05, and N06, whereas stations N08 and northwards have negative correlations, although less significant. Thus, a cyclonic eddy would tend to deepen the isotherm in the southern part and make it shallower around stations N08 and N09. None of the correlation coefficients between PcAU-2 and isotherm depth are very high, however, and the meso-scale activity associated with this EOF mode only explains a part of the isotherm depth variations even for the de-trended and de-seasoned data.

As seen in Table 5.5, the 4°C-isotherm depth at a station is generally well correlated with the sea level height at altimetry points more or less directly above the station. To check for possible lags, we have interpolated sea level latitudinally between altimetry points to produce time series, $h_j(t)$, of sea level directly at each station (j) and calculated lagged correlation coefficients (Figure 5.9a). For stations N05 – N08, the zero-lag correlations are fairly high, consistent with Table 5.5b. For these stations, there may be a lag of a couple of days, but its statistical significance is doubtful. Thus the isotherm depth at a station is generally in phase with sea level height directly above the station.
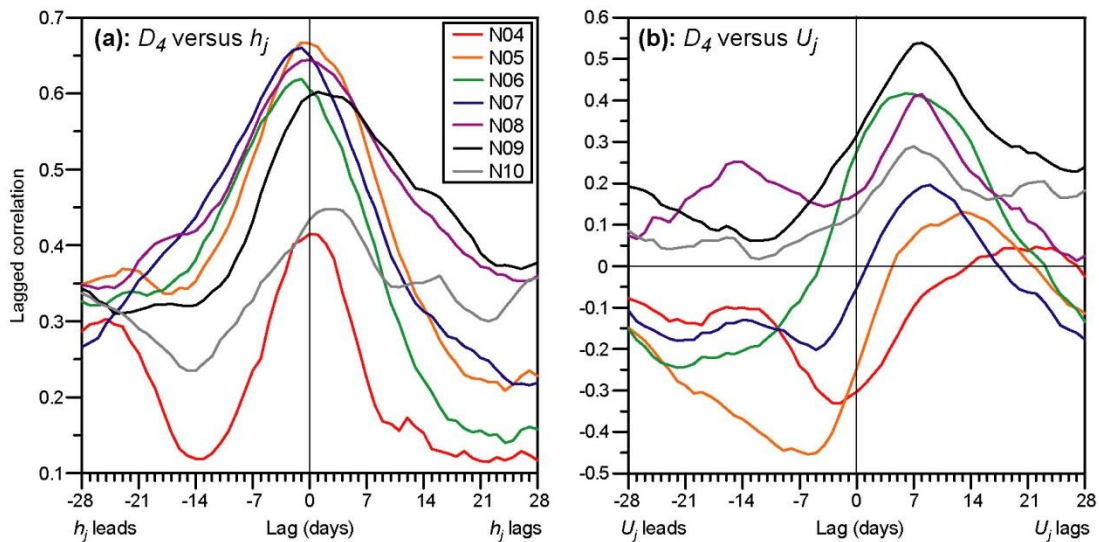
Figure 5.9. (a) Lagged correlation between the depth of the 4°C-isotherm at stations N04 – N10, D_4, and sea level just at the station, h_j. (b) Lagged correlation between the depth of the 4°C-isotherm, D_4, and eastward surface velocity in the altimetry interval including the station, U_j. All the data have been de-trended and de-seasoned before correlation.

If, instead, isotherm depth at a station is lag-correlated with the eastward surface velocity in the altimetry interval that includes the station, U_j, the picture is quite different (Figure 5.9b). Zero-lag correlations are generally weak and may be either positive or negative. Most of the stations, however, have a peak in the cross-correlation function when U_j lags isotherm depth by $\approx$ 1 week. For N04 and especially N05, we also see fairly strong negative correlations when U_j leads isotherm depth by a few days.

These lagged correlations may again be interpreted in terms of eddies passing through the section. These passages are likely to induce lagged correlations between sea level and eastward surface velocity, as indeed is the case (Figure 5.10). Thus, one way to interpret the lagged correlations between isotherm depth and surface velocity in Figure 5.9b is that they are a result of the $\approx$zero-lag link between sea level and isotherm depth (Figure 5.9a) combined with the lagged link between sea level and velocity (Figure 5.10).
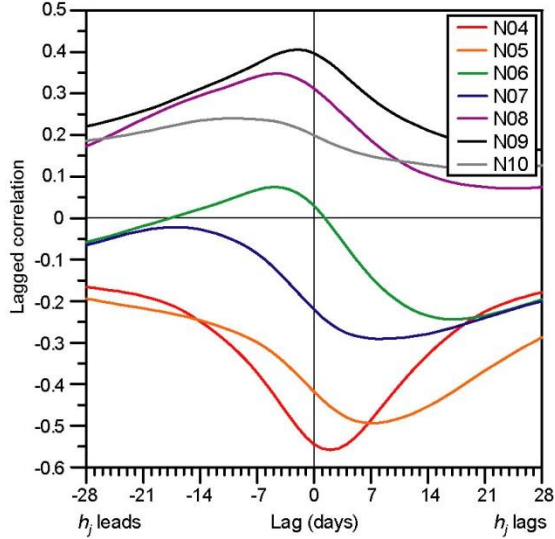
Figure 5.10. Lagged correlation between the sea level just at stations N04 – N10, h_j, and eastward surface velocity in the altimetry interval including the station, U_j. All the data have been de-trended and de-seasoned before correlation.

5.4.2 Simulating isotherm depth from CTD profiles by altimetry

Taking this into account, it does not appear fruitful to try lagged regression models for simulating the 4°C-isotherm depth, $D_j(t)$ at station j. Instead, we try to simulate $D_j(t)$ as a linear combination of a slowly varying function of time, $\Gamma_j(t)$, a sinusoidal seasonal variation, sea level interpolated to the latitude of the standard station, $h_j(t)$, and one additional altimetry parameter, $x_j(t)$, where both $h_j(t)$ and $x_j(t)$ have been de-trended and de-seasoned:

$$D_j(t) = \Gamma_j(t) + A_j \cdot cos\left[2\pi \cdot \left(t - \frac{Day_j}{365}\right)\right] + a_{h,j} \cdot h_j(t) + a_{x,j} \cdot x_j(t) + a_{0,j} \tag{5.2}$$

At this stage, it might seem natural to assume a linear trend for $\Gamma_j(t)$ ($\Gamma_j(t) = \Gamma_{0,j} + \gamma_j \cdot t$), but from Sect. 2.2.2 it appears that the long-term variations of $D_j(t)$ are not very linear in time for all the stations. Instead, we use the iterative algorithm described in Appendix A to split the slow depth variations into sinusoidal seasonal variations and 3-year running means and use the 3-year running means to represent $\Gamma_j(t)$ for each station (Figure 5.11).
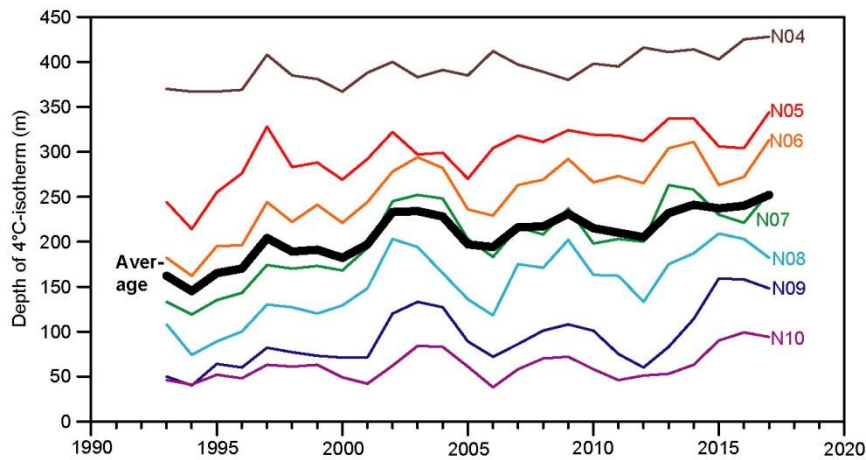
Figure 5.11. Three-year running mean of de-seasoned depth (Appendix A) of the 4°C-isotherm, $\Gamma_j(t)$, 1994 – 2017 at stations N04 to N10. The thick black curve is the average of all the other curves.

The performance of the iterative splitting of the slow isotherm depth variations may be assessed by the maximum correlation coefficient, R_{max}, obtained by varying the time of maximum, Day_j, through the year. As seen in Table 5.7, R_{max} is not very high for the southernmost stations (N04 to N06), indicating that short-term variations dominate strongly over the slow variations. For stations N07 to N10, long-term and seasonal variations explain more of the variance, but still less than half, even for N10 ($0.69^2 = 0.48$).

Table 5.7. The "slow" variations of the 4°C-isotherm depths at stations N04 to N10. The top three lines document the results of the iterative splitting (Appendix A), listing the maximum correlation coefficient (R_{max}) and the amplitude (A_j) and time of maximum (Day_j) of the seasonal variation based on all isotherm depths observed by CTD 1987 – 2018. The next two lines list the correlation coefficients between the 3-year running mean, $\Gamma_j(t)$, and time ($R_{Yr,j}$) as well as Atlantic water temperature ($R_{TA,j}$). The bottom four lines list the explained variance (R^2) and the coefficients of the fit in Eq. (5.3). The values in the bottom six lines are based on the period 1993 – 2017. Profiles with surface temperature < 4°C are included with isotherm depth set to zero.

Station:	N04	N05	N06	N07	N08	N09	N10
R_{max}:	0.24	0.24	0.35	0.52	0.48	0.51	0.69
A_j (m):	25	32	45	65	56	48	48
Day_j:	298	294	283	262	269	262	270
$R_{Yr,j}$:	0.79	0.75	0.81	0.77	0.76	0.67	0.52
$R_{TA,j}$:	0.37	0.66	0.73	0.70	0.62	0.37	0.21
R^2:	0.62	0.64	0.76	0.70	0.63	0.44	0.27
γ_j (m/yr):	1.97	2.33	3.20	3.16	3.12	3.00	1.21
$a_{TA,j}$ (m/°C):	0.0	30.6	44.0	45.1	30.4	0.0	0.0
$d_{0,j}$ (m):	369	271	214	163	115	57	47

Since they are derived in a different way, the seasonal amplitudes, A_j, and times of maximum, Day_j, differ from the values in Table 2.2, but the differences are marginal. From Figure 5.11, the $\Gamma_j(t)$ functions for all of the stations seem to have increasing trends and this is verified by calculating the correlation coefficients, $R_{Yr,j}$, between annual values for $\Gamma_j(t)$ and the year (Table 5.7). For some of the stations, however, the $\Gamma_j(t)$ variations show similarities to the variations of the Atlantic water temperature, $T_A(t)$, (Figure 2.2a). The correlation coefficient between these two parameters, $R_{TA,j}$, is fairly high for stations N05 to N08, but not for N04 or N09 and N10 (Table 5.7). Combining these two relationships, we can try to fit $\Gamma_j(t)$:

$$\Gamma_j(t) = d_{0,j} + \gamma_j \cdot t + a_{TA,j} \cdot [T_A(t) - \langle T_A \rangle] \qquad (5.3)$$

where $\langle T_A \rangle$ is the average value of $T_A(t)$ for the 1993 – 2017 period, 8.336°C. Based on the values for $R_{TA,j}$ in Table 5.7, the coefficient, $a_{TA,j}$, is set to zero for N04, N09, and N10, and the other two coefficients for these stations are determined by simple linear regression. For stations N05 to N08, all the coefficients are determined by multiple linear regression. The coefficients, as well as the explained variances (R^2) are listed in the four bottom rows of Table 5.7.

It might seem evident that it would always be better to use the raw values for $\Gamma_j(t)$ each year, i.e., the 3-year running mean values from the iterative splitting (Figure 5.11), rather than the values fitted by Eq. (5.3). The raw values have considerable uncertainties, however. For most of the stations, twice the standard error of $\Gamma_j(t)$ (often used as a 95% confidence interval) was more than 50 m. We therefore try both alternatives and compare them with the results of doing no de-trending or de-seasoning.

As a first attempt to use Eq. (5.2), we set $a_{x,j} = 0$ and determine the $a_{h,j}$ and $a_{0,j}$ coefficients. To do this, the first two terms on the right hand side of Eq. (5.2) are subtracted from the left hand side and the coefficients determined by linear regression. The correlation coefficients are listed in the three rows in

Table 5.8. The two bottom rows in the table use the two alternative ways to assign values to $\Gamma_j(t)$, whereas the top row is without any de-trending or de-seasoning to provide base values.

Table 5.8. Correlation coefficients between the 4°C-isotherm depths at stations N04 to N10 and sea level interpolated to the latitude of the station, $h_j(t)$. In the top row (Raw data), no de-trending or de-seasoning has been performed. In the other two rows, $h_j(t)$ has been de-trended and de-seasoned while isotherm depth has been de-seasoned and $\Gamma_j(t)$ subtracted before correlation. In the middle row, the $\Gamma_j(t)$ value used for each year is the 3-year running mean (Figure 5.11). In the bottom row, the $\Gamma_j(t)$ value used for each year is calculated from Eq. (5.3) with coefficients from Table 5.7. Profiles with surface temperature < 4°C are included with isotherm depth set to zero.

Station:	N04	N05	N06	N07	N08	N09	N10
Raw data:	0.47***	0.67***	0.66***	0.78***	0.76***	0.73***	0.69***
Γ_j 3-year R-mean:	0.49***	0.68***	0.69***	0.79***	0.76***	0.75***	0.76***
Γ_j from Eq.(5.3):	0.51***	0.71***	0.71***	0.78***	0.77***	0.74***	0.73***

Generally, the correlations seem to increase with de-trending and de-seasoning, but not by very much. Neither is it evident, what method for assigning values to $\Gamma_j(t)$ is preferable. In the following, we therefore retain the three alternative ways to treat de-trending and de-seasoning. The explanatory power of each fit (R^2) is seen to be low for N04, but for the other stations, the fits are seen to explain around 50 – 60 % of the variance.

The values for R^2 with $a_{x,j} = 0$ in Eq. (5.2) are listed in the top rows of Tables C5 in Appendix C with heading "None". The rest of Tables C5 lists R^2 with different choices for $x_j(t)$ and with the three alternatives for de-trending and de-seasoning. For N09 and N10, the inclusion of $x_j(t)$ makes only negligible improvements. For the other stations, there are improvements for some choices of $x_j(t)$. The best choice for $x_j(t)$ is, however, not obvious for any of the stations.

For stations N04 to N08, the combination of sea level at the station, $h_j(t)$, and the first sea level EOF mode, PcAH-1, is one of the combinations with most explanatory power. The explanatory power, R^2, and the coefficients of the fits for this combination are listed in the top five rows of Table 5.9. The next six rows list the same information for some combination of sea level at the station, $h_j(t)$, and the surface velocity in one of the intervals. For N09 and N10, only the combination with $a_{x,j} = 0$ is listed in Table 5.9 since the inclusion of an $x_j(t)$ did not increase the explained variance to any appreciable degree as seen in Table C5.

Table 5.9. Explained variance (R^2) and the coefficients in Eq. (5.2) for selected parameters $x_j(t)$ for each station and for the three alternative methods for treating de-trending and de-seasoning. The unit for $a_{h,j}$ is (m/cm). For $a_{x,j}$ it is (m/(cm/s)) if $x_j(t)$ is a velocity; otherwise it is (m). The unit for $a_{0,j}$ is (m). Profiles with surface temperature < 4°C are included with isotherm depth set to zero and fitted values giving negative isotherm depth are also set to zero before evaluating the explanatory power.

Stat	N	$x_j(t)$	Raw data R^2	$a_{h,j}$	$a_{x,j}$	$a_{0,j}$	Γ_j 3-year R-mean R^2	$a_{h,j}$	$a_{x,j}$	$a_{0,j}$	Γ_j from Eq.(5.3) R^2	$a_{h,j}$	$a_{x,j}$	$a_{0,j}$
N04	112	PcAH-1	0.31	16.20	-66.76	332	0.29	14.43	-58.46	-4	0.31	15.22	-60.30	-4
N05	115	PcAH-1	0.62	33.04	-163.29	165	0.60	32.42	-166.82	-14	0.62	31.78	-151.38	-14
N06	102	PcAH-1	0.53	23.89	-114.52	154	0.59	26.52	-159.43	-10	0.58	25.11	-135.41	-9
N07	105	PcAH-1	0.63	19.18	-70.08	129	0.67	20.09	-104.13	-3	0.66	20.11	-94.09	-2
N08	102	PcAH-1	0.59	15.58	-42.82	92	0.60	15.71	-57.52	-2	0.63	17.62	-63.33	-2
N05	115	U_5	0.58	9.88	6.82	255	0.56	10.46	6.03	-12	0.60	11.75	5.75	-12
N05	115	U_3	0.56	5.88	-7.74	265	0.57	4.88	-8.45	-9	0.60	6.88	-7.57	-10
N06	102	U_6	0.57	6.18	8.36	217	0.61	3.80	9.44	-12	0.60	5.63	8.28	-12
N07	105	U_7	0.65	8.06	6.93	169	0.68	5.05	7.97	-4	0.66	6.59	7.08	-4
N07	105	U_6	0.65	9.00	4.86	164	0.69	5.99	5.89	-8	0.67	7.44	5.21	-7
N08	102	U_7	0.62	8.20	5.45	116	0.62	6.57	5.50	-6	0.64	8.16	4.89	-6
N09	101	None	0.54	0.07	0.00	-3	0.57	6.78	0.00	-1	0.56	8.72	0.00	-0
N10	98	None	0.47	0.08	0.00	-2	0.58	3.13	0.00	-0	0.54	4.37	0.00	0

To illustrate the performance of the fits, Figure 5.12 compares observed and fitted isotherm depths for a selected parameter combination for each station, where $\Gamma_j(t)$ in every case was calculated from Eq. (5.3). As expected from Table 5.7, the fit for N04 is not very successful and it appears that this fit mainly fails when the observed isotherm is exceptionally shallow. For stations N05 to N08, the fits perform much better, but again tend to give too deep isotherms, when they should be shallow. The same tendency is seen for stations N09 and N10, but there, the fit apparently also fails to produce deep isotherms.
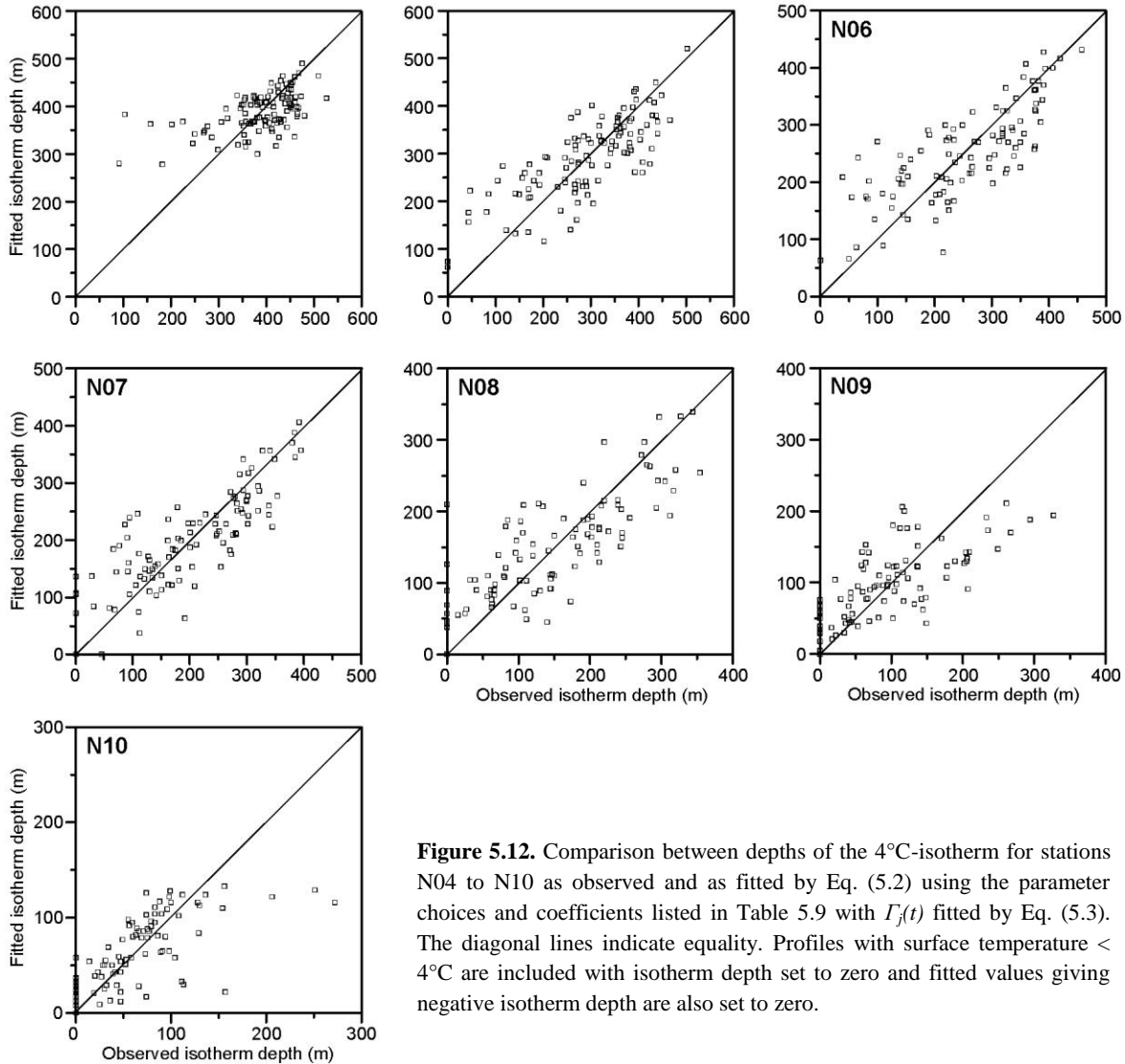
Figure 5.12. Comparison between depths of the 4°C-isotherm for stations N04 to N10 as observed and as fitted by Eq. (5.2) using the parameter choices and coefficients listed in Table 5.9 with $\Gamma_j(t)$ fitted by Eq. (5.3). The diagonal lines indicate equality. Profiles with surface temperature < 4°C are included with isotherm depth set to zero and fitted values giving negative isotherm depth are also set to zero.

The values for R^2 in Table 5.9 may be compared with the previously used fits (Table 4.2.1 in the Supplement of Hansen et al., 2015). The data material in Table 5.9 is more comprehensive and this newer table also includes additional parameter choices as well as the de-trending and de-seasoning before fitting. For most of the stations, the explained variance (R^2) is higher in Table 5.9 than in Hansen et al. (2015). The main exception is for N04, where the fit in Hansen et al. (2015) included the observed bottom temperature at mooring site NE.

5.4.3 Altimetry and isotherm depth from PIES data

From the PIES, we have observations at two sites (N05 and N07) and over a shorter period than for the CTD data set, but the PIES data are continuous and may be averaged to reduce short-term variations, e.g. from eddies. We only consider the data for the period with available altimetry data, which reduces both of the PIES data series by 25 days. For the transport estimates, we focus on monthly time scales and average over 28 days, which gives time series with 22 values at N05 and 20 values at N07.

Table 5.10. Characteristics of the original daily averaged (Daily), the 28-day averaged (28-day), and the 28-day averaged and de-seasoned (28-des) time series of 4°C-isotherm depth at N05 and N07 based on PIES data. "N" is the number of values. "Avg" is the average. "Std" is the standard deviation. "Range" lists minimum and maximum depth.

	N05				N07			
Series	N	Avg	Std	Range	N	Avg	Std	Range
Daily:	620	330m	83m	127-462m	569	217m	69m	75-367m
28-day:	22	330m	54m	226-412m	20	217m	52m	124-306m
28-des:	22	330m	45m	244-413m	20	222m	46m	119-299m

As expected, the averaging reduces both the standard deviation and the range of isotherm depth (Table 5.10). A further reduction in standard deviation is obtained when the 28-day averaged have been de-seasoned (last row in Table 5.10). This de-seasoning was carried out in a similar manner to that in Sect 2.3.2 by varying the day of maximum to get maximum correlation, but no long-term variation was considered since the PIES period was so short. As seen in Table 5.11, the 28-day averaging has little effect on the seasonal amplitude (A_j) or time of maximum depth (Day_j), but increases the maximum correlation coefficient, indicating a better seasonal fit.

Table 5.11. Fitting of 4°C-isotherm depth from PIES data to a sinusoidal seasonal variation, Eq. (2.2) with $\gamma_j = 0$, for both the original daily averaged (Daily) and the 28-day averaged (28-day) data. R_{Max} is the maximum correlation coefficient obtained when varying the time of maximum depth through the year.

	N05				N07			
Series	R_{Max}	D_{0j}	A_j	Day_j	R_{Max}	D_{0j}	A_j	Day_j
Daily:	0.35	330m	39m	277	0.34	223m	35m	250
28-day:	0.56	330m	40m	277	0.47	222m	35m	250

Comparing Table 5.11 with Table 2.2 and Table 5.7, we find similar values for the time of maximum depth (Day_j), which is encouraging. The seasonal amplitude (A_j) is also similar for N05, but not for N07. Since both PIES time series are shorter than two years (especially for N07), this discrepancy was not unexpected. The largest difference between the two tables is, however, in the offset (D_{0j}), which is much higher in Table 5.11 for both N05 and N07. Taking into account the effect of the long-term trends in the 25-year period from 1993 to 2018, this was also to be expected.

We now repeat the calculations leading to Table 5.5, using the 28-day averaged isotherm depths from the PIES instead of isotherm depths from CTD profiles. Since the averaging should reduce short-term variations, we might expect higher correlations and that is indeed generally the case (Table 5.12). Fortunately, the highest correlations in Table 5.5 and Table 5.12 generally are seen for the same altimetry parameters (and with the same signs), which provides a good consistency check.

Table 5.12. Correlation coefficients between 28-day averaged 4°C-isotherm depth from the PIES data and various altimetry parameters. The highest correlation coefficients for each station and each of the three groups of parameters are bold while the overall maximum is bold and underlined. For each of the PIES sites, there is one column for the original 28-day averaged series (28-day) and one column for which both isotherm depth and altimetry parameters have been de-seasoned (De-seas).

Site:	N05		N07	
Series:	28-day	De-seas	28-day	De-seas
h_1:	0.63*	0.35	0.57*	0.43
h_2:	0.61*	0.29	0.58*	0.44
h_3:	0.69**	0.48*	0.62*	0.51*
h_4:	**0.83***	0.75***	0.70**	0.60**
h_5:	0.83***	**0.77***	0.82***	0.72***
h_6:	0.71**	0.60**	**0.88***	**0.76***
h_7:	0.57*	0.39	0.81**	0.66**
h_8:	0.47	0.25	0.65*	0.44
U_1:	0.54*	0.30	0.18	-0.09
U_2:	-0.39	-0.74***	-0.08	-0.33
U_3:	-0.71***	**-0.80***	-0.40	-0.42
U_4:	-0.28	-0.40	-0.50	-0.54*
U_5:	0.53*	0.43	-0.16	-0.24
U_6:	**0.79***	0.71***	0.53*	0.52*
U_7:	0.57**	0.47*	**0.77***	**0.78**
PcAH-1:	**0.73**	0.59**	**0.79**	**0.68***
PcAH-2:	0.28	-0.11	-0.01	-0.27
PcAH-3:	-0.70***	**-0.73***	-0.20	-0.32
PcAU-1:	-0.62**	-0.68**	-0.65**	-0.66**
PcAU-2:	0.62*	0.62**	-0.07	-0.05
PcAU-3:	0.38	0.05	0.30	0.22

We therefore use the same strategy as before and try to fit the 28-day averaged isotherm depths from the PIES data to Eq. (5.2) with various choices for $x_j(t)$. The value for $\Gamma_j(t)$ ought to be fairly constant through the PIES period, equal to $\Gamma_j(2018)$, but since we have used two alternative methods to evaluate $\Gamma_j(t)$, we set $\Gamma_j(t)$ to zero, which means that the offset in the regression is solely $a_{0,j}$.

The result is listed in Table 5.13, which shows that the inclusion of both $h_j(t)$ and $x_j(t)$ in the fit may explain considerably more of the variance than using only $h_j(t)$ (compare the column labelled "None" with the bold underlined column). All the values in Table 5.13 are considerably higher than the analogous values in Table C5 based on the CTD data, but the two tables show similar relative variation of R^2 between the different choices for $x_j(t)$, which again is a good consistency check.

Table 5.13. Explained variance (R^2) by the fit in Eq. (5.2) for PIES sites N05 and N07 with $\Gamma_j(t) = 0$. The column labelled "None" lists R^2 with seasonal variation and $h_j(t)$, but no $x_j(t)$, ($a_{x,j} = 0$). The remaining columns list R^2 with the full Eq. (5.2) and for various choices of altimetry parameter x_j. Both $h_j(t)$ and $x_j(t)$ have been de-seasoned before fitting. The bold underlined values represent the parameters chosen for further analysis.

x_j:	None	U_1	U_2	U_3	U_4	U_5	U_6	U_7	PcAH-1	PcAH-2	PcAH-3	PcAU-1	PcAU-2	PcAU-3
N05:	0.727	0.754	0.790	**0.817**	0.731	0.762	0.776	0.732	0.814	0.732	0.812	0.761	0.785	0.726
N07:	0.708	0.709	0.708	0.713	0.708	0.710	0.724	**0.814**	0.719	0.709	0.714	0.716	0.709	0.782

The bold underlined choices in Table 5.13 are those with the highest R^2 values and they have been selected for further analysis. The coefficients to use in Eq. (5.2) for these choices, as determined by multiple linear regression, are listed in Table 5.14, which also documents the performances of the fits for both stations.

Table 5.14. The left part of the table lists the choices for parameter $x_j(t)$ and the coefficients to use in Eq. (5.2) with $\Gamma_j(t) = 0$ for N05 and N07 based on the PIES data. Both $x_j(t)$ and $x_j(t)$ are 28-day averages that have been de-trended and de-seasoned. The last five columns indicate the performance of the fit: "R^2" is the variance explained by the fit. "std", "max", "min", and "avg" are the standard deviation, maximum, minimum, and average of the difference (observed – fitted), respectively.

	$x_j(t)$	$a_{h,j}$	$a_{x,j}$	$a_{0,j}$	A_j	Day_j	R^2	std	max	min	avg
	cm/s	m/cm	m/(cm/s)	m	m	number		m	m	m	m
N05:	U_3	5.23	-5.87	323	40	277	0.82	24	32	-59	0
N07:	U_7	5.29	6.91	231	35	250	0.81	23	33	-45	0

From the performance indicators in the last five columns of Table 5.14, the fitted isotherm depths compare remarkably well with the observed depths with standard deviations (std) of the difference between fitted and observed less than 25 m for both N05 and N07. The largest deviations are seen in the column labelled "min" in the table, which means that they represent occasions where the fitted depths exceed the observed depths. As seen in Figure 5.13, this seems to occur mainly when the isotherms are shallow, which was also seen for the isotherm depths based on CTD data (Figure 5.12).

Figure 5.13. The red squares show comparisons between 28-day averaged depths of the 4°C-isotherm for stations N05 and N07 as observed by the PIES and as fitted by Eq. (5.2) using the parameter choices and coefficients listed in Table 5.14. The red diagonal lines indicate equality.

By requiring $\Gamma_j(t)$ to be zero in this analysis, we have, however, disregarded all the information from the CTD data and it remains to clarify, how consistent the two data sets (CTD and PIES) are. The only terms in Eq. (5.2) that have longer time scales than the seasonal are $\Gamma_j(t)$ and $a_{0,j}$. If we had used the correct value for $\Gamma_j(t)$, we would expect the constant term, $a_{0,j}$, to be zero. When instead we have required $\Gamma_j(t)$ to be zero, the value of $a_{0,j}$ should represent $\Gamma_j(t)$ for the PIES period.

We therefore compare the values of $a_{0,j}$ in Table 5.14 with the two alternative versions for $\Gamma_j(t)$. The 3-year running mean depth of the 4°C-isotherm (Figure 5.11) for the middle year of the PIES period, 2018, was 344 m at N05 and 255 m at N07, i.e., more than 20 m higher than the respective values for $a_{0,j}$ in Table 5.14 for both stations, If, instead, we use Eq. (5.3) to estimate $\Gamma_j(t)$ for the middle of the PIES period, we get 326 m at N05 and 237 m at N07, both of which deviate less than 10 m from the values for $a_{0,j}$.

With these encouraging results, it is a bit depressing to note that the coefficients in Table 5.14 (based on PIES data) deviate considerably from the coefficients in Table 5.9 (based on CTD data) for the same choices for $x_j(t)$ both N05 and N07. This apparent disagreement may be misleading, however, as

demonstrated by Table 5.15. There, we have used the coefficients from the last three columns of Table 5.9 instead of Table 5.14. Thus the values in Table 5.15 represent a comparison between the 28-day averaged isotherm depths from the PIES and fits using 28-day averaged altimetry data in Eq. (5.2) with coefficients derived from the CTD data.

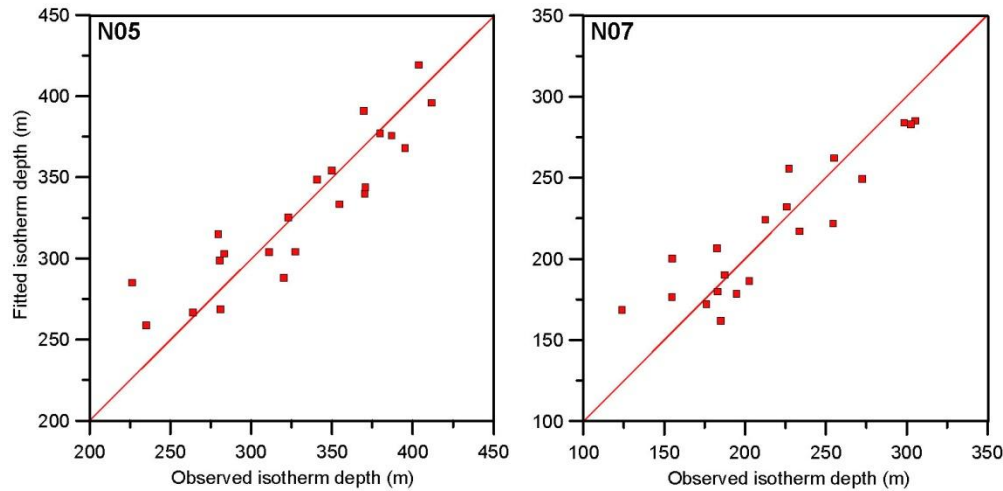**Table 5.15.** The correspondence between 28-day averaged depths of the 4°C-isotherm for stations N05 and N07 as observed by the PIES and as fitted by Eq. (5.2) using the parameter choices and coefficients listed in Table 5.9 with $\Gamma_j(t)$ given by Eq. (5.3) (last three columns in Table 5.9). "R^2" is the variance explained by the fit. "std", "max", "min", and "avg" are the standard deviation, maximum, minimum, and average of the difference (observed – fitted), respectively.

	N05					N07				
$x_j(t)$	R^2	std	max	min	avg	$x_j(t)$	R^2	std	max	min	avg
U_5:	0.71	32m	45m	-54m	-10m	PcAH-1:	0.79	24m	43m	-59m	-2m
PcAH-1:	0.77	29m	60m	-42m	1m	U_6:	0.73	28m	46m	-54m	-3m
U_3	0.73	29m	64m	-63m	4m	U_7:	0.84^2	22m	55m	-33m	1m

The values for explained variance (R^2) in Table 5.15 are seen to be much higher than the R^2 values from using the same coefficients on the CTD data. This has an important implication:

- Even though the coefficients in Table 5.9 were derived from snapshot CTD profiles and daily averaged altimetry values, the fits using these coefficients are much less noisy than indicated by the R^2 values in Table 5.9 when used with 28-day averaged altimetry and $\Gamma_j(t)$ given by Eq. (5.3). Since this is the case for both N05 and N07, we expect it also to be valid for other stations, at least to some extent.

Before we can finally generate algorithms to simulate the depth of the 4°C-isotherm at N05 and N07, it remains to decide, which of the three choices in Table 5.15 to select for each station. One might be tempted to choose the one with the highest R^2 value, but in most cases, there is little difference and it might be a statistical fluke (e.g. the value 0.84 in Table 5.15 ?).

To facilitate the selection, 28-day averaged altimetry parameters were generated for the whole altimetry period (343 values) and used to simulate 28-day averaged isotherm depth for three different choices for $x_j(t)$ for each station (Table 5.15). Comparisons between these indicate very similar averages and standard deviations (Table 5.16a).

Table 5.16a. Statistics of the 4°C-isotherm depth at N05 and N07 for the whole altimetry period as simulated by Eq. (5.2) with 28-day averaged altimetry parameters with different choices for the parameter $x_j(t)$. The coefficients are from Table 5.9 with $\Gamma_j(t)$ given by Eq. (5.3)

Station:	N05			N07		
Parameter $x_j(t)$:	U_5	U_3	PcAH-1	U_6	U_7	PcAH-1
Average (m):	289	291	287	197	200	202
Stand. dev. (m):	65	69	66	77	78	78
Minimum (m):	85	65	97	0	0	0
Maximum (m):	476	490	482	385	402	405

A further comparison was made by correlating the simulated isotherm depth time series generated from different choices of the $x_j(t)$ parameter with one another (Table 5.16b). For N05, the series based on PcAH-1 is better correlated with the series based on both U_5 and U_3 than these two series are with one

---

[2] It may seem paradoxical that a fit based on Table 5.9 should fit the observed values better (higher R^2 value) than the fit that was generated from the observed values (Table 5.14). Note, however, the difference in seasonal amplitude (Table 5.7 and Table 5.11).

another. We therefore choose the series based on PcAH-1 for station N05. For N07, all the series are well correlated.

Table 5.16b. Correlation coefficients between 28-day averaged 4°C-isotherm depth as simulated by Eq. (5.2) with two different choices for the parameter $x_j(t)$ for the same station. The data are for the whole altimetry period and the coefficients are from Table 5.9 with $\Gamma_j(t)$ given by Eq. (5.3)

Station:	N05			N07		
$x_j(t)$ pair:	$\overline{U_5}-U_3$	U_5-PcAH-1	U_3-PcAH-1	$\overline{U_6}-U_7$	U_6-PcAH-1	U_7-PcAH-1
Corr. coeff.:	0.896***	0.973***	0.944***	0.980***	0.974***	0.985***

A similar exercise may be tried for stations N06 and N08. They each have two choices for $x_j(t)$ in Table 5.9, one of which is PcAH-1 and the other a surface velocity parameter. Also for these cases, average values and standard deviations are very similar and the correlation coefficient between the two series is 0.981*** for both N06 and N08. Thus, there is no clear guideline for which parameter to select for $x_j(t)$.

We have decided to use PcAH-1 for all the four stations N05 to N08. With this decision, the isotherm depth at each of these stations is based on Eq. (5.2) and Eq. (5.3) with one local altimetry parameter, $h_j(t)$, and one parameter, PcAH-1, which is determined from the altimetry along the whole section. The performances of these fits on monthly time scales may be illustrated for stations N05 and N07 by comparing the fitted 28-day averaged isotherm depths with those observed by the PIES (Figure 5.14).
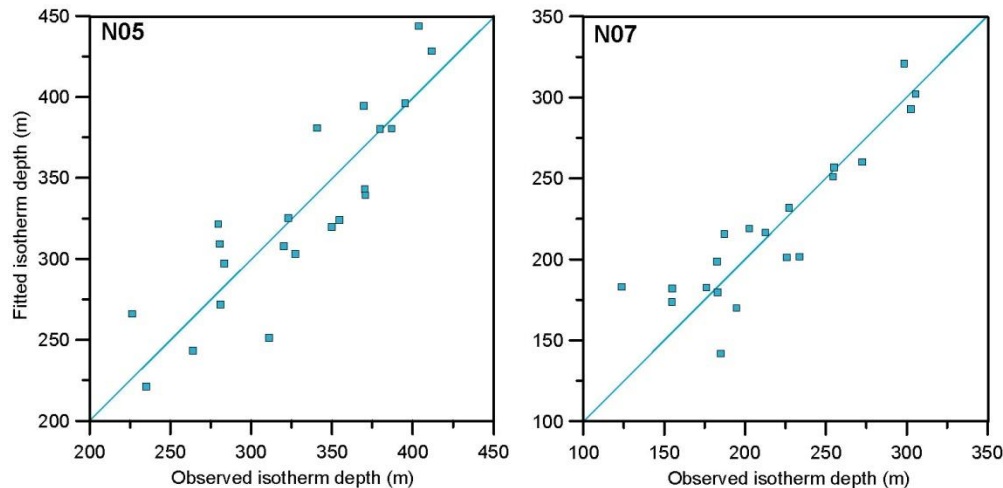
Figure 5.14. The cyan squares show comparisons between 28-day averaged depths of the 4°C-isotherm for stations N05 and N07 as observed by the PIES and as fitted by Eq. (5.2) and Eq. (5.3) with $x_j(t)$ = PcAH-1 and coefficients listed in Table 5.17. The cyan diagonal lines indicate equality.

5.5 Overview of isotherm depth determination for stations N05 to N10

5.5.1 Isotherm depth simulation from altimetry data alone

For station N04, no fit based on altimetry data alone was very successful and this station will be further addressed in Chapter 6. For the other deep stations in the Atlantic domain, Eq. (5.2) with Eq. (5.3) can be used to simulate the 4°C-isotherm depth, using altimetry data alone, with some accuracy. For stations N05 to N08, the use of PcAH-1 for the parameter $x_j(t)$ can explain between 58 and 66% of the variance in isotherm depth observed by CTD (Table 5.17). As discussed in the previous section, monthly averaged isotherm depth is likely to be considerably better simulated. For stations N09 and N10, the inclusion of

$x_j(t)$ in the simulation did not give appreciably better fits, and we set $a_{x,j}$ to zero for these stations (Table 5.17).

Table 5.17. Coefficients to use with Eq. (5.2) and Eq. (5.3) to simulate 4°C-isotherm depth at stations N05 to N10 with $x_j(t) =$ PcAH-1 and explained variance (R^2) of the isotherm depths from CTD.

Coeff.:	$d_{0,j}$	Y_j	$a_{TA,j}$	A_j	Day_j	$a_{h,j}$	$a_{x,j}$	$a_{0,j}$	R^2
Unit:	m	m/yr	m/°C	m			m	m	
N05:	271	2.33	30.6	32	294	3178	-151.38	-14	0.62
N06:	214	3.20	44.0	45	283	2511	-135.41	-9	0.58
N07:	163	3.16	45.1	65	262	2011	-94.09	-2	0.66
N08:	115	3.12	30.4	56	269	1762	-63.33	-2	0.63
N09:	57	3.00	0.0	48	262	872	0.00	0	0.56
N10:	47	1.21	0.0	48	270	437	0.00	0	0.54

5.5.2 Isotherm depth from PIES

Isotherm depths determined from calibrated PIES data are considered the most accurate source for continuous data and will be used in preference to the simulated isotherm depths whenever available. In the present data set, isotherm depths from PIES are only available for stations N05 and N07 from the 2017-2019 experiment, but they may also be used to determine the isotherm depth at the intermediate station N06. It was noted by Hansen et al. (2019b) that the observed 4°C-isotherm depth at N06, D_{N06}, was highly correlated (R = 0.86***) with the average of the isotherms depth at N05, D_{N05}, and at N07, D_{N07}. A slightly better estimate may be acquired by multiple linear regression on data from 109 CTD cruises for which isotherm depths were measured at all the three stations within less than 9 hours:

$$D_{N06} = 0.408 \cdot D_{N05} + 0.669 \cdot D_{N07} - 9 \text{ m} \qquad (5.4)$$

This relationship explains 77% of the variance in D_{N06}, which is much higher than the 58% in Table 5.17. When D_{N05} and D_{N07} are available from PIES, this relationship will therefore be used to derive D_{N06} instead of Eq. (5.2). A similar attempt to relate the isotherm depth at N08, D_{N08}, to D_{N05} and D_{N07} explained less of the variance of D_{N08} than Eq. (5.2) and has not been implemented.

6 Estimating isotherm depth at station N04

As discussed in Chapter 5, the monthly averaged isotherm depth for stations N05, N06, N07, and N08 may be estimated with a high accuracy from satellite altimetry alone. This leaves the northernmost part of the section, which will be discussed in Chapter 7, and station N04, discussed here, for which altimetry only explains around 30% of the variance in isotherm depth (Table 5.9). There are, however, additional observations that may be used for station N04.

6.1 The bottom temperature at site NE

6.1.1 The bottom temperature data at NE

Site NE is located a few km south of station N04 with a bottom depth ($\approx$ 455 m) close to the average depth of the 4°C-isotherm in this region. Thus, the bottom temperature at NE might well be related to the depth of the isotherm at N04.

Initially, the bottom temperature data at this site were collected by an ADCP in a protective frame, moored at NE during several periods from July 2000 to May 2011. The ADCP measured the temperature every 20 minutes. The accuracy is not high, but sufficient for the purpose here. In October 2014, a specially designed bottom temperature logger in a protective frame (Figure 6.1a) was deployed at NE. The logger measured temperature (high accuracy) every hour and data were to be uploaded acoustically to research vessel and three successful uploads were obtained, the last one in September 2015. Since then, several attempts to contact the logger have failed and it is considered lost.
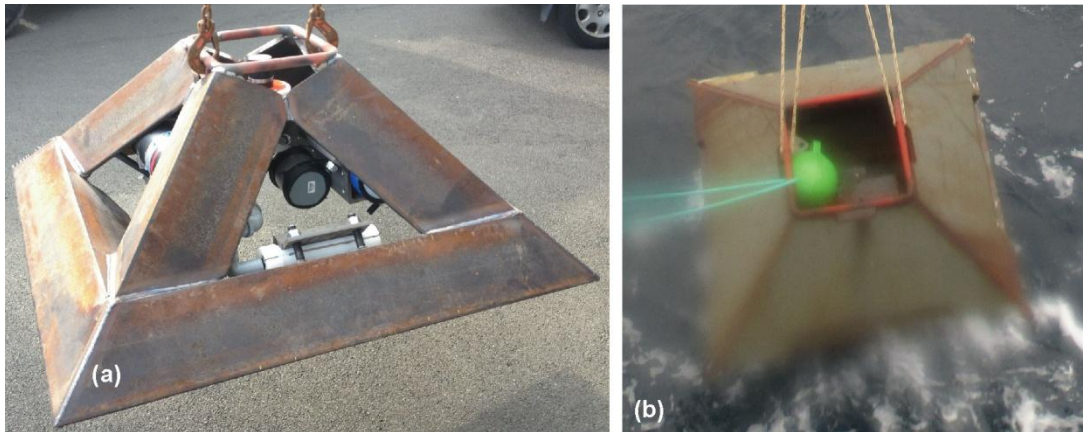
Figure 6.1. Two different types of instrument packages developed by Havstovan to monitor bottom temperature in heavily fished areas, both of them with instrumentation continuously logging temperature inside protective frames. Data recovery either with acoustic upload to research vessel **(a)** or with timed release of up to four self-contained LoTUS buoys (green in photo) that transmit data after surfacing **(b)**.

In 2017, a different type of bottom temperature logger (Figure 6.1b) was deployed at NE. This type has a protective steel frame within which there may be up to four self-contained LoTUS buoys. Each of these buoys measures temperature every hour and is pre-programmed to release its connection to the frame, surface, and transmit data at a specific time. The first of these frames was deployed in October 2017 with only one LoTUS buoy in the frame. This buoy was planned to surface and transmit in June 2018, but no data were received from it. In the meantime, a new frame with four buoys was deployed in May 2018. The first of these four buoys was programmed to surface in June 2019, but again with no data received. The three remaining buoys in this frame are programmed to surface in June 2020, 2021, and

2022, respectively. Each of the buoys stores temperature data for the whole period from deployment to release, so there is still hope of complete data recovery from this later deployment.

At the present stage, bottom temperature data from site NE are thus only from the ADCP deployments, a total of 3635 days, and 220 days from the first type of bottom temperature logger (Figure 6.1a). Of these 3855 days, around one third (32%) had daily averaged bottom temperatures above 4°C (Figure 6.2a), and the overall average was 3.15°C. Typically, the 4°C-isotherm thus seems to hit bottom shallower than at site NE.

From Table 2.2, the isotherm deepens $\approx$ 100 m from N05 to N04. Since site NE is located some 4-5 km south of station N04, the extrapolated isotherm depth at site NE would be $\approx$ 440 m. From Table 2.5, a depth difference of 15 m (455 – 440) would be equivalent to around 0.5°C, a bit less than the 0.85°C indicated by the average temperature. This might indicate that the 4°C-isotherm deepens less steeply from N04 to NE than from N05 to N04, but taking all the uncertainties in Table 2.2 and Table 2.5 into account, the overall picture is one of consistency.
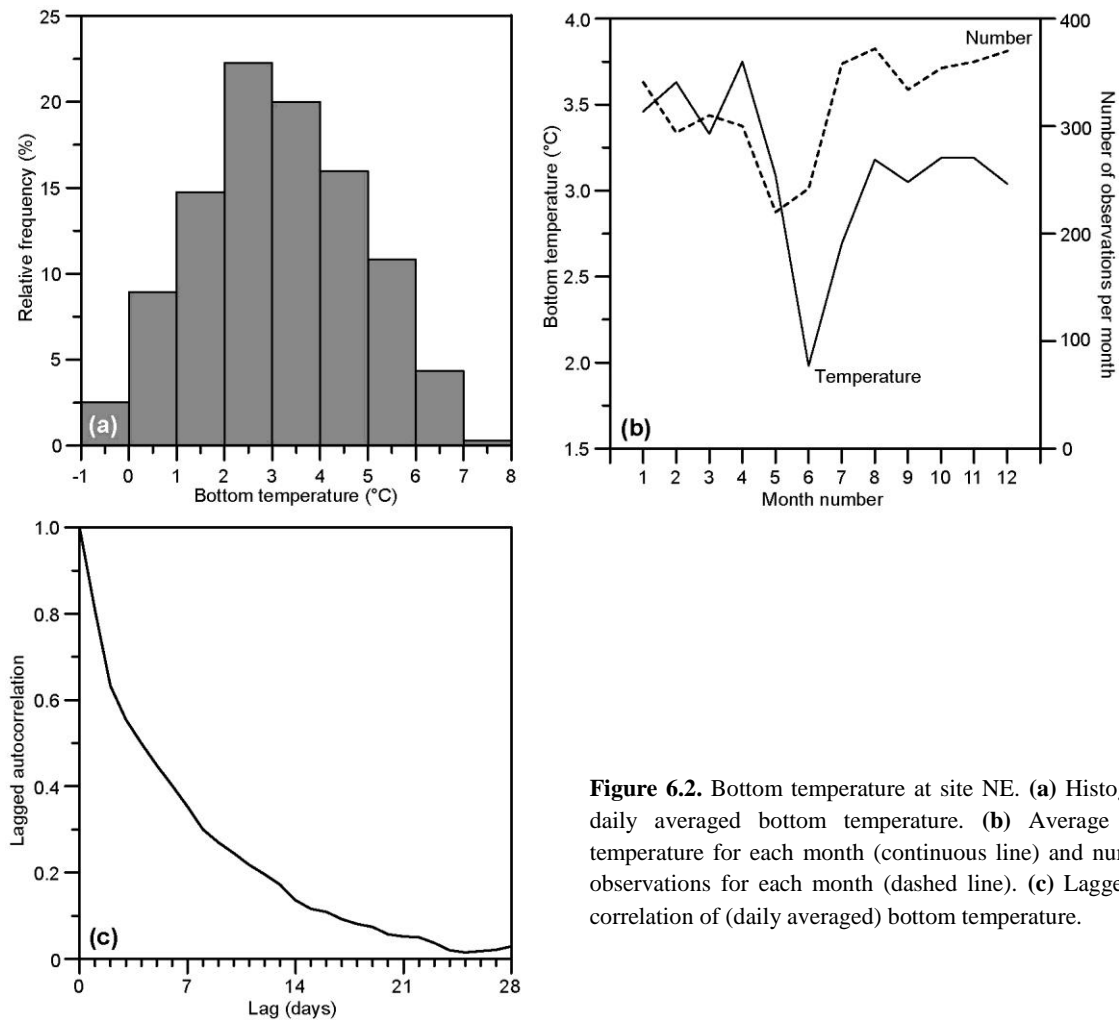
Figure 6.2. Bottom temperature at site NE. **(a)** Histogram of daily averaged bottom temperature. **(b)** Average bottom temperature for each month (continuous line) and number of observations for each month (dashed line). **(c)** Lagged auto-correlation of (daily averaged) bottom temperature.

A histogram of daily averaged bottom temperature at NE (Figure 6.2a) shows a wide range of temperatures, consistent with the wide range of isotherm depth variations at station N04 (Table C3). From Figure 6.2b, there appears to be a seasonal variation with minimum bottom temperature (i.e., shallowest

isotherm) in June. Table 2.2 indicates the shallowest isotherm depth at N04 to be in April, but the seasonal sinusoidal fit for N04 was not very good (R_{Max} only 0.23). From Figure 6.2c, the autocorrelation decreases rapidly with the lag, but still retains a value of 0.35 for a lag of a week.

6.1.2 Determining isotherm depth at N04 from bottom temperature at NE

We now want to use the bottom temperature at NE, $T_{NE}(t)$, to simulate the depth of the 4°C-isotherm at station N04, $D_4(t)$, for the period with temperature data at NE and will try an expression similar to Eq. (5.2) with Eq. (5.3). From Table 5.7, it appears that there is not a well defined dependence of isotherm depth on the Atlantic water temperature and we therefore use a fit of the form:

$$D_4(t) = d_{0,4} + \gamma_4 \cdot t + A_4 \cdot cos\left[2\pi \cdot \left(t - \frac{Day_4}{365}\right)\right] + a_{NE} \cdot T_{NE}(t) + b_{x,4} \cdot x(t) \qquad (6.1)$$

with γ_4, A_4, and Day_4 as listed in Table 5.7 and $x(t)$ as a parameter based on the altimetry data. For each choice of this parameter, the three coefficients, $d_{0,4}$, a_{NE}, and $b_{x,4}$, are determined by regression analysis on the de-trended and de-seasoned values of $D_4(t)$, i.e., on the $D_4(t)$ values observed (by CTD) minus the second and third terms on the right hand side of Eq. (6.1). Altogether, there were 47 CTD cruises in the periods with bottom temperature data at NE, from which values of $D_4(t)$ are available. The performance of each fit may be evaluated by the explained variance (R^2) as listed in Table 6.1, which includes the closest sea level (h_3 and h_4) and surface velocity (U_3) parameters as well as the six principal components.

Table 6.1. Explained variance (R^2) by the fit in Eq. (6.1) for selected altimetry parameters, $x(t)$. The column labelled "None" lists R^2 with trend, seasonal variation and $T_{NE}(t)$, but no $x(t)$, ($b_{x,4} = 0$). The remaining columns list R^2 with the full Eq. (6.1) and for various choices of altimetry parameter x, which have been de-trended and de-seasoned before fitting. The bold underlined value represents the parameter chosen for simulating $D_4(t)$.

x:	None	h_3	h_4	U_3	PcAH-1	PcAH-2	PcAH-3	PcAU-1	PcAU-2	PcAU-3
	0.554	0.570	0.635	**0.659**	0.572	0.557	0.664	0.583	0.652	0.573

As seen in the first column of Table 6.1, the bottom temperature at NE by itself explains 55% of the variance of $D_4(t)$, and several additional choices for the parameter $x(t)$ increase the explained variance to more than 60%. The highest value for R^2 is for PcAH-3, but this EOF mode only explained 3.5% of the sea level variance (Table 5.2). Instead, we choose the parameter $U_3(t)$ to use for $x(t)$ in Eq. (6.1) and Table 6.2 lists the values for the coefficients as well as two different error indicators for the fit. As seen in Figure 6.3, the fitted depth deviates most from the observed depth when the isotherm (as observed by the CTD) is shallow consistent with previous results (e.g., Figure 5.12).

Table 6.2. Coefficients to use with Eq. (6.1) to simulate 4°C-isotherm depth at station N04 with $x(t) = U_3(t)$ as well as the Root-Mean-Square (RMS) and maximal (Max) errors of the fit.

Coeff.:	$d_{0,4}$	γ_4	A_4	Day_4	a_{NE}	$b_{x,4}$	RMS	Max
Unit:	m	m/yr	m		m/°C	s	m	m
N04:	259	1.97	25	298	32.1	−323	36	101

This parameter choice is the same as that by Hansen et al. (2015) (their Table S4.2.1) and the coefficients have similar values when taking into account the differences in definitions and units. The new coefficients are not identical to the old ones even though the data sets are the same. Also the explained variance for

the new fit (65%) is considerably higher than for the old (58%). The reason for these differences is that the fit in Hansen et al. (2015) did not include the linear trend and seasonal variation of Eq. (6.1).
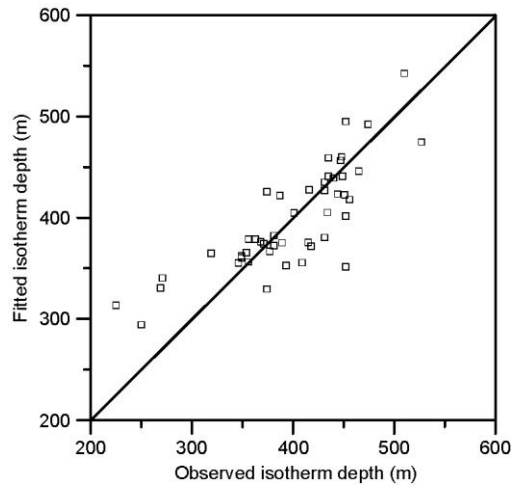
Figure 6.3. Depths of the 4°C-isotherm at station N04 simulated by Eq. (6.1) using the coefficients in Table 6.2 plotted against the observed isotherm depth.

6.2 The velocity profile at site NB

6.2.1 Determining isotherm depth at N04 from the velocity profile at NB

As discussed in Sect. 4.2.3, the thermal wind equation provides a relationship between the change in the 4°C-isotherm depth from N05 to N04 (D_{N04} - D_{N05}) and the vertical shear of the eastward velocity, Eq. (4.5). For CTD cruises where the isotherm depth had been observed at both N04 and N05, while there was an ADCP at NB (85 cases), this relationship could explain 62% (0.79^2) of the variance in (D_{N04} - D_{N05}) (Figure 4.12a) and two regression equations were suggested: Eq. (4.6) and Eq. (4.7).

The performances of these two fits were illustrated in Figure 4.13 and are summarized in the top row of Table 6.3. In order to use these fits to simulate the 4°C-isotherm depth at N04, we need to know the isotherm depth at N05, which from observations is only for 85 days. Using Eq. (5.2) and Eq. (5.3), we can, however, simulate the isotherm depth at N05 and then use the two fits. As seen in the two bottommost rows in Table 6.3, the performances of the fits with simulated D_{N05} is worse than with observed D_{N05}, but still relatively good. On the 85 CTD cruises, there were at most 5 hours difference between the observations at N04 and N05, but they were not always on the same day, which makes a small (probably not significant) difference (two bottommost rows in Table 6.3 and Figure 6.4).

Table 6.3. Comparison between observed depth of the 4°C-isotherm at station N04 and isotherm depth generated from Eq. (4.6) and Eq. (4.7) using the coefficients in Table 4.6 with D_{N05} as observed (top row), and as simulated by Eq. (5.2) and Eq. (5.3) with coefficients in Table 5.17 for the date of the isotherm observation at N05 (middle row) and the date of the isotherm observation at N04 (bottom row). "R" indicates correlation coefficient. "RMS" indicates Root-Mean-Square (RMS) error. "Max" indicates the maximal (numerical) error.

	Eq. (4.6)			Eq. (4.7)		
	R	RMS	Max	R	RMS	Max
D_{N05} observed:	0.81***	42m	119m	0.77***	43m	174m
D_{N05} simulated for the date at N05:	0.70***	54m	144m	0.66***	53m	161m
D_{N05} simulated for the date at N04:	0.71***	53m	144m	0.67***	52m	161m
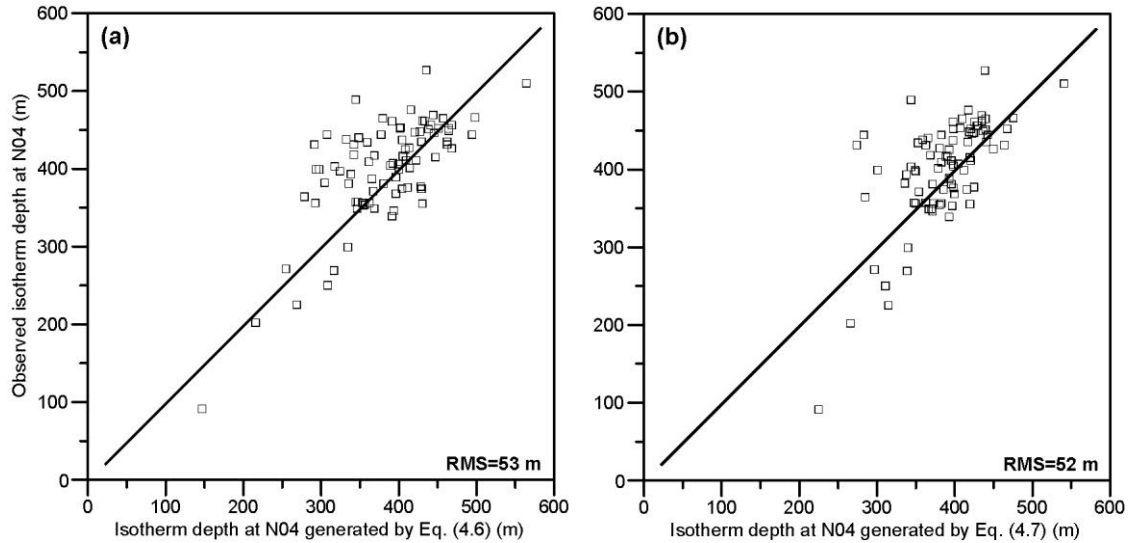
Figure 6.4. Observed depth of the 4°C-isotherm at station N04 plotted against the isotherm depth generated from Eq. (4.6) **(a)** and Eq. (4.7) **(b)** using the coefficients in Table 4.6 and using, not the observed D_{N05}, but rather D_{N05} as simulated by Eq. (5.2) and Eq. (5.3) with coefficients in Table 5.17 for the date of the isotherm observation at N04.

From Table 6.3, the best result is obtained by using the fit in Eq. (4.6) with D_{N05} simulated for the day of the observation at N04 (Figure 6.4a). This fit explains 50% of the variance of the D_{N04} as observed by CTD. This explanatory power is based on daily averaged altimetry and ADCP data. In analogy with the results from Sect. 5.4.3, we might perhaps expect the explanatory power to increase when averaging over longer periods. This is hard to verify directly, since we only have the snapshot estimates of isotherm depth at N04 obtained by CTD profiles. Indirectly, it can be verified, however, by correlating simulated values for D_{N04} with the bottom temperature at NE. For the fit in Eq. 4.6, the correlation coefficient increases from 0.51 to 0.58, when using 28-day instead of daily averages (Table 6.4) and Figure 6.5 illustrates the performances of the two fits for 28-day averages.
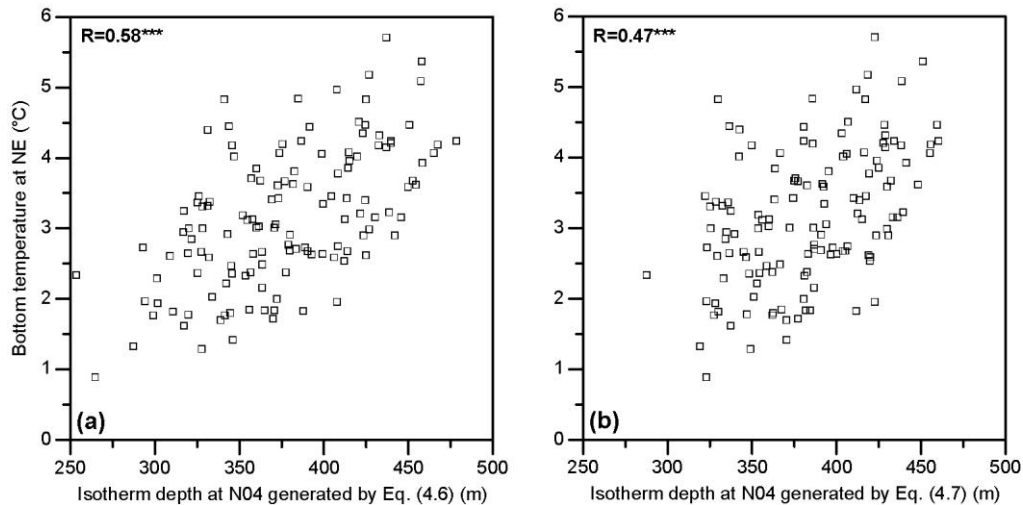
Figure 6.5. Monthly (28-day) averaged bottom temperature at site NE plotted against 28-day averaged isotherm depth generated from Eq. (4.6) **(a)** and Eq. (4.7) **(b)** using the coefficients in Table 4.6 and using D_{N05} as simulated by Eq. (5.2) and Eq. (5.3) with coefficients in Table 5.17 for the date of the isotherm observation at N04.

Table 6.4. Correlation coefficients between observed bottom temperature at site NE and 4°C-isotherm at station N04 generated from Eq. (4.6) and Eq. (4.7) with D_{N05} as simulated by Eq. (5.2) and Eq. (5.3) for daily and 28-day averages. "N" indicates number of values.

	Daily averages			28-day averages	
N	Eq. (4.6)	Eq. (4.7)	N	Eq. (4.6)	Eq. (4.7)
3769	0.51***	0.42***	130	0.58***	0.47***

6.3 Overview of isotherm simulation at station N04

Altogether, we have three different methods for simulating 4°C-isotherm depth at N04. They have different explanatory power, but they also have different needs for additional observational data sets and therefore different periods of applicability:

- **S1:** Simulation with altimetry data only, can be for every day in the altimetry period, i.e., from 1st January 1993 to 13th May 2019 (for the present altimetry data set).
- **S2:** Simulation with altimetry data and ADCP data from site NB can be done for days in the altimetry period with observations at NB.
- **S3:** Simulation with altimetry data and bottom temperature data from site NE can be done for days in the altimetry period with observations at NE.

Table 6.5. The 4°C-isotherm depth at N04, D_{N04}, simulated in three different ways. "Datacover" is the number of days for which data is available for the simulation. "N" is the number of D_{N04} observations (from CTD) in the simulated period, "R^2" is the explained variance, and "RMS" and "Max" the Root-Mean-Square and maximal error, respectively.

	Datacover	N	R^2	RMS	Max
S1:D_{N04} simulated with altimetry only:	9629 days	112	0.31	65m	284m
S2:D_{N04} simulated with altimetry and NB ADCP:	7603 days	85	0.50	53m	139m
S3:D_{N04} simulated with altimetry and NE temp:	3855 days	47	0.66	36m	100m

The characteristics of each of these simulation methods are summarized in Table 6.5, from which is evident that the simulation methods with highest data coverage have the lowest quality as indicated by R^2 and RMS- and maximal errors. These quality indicators are based on comparison between simulated isotherm depth and isotherm depth as observed by the snapshot CTD profiles. From the results in Sect. 5.4.3, we might perhaps expect the quality to be better when simulating monthly averaged isotherm depth. This is supported by Table 6.4 and also by Table 6.6 where the three simulation methods are compared. Correlation coefficients as well as both RMS- and maximal differences indicate much better correspondence between monthly than daily averaged simulations.

Table 6.6. Comparisons between the 4°C-isotherm depth at N04, D_{N04}, simulated in three different ways for overlapping periods. ""N" is the number of simulated values, "R" is the correlation coefficient, and "RMS" and "Max" the Root-Mean-Square and maximal difference, respectively. The "Monthly" values are for overlapping calendar (not 28-day) months.

	S1 versus S2				S1 versus S3				S2 versus S3			
	N	R	RMS	Max	N	R	RMS	Max	N	R	RMS	Max
Daily:	7603	0.71***	61m	319m	3855	0.63***	49m	186m	3769	0.62***	64m	269m
Monthly:	221	0.84***	35m	99m	115	0.70***	29m	63m	108	0.75***	33m	83m

The monthly values in Table 6.6 raise an important question. S2 is considerably better correlated with S3 than S1, but the RMS difference as well as the maximal difference is lower for (S1 versus S3) than for (S2 versus S3). So, does the use of the velocity at NB give better estimates of the 4°C-isotherm depth at

N04 than using altimetry data only? The problem is further illustrated in Figure 6.6, which compares isotherm depths at N04 determined by the three different methods for all calendar months (108 months) with observations at both NE and NB.
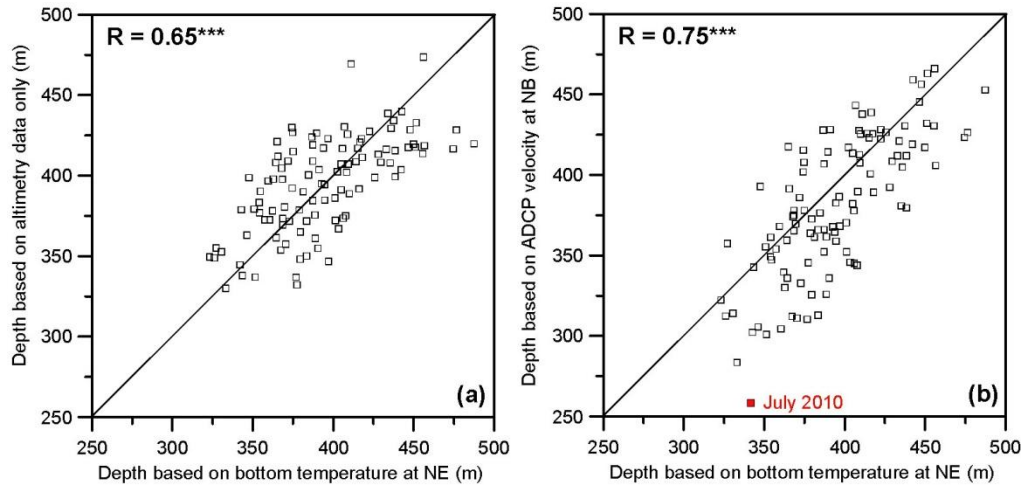
Figure 6.6. Comparisons between monthly averaged depth of the 4°C-isotherm at N04 determined in three different ways for all calendar months with at least 28 days of data at both NE and NB. The largest difference is highlighted in red.

The message from Figure 6.6 is the same as from Table 6.6. If we assume the isotherm depths based on the bottom temperature at NE to be our best estimate, then the depths based on the ADCP data at NB are better than those based on altimetry only, as long as we use the correlation coefficient as a criterion. If, however, we use the most extreme outlier (red square in Figure 6.6b), then the use of the ADCP data at NB may be worse than using altimetry only. We leave this question open here and return to it in Sect. 8.1, where we can estimate the effect on volume transport.

7 The Atlantic water boundary towards the North

Using the 4°C-isotherm as boundary for the Atlantic water extent on the section is seen as an appropriate definition for the deep stations in the southern part of the section where this isotherm is generally deep (Figure 2.1a). In the northern part of the section, on the other hand, the near-surface waters of Arctic origin are often heated above 4°C in summer and the 4°C-isotherm is not an appropriate boundary. Instead, Hansen et al. (2015) suggested to use the 35.0-isohaline and derived algorithms for simulating this isohaline from altimetry data. In the following, we first discuss this suggestion and a revised version of it and then update the algorithms.

7.1 Isohalines as Atlantic water boundary

7.1.1 Relations between Isotherm depth and salinity

If we compare the depths of the 4°C-isotherm and the 35.0-isohaline for all CTD profiles from each station where both isotherm and isohaline were within the water column (neither above nor below the CTD profile), we find that for the southernmost deep stations they are highly correlated (Figure 7.1). For stations N04 to N08, the correlation coefficient is above 0.9 and highly significant statistically ($p<0.001$).
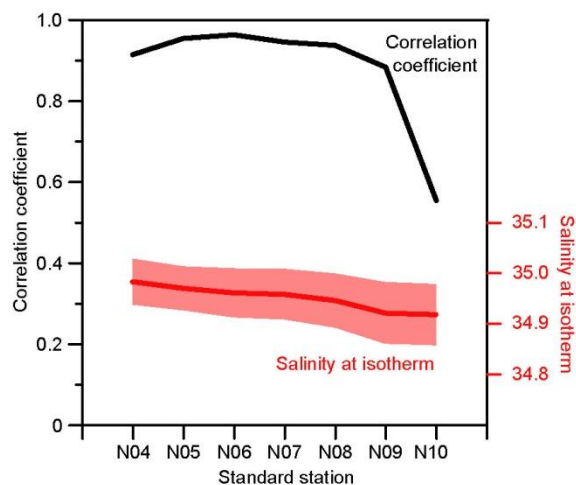
Figure 7.1. Correlation coefficient between depths of the 4°C-isotherm and the 35.0-isohaline, for which both are within the water column for stations N04 to N10 (black curve) and salinity at the 4°C-isotherm shown as average (thick red curve) ± one standard deviation (shaded red area) for all profiles where the isotherm was within the water column. Based on 80 CTD cruises 1997 – 2018.

At station N04, the average salinity at the 4°C-isotherm is seen to be close to 35.0 (34.98), but it decreases, as we move northwards. Most likely, this is because the Arctic water that is mixed with the Atlantic water decreases relatively more in salinity than in temperature as we move northwards. This raises the question, how appropriate it is to use the 35.0-isohaline as a northern boundary, which we address further in the next section.

7.1.2 Characteristics of the 35.0-isohaline in the upper water masses

The average salinity at each standard station is very similar at 10 m depth and at 100 m depth for stations N02 to N08 (Figure 7.2a), but diverges after that with considerably fresher water near the surface (at 10 m). On average, the salinity decreases below 35.0 around station N08 for both 10 m and 100 m depth. Consistent with that, the fraction of CTD profiles with salinity > 35.0 (i.e., Atlantic water) also falls below 50% around N08, although slightly more southerly at 100 m depth than at 10 m (Figure 7.2b).
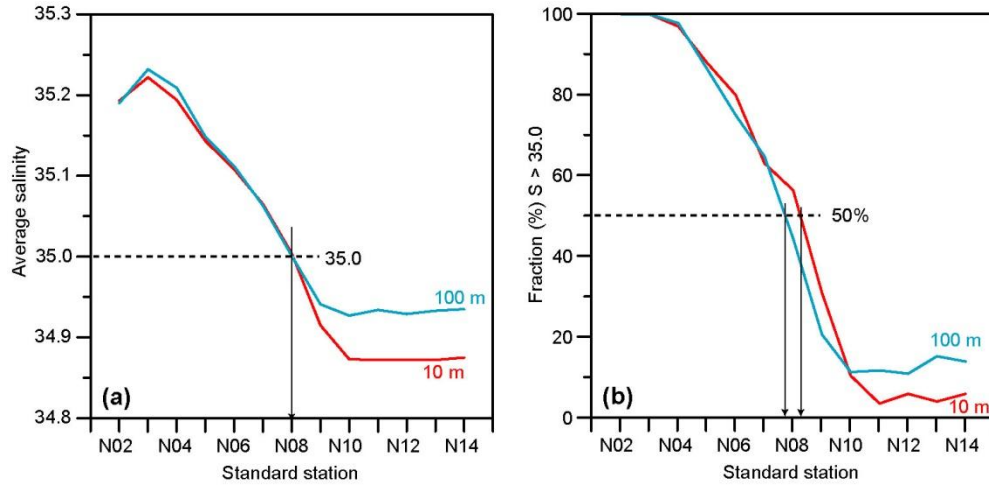
Figure 7.2. (a) Average salinity at 10 m depth (red) and 100 m depth (cyan) along the section. **(b)** Fraction of stations with salinity at 10 m (red) and 100 m (cyan) higher than 35.0. Observations have not always been at all stations on each cruise.
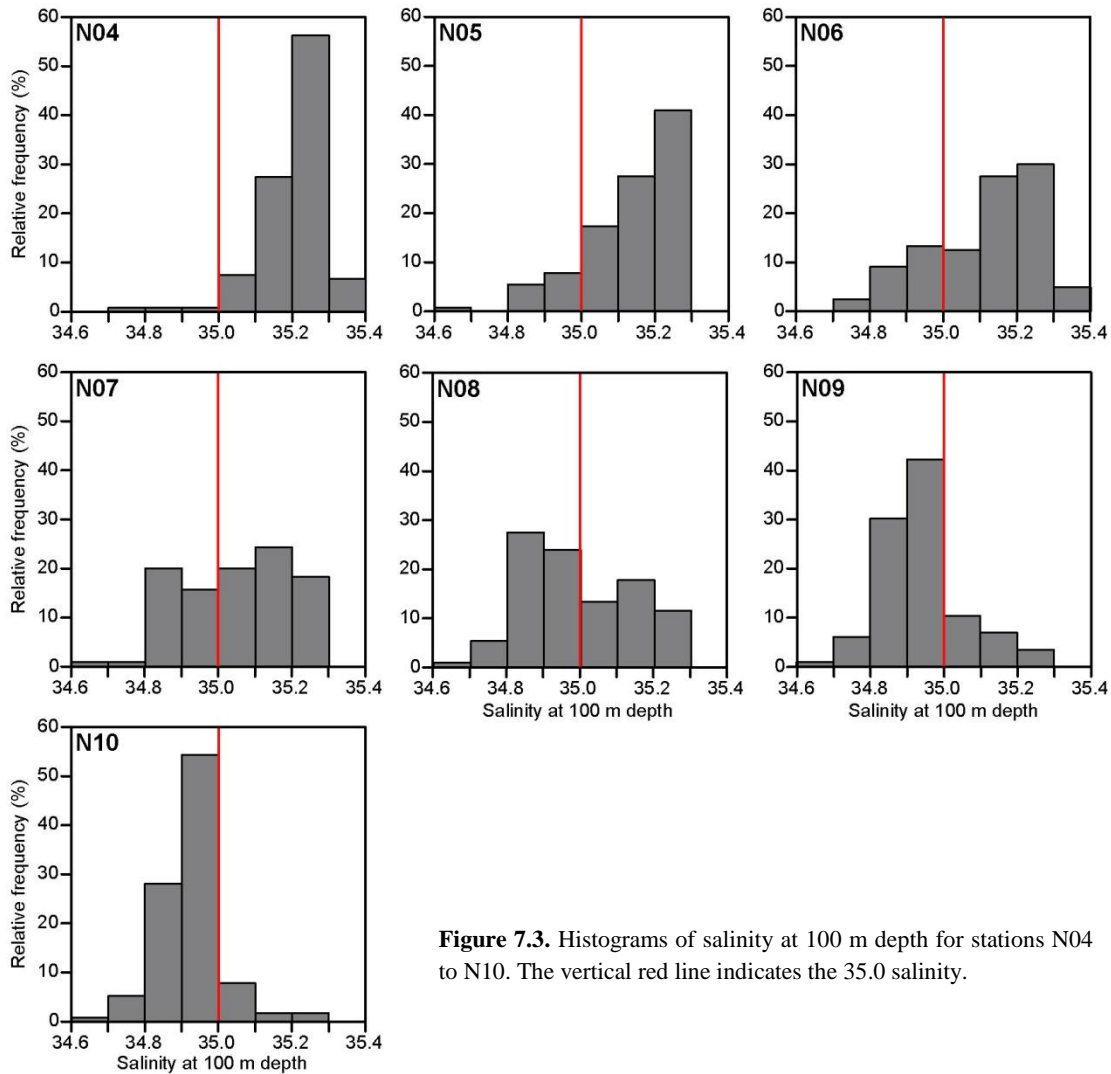
Figure 7.3. Histograms of salinity at 100 m depth for stations N04 to N10. The vertical red line indicates the 35.0 salinity.

A more detailed picture of the salinity variations at 100 m depth for the various stations is shown in Figure 7.3, which demonstrates that water with very low salinity (< 34.8) occasionally may be found even as far south as at N04 and N05. An example of this occurrence is seen in Figure 7.4a where the low-salinity water is in a thin layer near the surface. A salinity section for this cruise (Figure 7.4b) indicates that this is likely associated with a meso-scale feature passing through the section and that water with salinity > 35.0 extends all the way north of N09 at depths around 100 m.
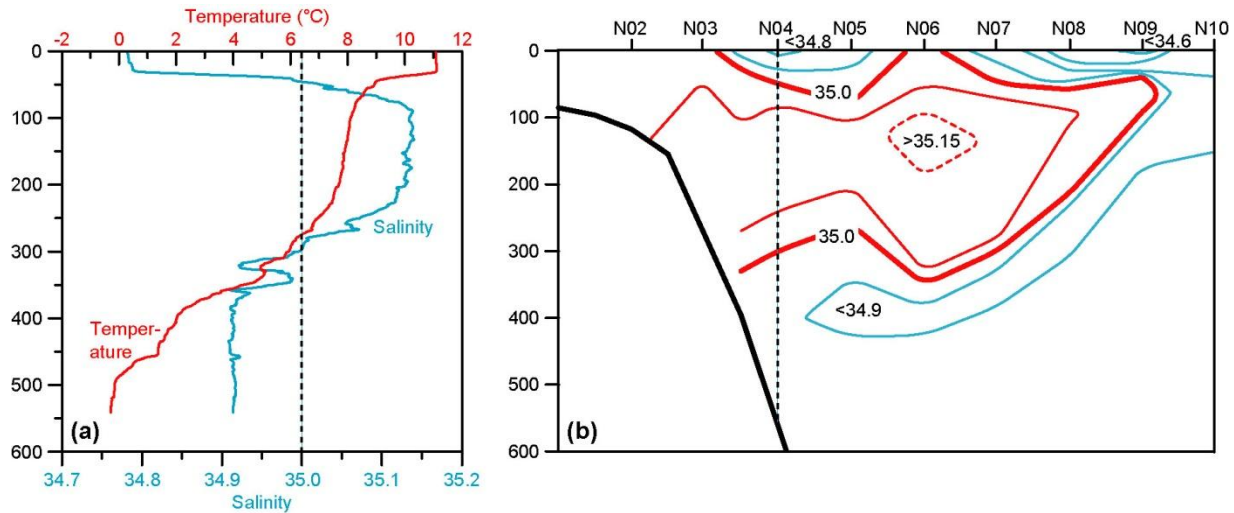
Figure 7.4. Hydrographic conditions on the monitoring section during R/V Magnus Heinason cruise 1838 in Agust 2018. **(a)** Salinity (and temperature) profile at station N04. Dashed vertical line indicates salinity 35.0. **(b)** Simplified salinity section (contouring interval 0.1). Dashed vertical line indicates station N04.

This was the reason for Hansen et al. (2015) to use the 35.0-isohaline at 100 m depth, rather than in the surface to define the northern Atlantic water boundary. Figure 7.3 shows, however, that even at 100 m depth, salinities below 35.0 are occasionally seen, but there may still be much more saline water farther north. Figure 7.4b also demonstrates the ambiguity involved in using the isohaline at a specific depth: choosing 50 m or 200 m instead of 100 m would give a large difference for the case shown in the figure.

7.1.3 Revised definition and simulation of the northern Atlantic water boundary

The preceding discussion illustrates the difficulty in using an isohaline at a specific depth to define the northern boundary, especially in the presence of meso-scale activity. Another problem is the long-term variation of Atlantic water salinity, which has varied by roughly 0.15 (between 35.15 and 35.30, Figure 2.2a). Is it reasonable to use a fixed isohaline under those conditions?

To address these problems, we use salinity data from a set of cruises with occupations of stations N04 to N10. To ensure high salinity quality, we only use data from 1997 onwards. There were altogether 80 such cruises where all seven of these stations were occupied within less than 24 hours. For each CTD profile, the maximum salinity between 20 m and 300 m depth was determined. For each cruise, there are thus seven maximum salinity values, which may be denoted $S_j(t)$ where j indicates station number ($j = 4$ to 10) and t is the time of the cruise.

To reduce the effects of the long-term salinity variation (Figure 2.2a), the maximum salinity values were then "normalized" based on a simplified mixing argument. Assume that the water at any given location may be seen as a mixture of just two water masses: Atlantic water with salinity $S_A(t)$ and low-

salinity water of Arctic origin with salinity $S_L(t)$. If the fraction of Atlantic water is denoted $r_j(t)$, then in this simple model:

$$S_j(t) = r_j(t) \cdot S_A(t) + \left[1 - r_j(t)\right] \cdot S_L(t) \qquad (7.1)$$

where we may use the values in Figure 2.2a for $S_A(t)$. The Arctic-origin waters in the upper layers in the northern part of the section have highly variable salinities, but persistent long-term variations are not as evident. We therefore use a typical value of 34.9 (constant in time) for S_L. With $S_A(t)$ and S_L given, the Atlantic water fraction associated with each maximum salinity value, $r_j(t)$, is easily determined. The "normalized maximum salinity" value, $S_j^*(t)$, is then determined by replacing the variable $S_A(t)$ with its temporal average $<S_A>$:

$$S_j^*(t) = r_j(t) \cdot \langle S_A \rangle + \left[1 - r_j(t)\right] \cdot S_L = \frac{[S_j(t) - S_L] \cdot \langle S_A \rangle + [S_A(t) - S_j(t)] \cdot S_L}{S_A(t) - S_L} \qquad (7.2)$$

Averaged over all the 80 cruises, the normalized maximum salinity decreases from 35.25 at N04 to 35.00 at N10. The maximum value for $S_j^*(t)$ does not vary much along the section, but the minimum value decreases rapidly from N04 to N07 (Figure 7.5a). The first three modes of an EOF analysis of the normalized salinity (Figure 7.5b) explained 82% of the variance (Table 7.1).

Table 7.1. Characteristics of the three dominant EOF modes of the normalized maximum salinity variation along the section listing explained variance (Expl.var.) and the seasonal variation of the principal components, as characterized by the maximum correlation coefficient (R_{Max}) of a sinusoidal seasonal variation, its amplitude (Ampl) and day number of maximum (Day_{Max}).

	Expl.var.	R_{Max}	Ampl	Day_{Max}
Mode 1:	0.45	0.47	0.72	27
Mode 2:	0.27	0.01	0.01	273
Mode 3:	0.10	0.11	0.15	104
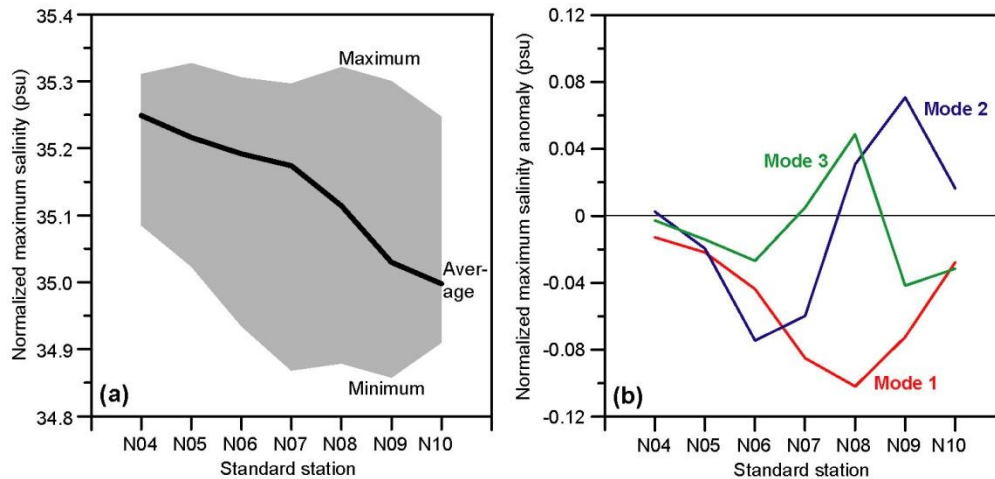
Figure 7.5. (a) Average normalized maximum salinity based on 80 cruises 1997-2018 with the interval between minimum and maximum values for each station shaded. **(b)** The three dominant EOF modes of the normalized maximum salinity in units of psu after the associated principal components have been normalized to a standard deviation of 1.

When the associated principal component is positive, Mode 1 involves a reduction of normalized maximum salinity all along the section, but most strongly around station N08 – so, a narrowing of the Atlantic water extent (Figure 7.5b). This mode seems to have a seasonal variation (although not very pronounced) with maximum values for the principal component in January (Table 7.1), which is consistent with previously observed focusing of the flow in the southern part of the section around this time (e.g., Figure S3.1.1 in the supplement to Hansen et a., 2015). The other two modes have opposite effects on different parts of the section with no apparent seasonal variation and are likely to include much of the meso-scale activity.

The principal component associated with Mode 1 was found to be significantly correlated with several altimetry parameters (Table 7.2). Again, we see that a high positive principal component value for this mode (PcS_1) is associated with increased eastward velocity in the southern part (U_4) and decreased in the northern part (U_7) as also implied by a high positive value for PcAU-1 associated with the first EOF mode (MAU-1) of the altimetric surface velocity (Figure 5.2b).

Table 7.2. Correlation coefficients between the principal components associated with normalized maximum salinity modes and altimetry parameters. "PcS_1" and "PcS_2" are the principal components associated with Mode 1 and Mode 2, respectively. Only correlation coefficients that were significant at the p<0.001 level are listed. None of the series have been de-seasoned or de-trended.

	h_5	h_6	h_7	h_8	U_4	U_5	U_6	U_7	PcAH-1	PcAH-2	PcAH-3	PcAU-1	PcAU-2
PcS_1:	-0.57	-0.68	-0.65	-0.56	0.69			-0.62	-0.54	0.50		0.63	
PcS_2:						-0.42	-0.52				0.53		-0.43

The principal component associated with Mode 2 was also found to be significantly correlated with some altimetry parameters, although to a lesser degree. Notably, this mode was significantly correlated with the "Eddy mode" of the altimetric surface velocity (PcAU-2). For Mode 3, no significant correlations were found.

On monthly time scales, meso-scale activity ought not to influence the Atlantic water extent to any large extent. This indicates that Mode 1 of the normalized maximum salinity may be the most appropriate measure of the Atlantic water extent and this is also the mode, which is best correlated with altimetry. By multiple regression analysis, it is found that a linear combination of altimetry parameters $h_6(t)$ and PcAH-1(t) can explain 58% of the variance of PcS_1. This expression can therefore be used to simulate PcS_1 and through that also the normalized maximum salinity for every day in the altimetry period:

$$S_j^*(t) \cong \langle S_j^* \rangle + \sum_{j=4}^{9} M_j^1 \cdot PcS_1(t)$$

$$\cong \langle S_j^* \rangle + \sum_{j=4}^{9} M_j^1 \cdot [-0.245 \cdot h_6(t) + 1.264 \cdot PcAH\text{-}1(t) + 1.04]$$

(7.3)

where $\langle S_j^* \rangle$ is the temporally averaged normalized maximum salinity for station j (Figure 7.5a) and M_j^1 is the value of Mode 1 for station j (Figure 7.5b). Using this expression to simulate monthly averaged $S_j^*(t)$ for the whole altimetry period, it is verified that the simulation gives values that appear close to normally distributed around the average values based on the 80 CTD cruises (thick black line in Figure 7.5a). From the structure of the mode (red curve in Figure 7.5b) and monthly averaging, we expect smaller ranges for the simulated values than were observed in the snapshot CTD cruises (Figure 7.5a), especially for the southernmost stations.

Closer to the typical Atlantic water boundary, the simulations still fail to reproduce as low values as observed, which is illustrated by an example in Figure 7.6. This was to be expected since the simulations include only the first mode; not the higher modes that would represent most of the meso-scale activity, Eq. (7.3). More problematic in Figure 7.6 is the occurrence of higher values than observed. These are only very few, but to exclude them, the simulations have been constrained to be within the ranges observed during the 80 CTD cruises (shaded area in Figure 7.5a).
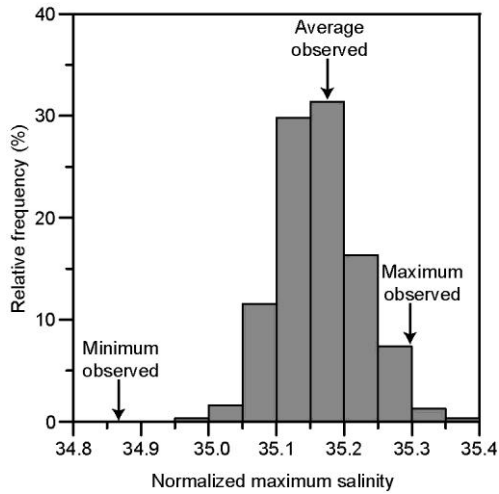
Figure 7.6. Histogram of simulated values for the monthly averaged normalized maximum salinity at station N07. The arrows indicate average, minimum, and maximum values for N07 observed during the 80 CTD cruises. The histogram shown is for the unconstrained simulations; before the constraint to be within the observed ranges was applied.

7.1.4 The choice of a reference salinity to define the northern Atlantic water boundary

With this tool, it is possible for every month in the altimetry period to determine where on the section, $S_j^*(t)$ crosses any give reference salinity, S_{Bound}, chosen to define the boundary. Figure 7.7, demonstrates the effect of two different choices for this reference value. The value $S_{Bound} = 35.075$ is midway between the average value for $S_4^*(t)$ at station N04 and the chosen value for Arctic water salinity $S_L = 34.9$ and so would represent an equal mixture of these waters, whereas $S_{Bound} = 35.0$ is the value used by Hansen et al. (2015), although for the actual (not normalized) salinity.
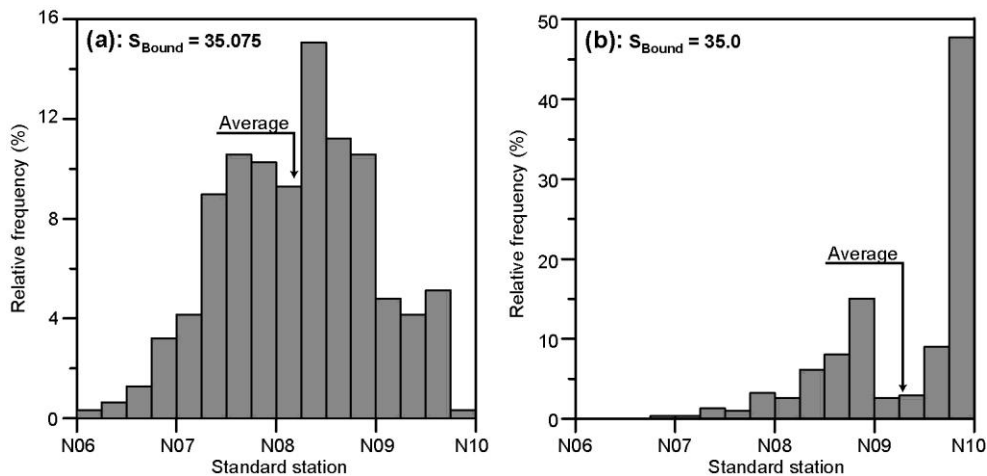
Figure 7.7. Histograms of the location of the northern Atlantic water boundary for two different choices of reference salinity, S_{Bound}, based on monthly averaged simulations for the period 1993 – 2018.

It is implicit in the method that the boundary never extends north of station N10, which helps explain the skewed distribution in Figure 7.7b. If we compare the averages for the two distributions in Figure 7.7 with the average salinity distribution in Figure 2.1 (lower panel), we find that the average in Figure 7.7a (S_{Bound} = 35.075) fits almost exactly with the surface location of the 35.0-isohaline in Figure 2.1, whereas the average in Figure 7.7b (S_{Bound} = 35.0) is much farther north. This seems counterintuitive, but it should be kept in mind that 1) Figure 7.7 is based on normalized salinities, whereas Figure 2.1 is not, and 2) Figure 7.7 is only based on the variations of the first EOF mode of normalized maximum salinity; not the higher modes that probably are the main cause of low-salinity water being advected into the Atlantic domain by meso-scale activity. This may also help explain why the salinity at the 4°C-isotherm (red curve in Figure 7.1) is so low compared to these values for S_{Bound}.

In the final end, the choice of a value for S_{Bound} to define the northern Atlantic water boundary is to a large extent arbitrary, as is the choice of the 4°C-isotherm to define the deep boundary. One might use more refined mixing models as was attempted by Hansen et al. (2003), but this would require much more knowledge on both mixing processes and the spatial and temporal variations of water mass characteristics than is available. As discussed in Hansen et al. (2003; 2015), the arbitrariness of these choices is a dominant contributor to the uncertainty of the temporally averaged transport values. The temporal transport variations should, however, be much less sensitive to the choices.

With this in mind, we choose the value S_{Bound} = 35.075. This seems to give a more realistic distribution of the northern Atlantic water boundary (Figure 7.7a) and this value is also midway between the average normalized maximum salinity of "pure Atlantic water" (N04) and "pure Arctic water" (S_L). Thus this definition is consistent with the use of the 4°C-isotherm (midway between 8°C and 0°C) for the deep boundary. With this definition, there is a clear seasonality to the location of the northern boundary (Figure 7.8).
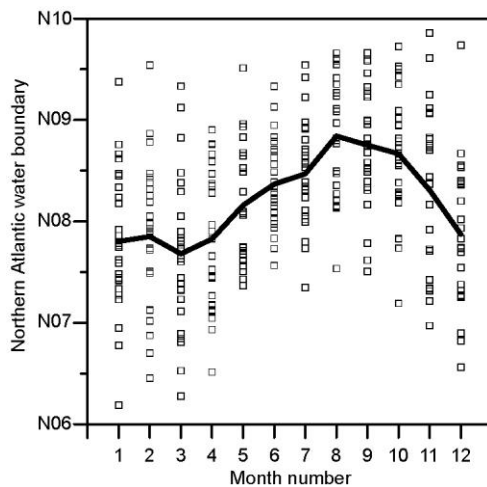
Figure 7.8. Seasonal variation of the monthly averaged simulated location of the northern boundary. Each square represents one month in the 1993 – 2018 period. The thick black curve is the overall monthly average.

7.2 Linking the deep boundary and the northern boundary

Having defined two different boundaries - one towards depth and one towards the north – the question arises how to connect them. Combining the seasonal variation of the northern boundary with the seasonal variation of the 4°C-isotherm depth from Table 5.7, we can sketch the typical situation in the boundary region in winter, summer, and on average (Figure 7.9).
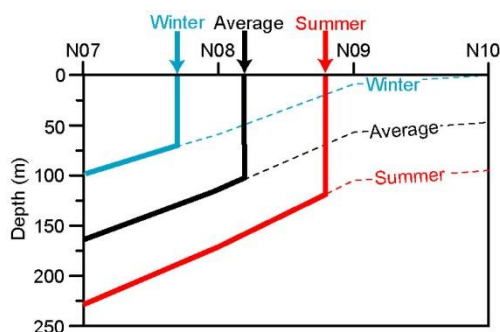
Figure 7.9. The typical situation in the boundary region in winter (around March, cyan), summer (September, red), and on average. The thin dashed lines show the average depths of the 4°C-isotherm in the three cases (From Table 5.7). The thick vertical arrows indicate the locations of the northern boundary (from Figure 7.8). The thick coloured lines indicate how the two types of boundary are connected.

Considering the seasonal variation of isotherm depth when the isotherm sometimes is not within the water column (surface colder than 4°C) is of course questionable. Thus, Figure 7.9 must not be interpreted too literally. The indicated relationship between the northern boundary and isotherm depth does seem to be more generally applicable (Figure 7.10). Figure 7.9 also illustrates how the two boundaries are connected more generally (Thick lines in the figure).
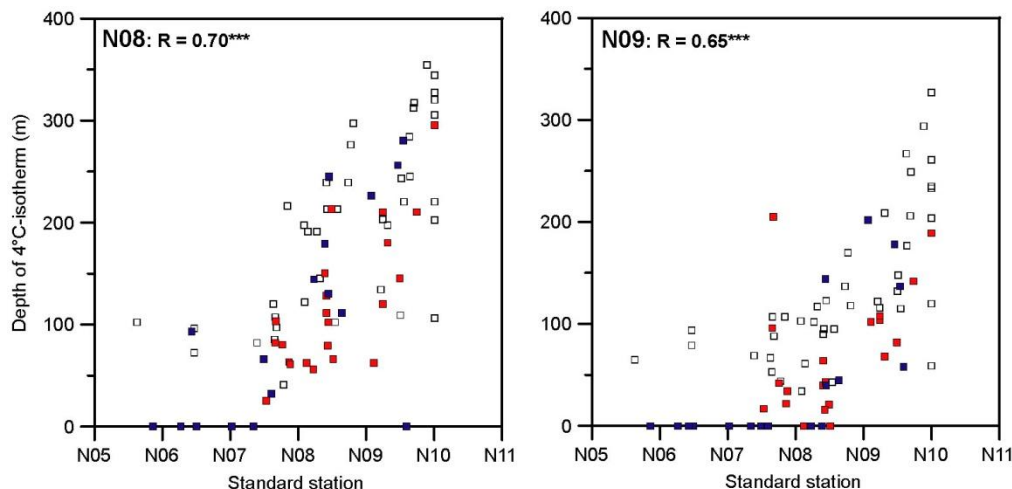
Figure 7.10. The depth of the 4°C-isotherm at stations N08 and N09 plotted against the northern Atlantic water boundary based on CTD data from 80 cruises in the period 1997 – 2018. Blue squares. January-April. Red squares: May. Opens squares: Other months. Correlation coefficients (all months) are shown in the upper left corners.

7.3 Monitoring the northern Atlantic water boundary with PIES

In the monitoring strategy suggested by Hansen et al. (2019b), PIES were to be deployed at stations N05, N07, and N09. The PIES at N09 would be located in the typical boundary region and might help to monitor the boundary location. Often there is, however, little Atlantic water to be found at this location, and the signal measured by the PIES therefore weak. Hence, it might perhaps be better to deploy the PIES at station N08 instead. In order to investigate this more closely, available CTD profiles from these two stations were analyzed in the same way as described in Sect. 2.4.
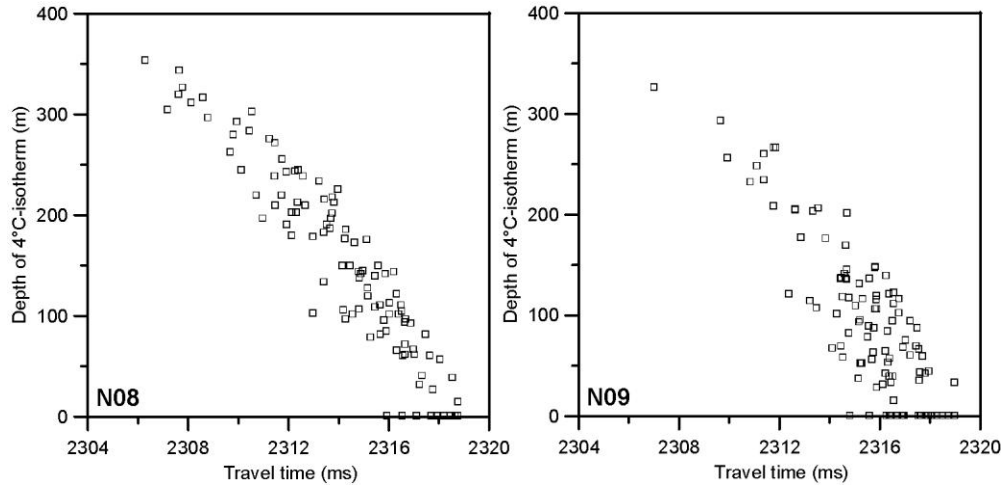
Figure 7.11. Depth of the 4°C-isotherm plotted against travel time for sites N08 and N09 assuming a bottom depth of 1695 m. Each open square represents a CTD profile. Profiles with surface temperature less than 4°C are included with isotherm depth set to zero. The profiles have been extrapolated from 1280 to 1695 m as described in Hansen et al. (2019b).

As for N05 and N07 (Figure 2.8), we can see relationships between travel time and 4°C-isotherm depth both at N08 and N09, but they are more noisy and this is especially the case for N09 (Figure 7.11). There were also more profiles with surface temperature less than 4°C (included in Figure 7.11 with isotherm depth set to zero) so that there was no 4°C-isotherm to monitor. For both stations, the data set had 104 CTD profiles. At N08, nine of these had surface temperature less than 4°C. At N09, the number was 19.

Thus, a PIES at N08 would give considerably more precise measurements of the local isotherm depth than a PIES at N09. In addition to this, N09 has a higher bottom depth (nominally 2169 m) than N08 (nominally 1823 m). Since the PIES is to be deployed on the bottom, a deeper bottom means that the sound has to pass through a longer distance below the isotherm, thereby increasing the noise in the relationship. Since both N08 and N09 are deeper than the depth used for Figure 7.11 (chosen for better comparison with Figure 2.8), the relationship will actually be more noisy than indicated by the figure, but this will especially be the case for N09, which is more than 300 m deeper than N08.
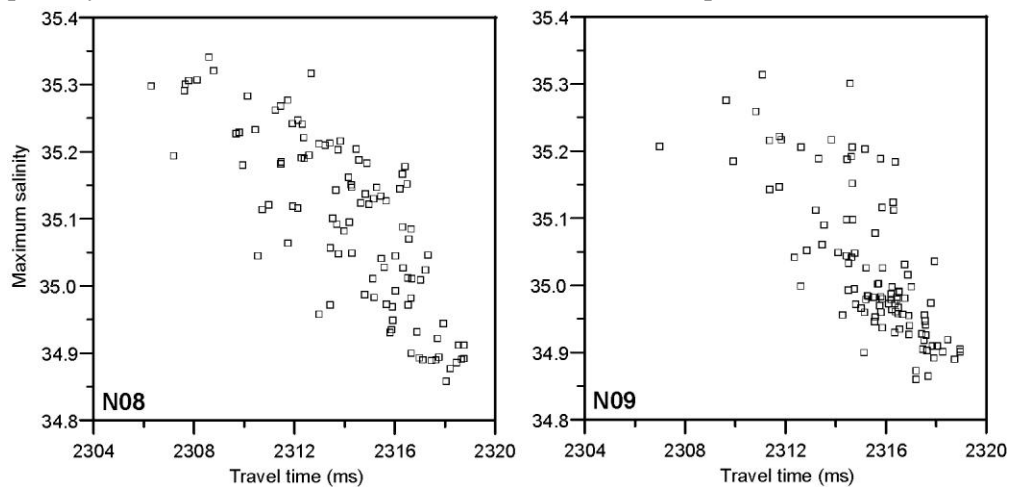
Figure 7.12. Maximum salinity within the 20 – 300 m depth interval plotted against travel time for sites N08 and N09 assuming a bottom depth of 1695 m. Each open square represents a CTD profile. The profiles have been extrapolated from 1280 to 1695 m.

As previously argued, the depth of the 4°C-isotherm is not a good indicator of Atlantic water extent in the boundary region where it is shallow and often "above the surface" in winter. In Sect. 7.1.3, an alternative criterion was suggested, which was based on the maximum salinity in the water column between 20 and 300 m depth. In addition to temperature (and pressure), the sound speed also depends on salinity and, conceivably, the travel time measured by a PIES might be used to determine the maximum salinity. Indeed, there is a relationship, but it is even more noisy than for isotherm depth and, again, especially for station N09 (Figure 7.12).

8 Transport calculation

8.1 Volume transport

The calculation of volume transport follows the same methodology as in Hansen et al. (2015). In their terminology, the eastward velocity at depth z in altimetry interval k at time t is denoted $U_k(z,t)$ and similarly the temperature $T_k(z,t)$ and the salinity $S_k(z,t)$. The volume transport at time t may then be calculated by:

$$Q(t) = \sum_{k=2}^{7} \sum_{z=1m}^{500m} U_k(z, t) \cdot W_k(z, t) \qquad (8.1)$$

where $W_k(z,t)$ is the width of altimetry interval k at depth z and time t. When the whole interval is within the Atlantic water domain, the width is equal to the distance between the two altimetry points at each end of it. At greater depth, the width starts to decrease when the deep boundary of the Atlantic layer is reached and falls to zero at depths where the whole interval is below the deep Atlantic water boundary. Similarly, the width is reduced when the northern boundary enters the interval.

The values for $W_k(z,t)$ are easily calculated once the deep and the northern boundary for Atlantic water extent have been determined (Hansen et al., 2015). For the deep boundary, we have so far used the 4°C-isotherm, as suggested by Hansen et al. (2015). Since the Atlantic water core varies in temperature, it may be argued, however, that the deep Atlantic water boundary should be modified accordingly. If, as an example, the Atlantic water core warms from 8°C to 9°C, it may thus be more appropriate to use the 4.5°C-isotherm rather than the 4°C-isotherm.

Instead of modifying the algorithms to calculate different isotherms, we continue calculating the 4°C-isotherm depth, but then add or subtract a (small) value to this depth. From Table 2.5, the temperature on average decreases by 1°C over a vertical distance of 30 m at the bottom of the Atlantic layer. To calculate the deep Atlantic water boundary, we therefore subtract half this distance, 15 m, from the 4°C-isotherm depth for every degree that the Atlantic water core is warmer than 8°C and add it for every degree that the Atlantic water core is colder than 8°C.

8.1.1 Volume transport dependence on in situ data

The problem is thus reduced to determining monthly averaged 4°C-isotherm depth at stations N04 to N10 and determining the monthly averaged location of the northern boundary. As detailed in Chapter 7, the northern boundary can be simulated from altimetry data and this is the only option available. For the 4°C-isotherm depths, there are, on the other hand, several options, depending on what in situ data are available and reliable. At stations N05 and N07, we use isotherm depths derived from the PIES data, whenever available - and also (interpolated) for N06, when available at both stations, Eq. (5.4).

Determining the 4°C-isotherm depth at station N04 is more problematic, since there are three different options as discussed in Sect. 6.3. In periods with bottom temperature data at site NE (period S3, Sect. 6.3), we use these temperatures to simulate the isotherm depth (Eq. (6.1) with Table 6.2), since that is considered most accurate for monthly averages.

In periods with no data at NE, but with ADCP data at NB (period S2, Sect. 6.3), it would seem tempting to use the ADCP data as described in Sect. 6.2, but the discussion at the end of Sect. 6.3 indicates that this could give rise to problems. To investigate this further, we have calculated three different time series of monthly (and annually) averaged Atlantic water volume transport:

- "Basic" volume transport is calculated using the Atlantic water boundary simulated from altimetry data only.
- "Full" volume transport is based on the northern boundary simulated from altimetry whereas the 4°C-isotherm depth is calculated from all the available data: PIES when available, bottom temperature at NE when available, ADCP data from NB when they are available, but no data at NE, and altimetry when no in situ data available.
- "Full-NB" volume transport is the same as "Full", except that the ADCP data at NB have not been used.

Annually averaged volume transport values for these three different methods do not exhibit large differences between the methods (Figure 8.1a). Thus, inter-annual variations as well as long-term trends will not depend much upon the method, which is encouraging. Nevertheless, we want to use the most accurate estimates.
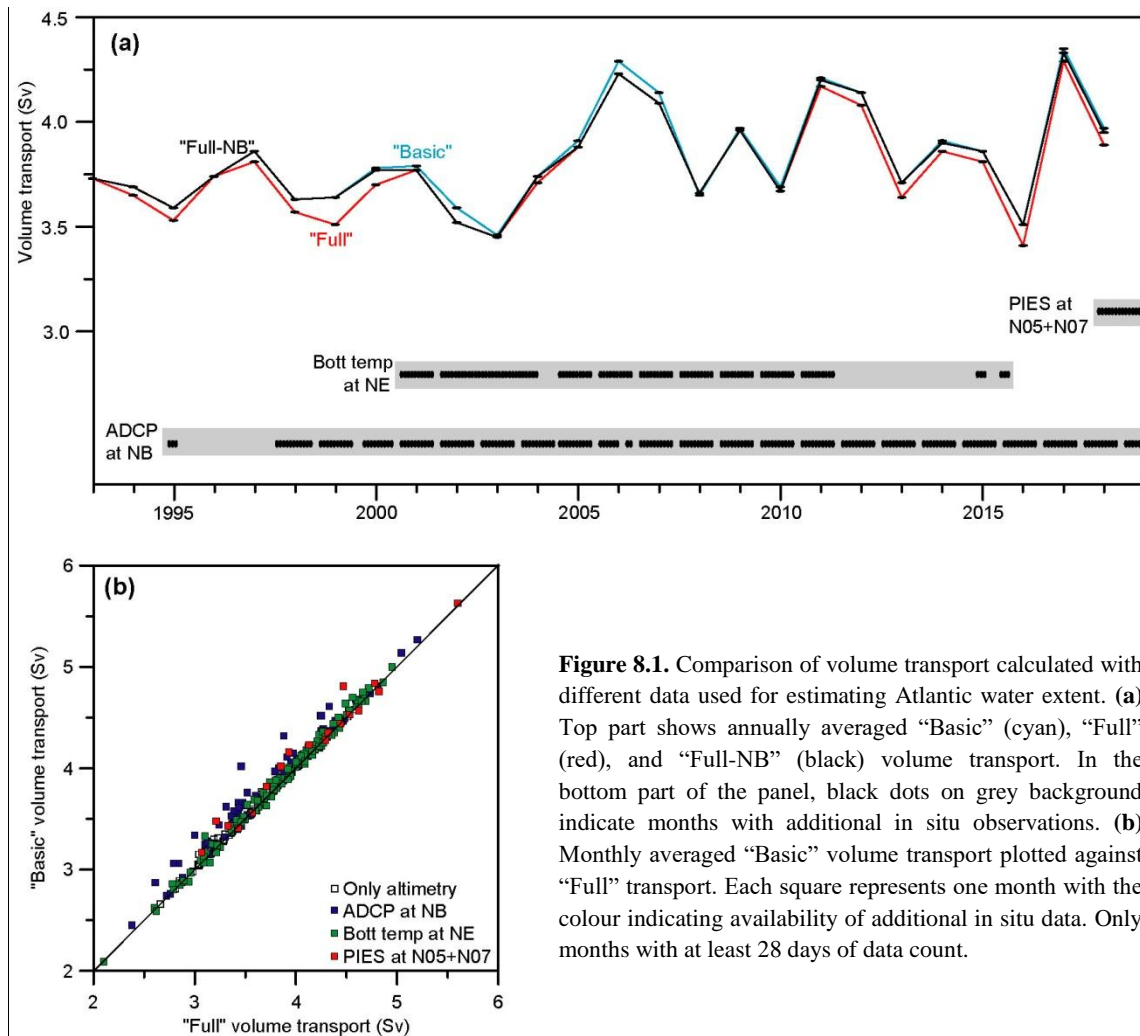
Figure 8.1. Comparison of volume transport calculated with different data used for estimating Atlantic water extent. **(a)** Top part shows annually averaged "Basic" (cyan), "Full" (red), and "Full-NB" (black) volume transport. In the bottom part of the panel, black dots on grey background indicate months with additional in situ observations. **(b)** Monthly averaged "Basic" volume transport plotted against "Full" transport. Each square represents one month with the colour indicating availability of additional in situ data. Only months with at least 28 days of data count.

A priori, one might perhaps expect the accuracy of the transport values to be highest for the "Full" values, somewhat lower for the "Full-NB" values, and lowest for the "Basic" values, but that does not seem to be

the case, as indicated in Figure 8.1b where monthly averaged "Basic" volume transport is plotted against the "Full" transport values. For the green rectangles in this figure, the isotherm depths at N04 are determined from bottom temperature at NE and all of them are almost exactly on the diagonal line. The blue squares, which use ADCP data at NB, in contrast, have several outliers with the "Full" volume transport value considerably lower than the "Basic" value (Table 8.1).

Table 8.1. Comparison of "Basic" volume transport values (with Atlantic water extent from altimetry only) with "Full" transport values (using all the information). In the top row, all the months in the altimetry period are included. The three bottom rows include only months with at least 28 days of data from the three additional types of in situ observations. "N" is number of months. "R" is correlation coefficient. The last four columns list the average (Avg), standard deviation (Std), minimal (Min), and maximal (Max) difference "Full" minus "Basic" volume transport in Sv.

Period	N	R	"Full" – "Basic"			
			Avg	Std	Min	Max
All months:	316	0.990***	−0.05	0.08	−0.56	0.08
Months with ADCP at NB:	221	0.988***	−0.05	0.09	−0.56	0.08
Months with bottom temp at NE:	115	0.996***	−0.02	0.05	−0.23	0.08
Months with PIES at N05+N07:	18	0.986***	−0.08	0.11	−0.34	0.06

To investigate this, we calculated monthly averaged volume transport for the 108 months with both bottom temperature data at NE and ADCP data at NB using the three different methods for estimating Atlantic water depth at station N04 discussed in Sect. 6.3. From the discussion in Chapter 6, the most accurate method for estimating Atlantic water depth at N04 is method S3 (using the bottom temperature at NE) and Figure 8.2 compares transport based on the other two methods with transport based on S3.
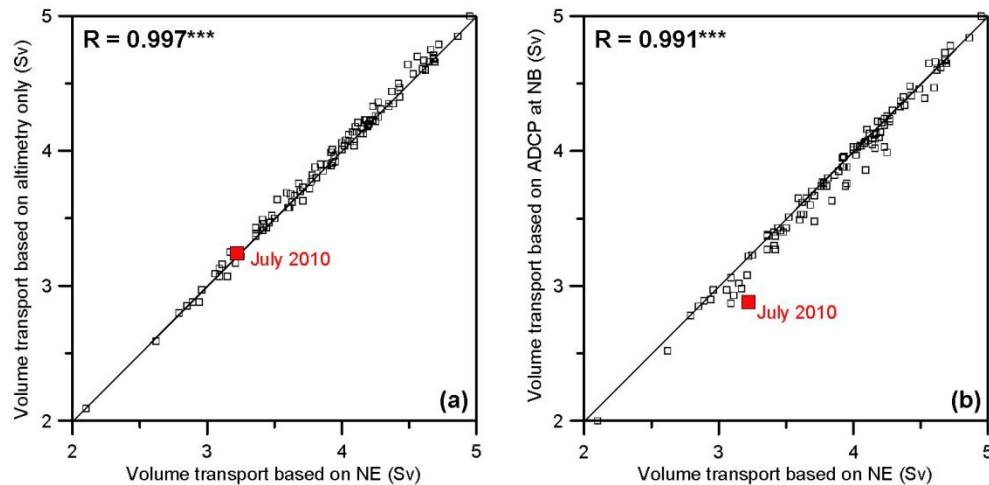
Figure 8.2. Comparison of monthly averaged volume transport calculated with three different methods (Sect. 6.3) used for estimating Atlantic water depth at station N04. **(a)** Transport based on method S1 plotted against transport based on method S3. **(b)** Transport based on method S2 plotted against transport based on method S3.

The (unexpected) message in Figure 8.2 is clear: method S1 is better than method S2. Referring back to Figure 6.6, it seems likely that the outliers in Figure 8.2b are cases where the isotherm depth at N04 is estimated too small, when based on ADCP data at NB, as highlighted for the month of July 2010. Since eastward velocity usually decreases with depth, the transport estimate is more sensitive to isotherm depth when it is small (shallow isotherm) rather than large (deep isotherm).

At a first glance, this conclusion seems depressing since it means that we gain no benefit from using the ADCP data at NB to estimate Atlantic water depth at station N04. In reality, the message is just the opposite: apparently, method S1, which may be used for the whole altimetry period, gives highly accurate volume transport.

Here it must be kept in mind that the only differences between these three methods are for station N04. The Atlantic water depths at all the other stations, as well as the northern boundary, have all been simulated in the same way from altimetry in Figure 8.2. There are, however, 18 months, for which the Atlantic water depths at N05 and N07 have been measured directly by PIES (and interpolated for N06). These are represented by the red squares in Figure 8.1b, which all are close to the diagonal. In Figure 8.1b (and Table 8.1), the Atlantic water depth at N04 was based on ADCP data at NB for most of the PIES period, which may confuse the issue. A clearer picture is presented in Figure 8.3, for which the Atlantic water depth at N04 was based on altimetry only.
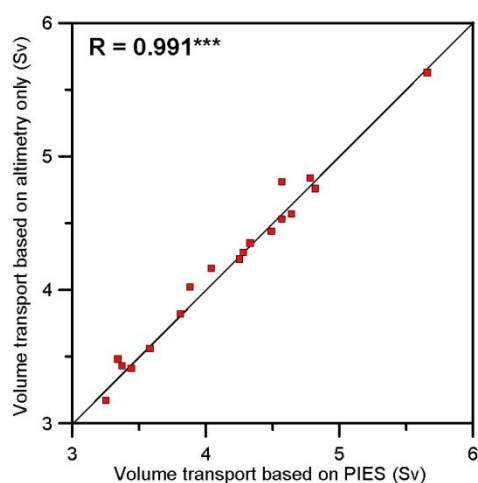
Figure 8.3. Monthly averaged volume transport based on altimetry only ("Basic") plotted against transport based on the isotherm depths measured by PIES at stations N05 and N07 and interpolated at N06 for the 18 calendar months with PIES deployed at both N05 and N07.

Combining the messages from Figure 8.2 and Figure 8.3, we conclude that the "Basic" volume transport, which is based on altimetry data only, agrees remarkably well with the transport for months where in situ observations yield additional data to estimate Atlantic water depth at station N04 (Figure 8.2a) or stations N05, N06, and N07 (Figure 8.3).

8.1.2 "New" time series of Atlantic water volume transport for the Faroe Current

Based on the analyses documented in this report, we have generated "new" time series of monthly, as well as annually, averaged volume transport of Atlantic water in the Faroe Current from January 1993 to April 2019. This is the "Full-NB" series defined above. For all months in this series, the velocity field is based on the calibrated altimetry data, as discussed in Hansen et al. (2019a). For most months, the Atlantic water extent is also based on altimetry data only. For months with PIES measurements, these data have been used to estimate the depths of the 4°C-isotherm (and hence Atlantic water depth) at the PIES deployment sites and for months with PIES at both N05 and N07, the 4°C-isotherm depth at N06 has been interpolated by Eq. (5.4). For months with bottom temperature measurements at NE, the depth of the 4°C-isotherm at N04, similarly, has been estimated from these measurements using Eq. (6.1) with Table 6.2.

The accuracy of the transport estimates is considered to be highest for months with additional in situ data (PIES or bottom temperature at NE), which is illustrated in the bottom part of Figure 8.1a. From the

discussion in Sect. 8.1.1, however, the accuracy appears to be remarkably high even for months with no in situ observations, when the volume transport is based on (calibrated) altimetry data only.

As documented in Table 1.3 and Figure 1.3, the "new" time series of monthly and annually averaged volume transport differ very little from the old series (Hansen et al., 2019a). The difference in overall averages is marginal and well below the quoted uncertainty (± 0.5 Sv) with a high correlation between the monthly averaged series.

8.2 Heat transport

Since most of the water leaving the Arctic Mediterranean has average temperatures close to $0°C$, it is common practice to use this value as a reference temperature for heat transport. Hansen et al. (2015) furthermore argued that also heat below the $4°C$ isotherm ought to be included and the time series of heat transport in that study included all the water south of the northern boundary down to 500 m for which the simulated temperature was above $0°C$. For consistency, we have retained the heat transport time series defined in this way and this is the basis for the values listed in Table 1.3 in the introduction.

In addition to this, we also calculate monthly averaged time series of transport-averaged temperature within the Atlantic water domain only, i.e., the product of monthly averaged temperature and eastward velocity integrated over the Atlantic water domain each month divided by the volume transport for the month, which is calculated as follows:

$$\Theta(t) = \frac{\sum_{k=2}^{7} \sum_{z=1m}^{500m} U_k(z,t) \cdot T_k(z,t) \cdot W_k(z,t)}{Q(t)} \qquad (8.2)$$

The advantage of a transport-averaged temperature is that it is independent of the choice of reference temperature. When combined with volume transport, the heat carried by the Atlantic part of the Faroe Current can be calculated for any value of reference temperature.

8.3 Salt/freshwater transport

In contrast to heat, the absolute salt transport of a current is well defined even if the system is not closed, but often salt transport is defined relative to some reference salinity or converted to a freshwater transport, which again depends on a reference salinity. This has introduced considerable confusion and discussion (e.g., https://asof.awi.de/outputs/asof-issg-meetings-workshops/copenhagen-april-2019/). In Hansen et al. (2015), the absolute salt transport of the Faroe Current was furthermore defined to include (Atlantic-derived) salt carried by the flow outside (below) the Atlantic water domain of the current in analogy to the heat transport discussed in Sect. 8.2. To calculate this salt transport, it was furthermore necessary to introduce a "boundary salinity" (Sect. 6.2 in the supplement to Hansen et al., 2015), which has introduced even more confusion.

To avoid this confusion, we no longer report values for salt transport of the Faroe Current. Instead, we report monthly values for the transport-averaged salinity of the (Atlantic water part of the) Faroe Current, which is defined as:

$$\Psi(t) = \frac{\sum_{k=2}^{7} \sum_{z=1m}^{500m} U_k(z,t) \cdot S_k(z,t) \cdot W_k(z,t)}{Q(t)} \qquad (8.3)$$

where $S_k(z,t)$ is the salinity at depth z in altimetry interval k at time t. As seen in Figure 1.4b, the transport-averaged salinity of the (Atlantic part of the) Faroe Current exhibits similar long-term variations as the Atlantic core, but with considerably lower values. Seasonal variability is much less pronounced than for transport-averaged temperature. With monthly values for both volume transport and transport-averaged salinity, the salt transport of the (Atlantic part of the) Faroe Current, $Q_S(t)$, is easily calculated once a reference salinity, S_{ref}, has been defined:

$$Q_S(t) = \mu \cdot Q(t) \cdot \left[\Psi(t) - S_{ref} \right] \qquad (8.4)$$

where the factor μ (≈ 1.03 kg m^{-3}) is needed to convert salinity to salt content per volume sea water. Similarly, we can define an equivalent freshwater transport, $Q_{fresh}(t)$, as the negative of the transport of fresh water that would be needed to maintain a constant reference salinity, S_{ref}, in the reservoir, which leads to:

$$Q_{fresh}(t) = -Q(t) \cdot \frac{\left[\Psi(t) - S_{ref} \right]}{S_{ref}} \qquad (8.5)$$

References

Hansen, B., Meincke, J. (1979). Eddies and meanders in the Iceland–Faroe Ridge area. Deep-Sea Research, 26, 1067–1082.

Hansen, B., Østerhus, S., Hátún, H., Kristiansen, R., Larsen, K. M. H. (2003). The Iceland-Faroe inflow of Atlantic water to the Nordic Seas, Prog. Oceanogr., 59, 443-474, doi:10.1016/j.pocean.2003.10.003, 2003.

Hansen, B., Larsen, K. M. H., Hátún, H., Kristiansen, R., Mortensen, E., Østerhus, S. (2015). Transport of volume, heat, and salt towards the Arctic in the Faroe Current 1993–2013. Ocean Sci., 11, 743-757. doi:10.5194/os-11-743-2015.

Hansen, B., Larsen, K. M. H., Hátún, H. (2019a). Monitoring the velocity structure of the Faroe Current. Havstovan Technical Report Nr.: 19-01. (http://www.hav.fo/PDF/Ritgerdir/2019/TechRep1901.pdf).

Hansen, B., Larsen, K. M. H., Hátún, H., Jochumsen, K., Østerhus, S. (2019b). Monitoring the hydrographic structure of the Faroe Current. Havstovan Technical Report Nr.: 19-02. (http://www.hav.fo/PDF/Ritgerdir/2019/TechRep1902.pdf).

Kennelly, M., Tracey, K. L., Watts, R. D. (2007). Inverted Echo Sounder Data Processing Manual. Physical Oceanography Technical Reports. Paper 2. http://digitalcommons.uri.edu/physical_oceanography_techrpts/2

Larsen, K. M. H., Hátún, H., Hansen, B., Kristiansen, R. (2012). Atlantic water in the Faroe area: sources and variability, ICES J. Mar. Sci., 69, 802-808, doi:10.1093/icesjms/fss028.

Pyper, B. J., Peterman, R. M. (1998). Comparison of methods to account for autocorrelation in correlation analyses of fish data, Can. J. Fish. Aquat. Sci., 55, 2127–2140, https://doi.org/10.1139/f98-104.

<u>Appendix A:</u>
Iterative procedure for splitting seasonal and long-term variations

The time series considered in this study may be seen as super-positions of slowly varying signals + seasonal signals + random variations. We use an iterative decomposition method to separate seasonal and long-term variations. The seasonal variation generally has a roughly sinusoidal shape, and a simple analysis may be made by regressing the time series on a sinusoidal seasonal variation, where the phase lag is varied to give maximum correlation. The long-term variation may then be calculated as a running mean of de-seasoned values. From the determined long-term variation, a new estimate of seasonal variation can be achieved.

This procedure is repeated iteratively and rapidly converges so that we get a seasonal signal that is not so much contaminated by long-term variations and we get a time series of a 3-year-running mean, which is the average of all the de-seasoned values within each 3-year period. In addition to the average, we also calculate the standard error of each 3-year mean value.

Appendix B:
Characteristics of the seasonal property variations

The iterative procedure described in Appendix A has been used to analyze CTD data to determine the seasonal and long-term variations of the properties (temperature, salinity, sigma-theta) for selected depths at all the CTD standard stations. The table below lists the number of CTD profiles included in the analysis for each depth and station.

```
===========================================================================================
Number of CTD observations for each depth at each standard station

Depth   N01   N02   N03   N04   N05   N06   N07   N08   N09   N10   N11   N12   N13   N14
 10m    155   152   142   135   133   120   122   117   116   114   110   100    98   100
100m          128   142   135   133   120   122   117   116   114   110   100    98   100
200m                 33   135   133   120   122   117   116   114   110   100    98   100
300m                      135   133   120   122   117   116   114   110   100    98   100
400m                      134   133   119   122   117   116   114   110   100    98   100
500m                      104   133   119   122   117   116   114   110   100    98   100
600m                           132   119   120   117   115   114   110   100    96   100
700m                           131   119   120   117   115   114   109    99    95   100
800m                           130   118   120   117   115   114   109    99    95    97
900m                           129   118   119   116   114   113   109    99    95    96
1000m                          124   111   113   112   108   107   104    95    90    88
1100m                          116   101   105   105   104   103    98    87    84    83
1200m                          110   100   105   105   104   102    98    86    82    83
```

On the following three pages, the characteristics for each property are listed separately. For each property, there are three tables listing: the maximum correlation coefficient of the sinusoidal seasonal fit (Appendix A), the amplitude of the seasonal variation, and the day number of property maximum.

Appendix B continued:

Temperature

```
================================================================================================
Maximum correlation coefficient for temperature
```

Depth	N01	N02	N03	N04	N05	N06	N07	N08	N09	N10	N11	N12	N13	N14
10m	0.97	0.95	0.91	0.87	0.81	0.78	0.83	0.80	0.81	0.90	0.93	0.94	0.94	0.95
100m		0.97	0.93	0.65	0.44	0.43	0.54	0.50	0.44	0.48	0.38	0.43	0.27	0.46
200m				0.49	0.36	0.38	0.50	0.41	0.30	0.17	0.25	0.29	0.19	0.10
300m				0.38	0.28	0.38	0.44	0.37	0.36	0.12	0.12	0.27	0.15	0.05
400m				0.23	0.18	0.32	0.43	0.35	0.29	0.16	0.15	0.25	0.18	0.09
500m				0.09	0.14	0.36	0.36	0.31	0.23	0.08	0.18	0.23	0.19	0.08
600m					0.20	0.37	0.33	0.24	0.10	0.08	0.18	0.20	0.22	0.08
700m					0.17	0.35	0.30	0.21	0.09	0.07	0.12	0.27	0.23	0.07
800m					0.17	0.29	0.28	0.19	0.07	0.14	0.15	0.27	0.33	0.12
900m					0.15	0.25	0.27	0.18	0.07	0.15	0.12	0.21	0.29	0.10
1000m					0.11	0.22	0.25	0.20	0.09	0.12	0.12	0.14	0.25	0.12
1100m					0.05	0.20	0.26	0.24	0.11	0.12	0.15	0.26	0.34	0.19
1200m					0.07	0.17	0.29	0.28	0.13	0.13	0.13	0.21	0.34	0.17

```
Seasonal amplitude for temperature (°C)
```

Depth	N01	N02	N03	N04	N05	N06	N07	N08	N09	N10	N11	N12	N13	N14
10m	1.78	1.66	1.64	1.81	1.85	1.98	2.30	2.55	2.75	3.12	3.32	3.46	3.52	3.56
100m		1.63	0.95	0.76	0.82	1.00	1.34	1.41	0.95	0.70	0.40	0.38	0.19	0.27
200m				0.75	0.97	1.16	1.51	1.08	0.48	0.16	0.16	0.16	0.10	0.06
300m				0.82	0.86	1.07	1.05	0.62	0.30	0.09	0.06	0.12	0.08	0.03
400m				0.60	0.40	0.49	0.53	0.29	0.13	0.09	0.05	0.08	0.06	0.03
500m				0.20	0.14	0.29	0.21	0.12	0.05	0.03	0.03	0.04	0.03	0.01
600m					0.07	0.12	0.08	0.05	0.01	0.01	0.02	0.02	0.02	0.01
700m					0.03	0.06	0.04	0.03	0.01	0.01	0.01	0.02	0.01	0.00
800m					0.02	0.03	0.03	0.02	0.00	0.01	0.01	0.01	0.01	0.01
900m					0.01	0.02	0.02	0.02	0.00	0.01	0.00	0.01	0.01	0.00
1000m					0.01	0.01	0.02	0.01	0.00	0.01	0.00	0.00	0.01	0.00
1100m					0.00	0.01	0.02	0.02	0.00	0.01	0.00	0.01	0.01	0.00
1200m					0.00	0.01	0.02	0.02	0.00	0.00	0.00	0.00	0.01	0.00

```
Day number of seasonal temperature maximum
```

Depth	N01	N02	N03	N04	N05	N06	N07	N08	N09	N10	N11	N12	N13	N14
10m	254	252	244	238	234	236	231	231	234	241	244	242	242	241
100m		259	262	259	275	280	266	278	277	289	301	333	321	328
200m				273	296	281	270	276	264	287	351	51	23	12
300m				287	299	267	261	259	249	216	348	73	23	13
400m				307	302	263	248	249	255	238	319	53	13	22
500m				10	270	246	246	256	268	232	350	40	3	24
600m					273	256	247	248	262	289	362	56	20	355
700m					274	259	236	242	254	365	363	57	38	21
800m					283	262	224	228	263	362	5	61	46	4
900m					274	251	206	203	322	23	29	50	39	9
1000m					263	240	185	179	344	9	18	44	48	45
1100m					271	209	161	157	344	26	364	79	24	73
1200m					96	193	147	146	315	37	33	74	24	51

Appendix B continued:

Salinity

```
===============================================================================================
```
Maximum correlation coefficient for salinity

Depth	N01	N02	N03	N04	N05	N06	N07	N08	N09	N10	N11	N12	N13	N14
10m	0.47	0.48	0.57	0.54	0.56	0.46	0.52	0.53	0.56	0.46	0.41	0.54	0.47	0.47
100m		0.41	0.47	0.36	0.17	0.21	0.41	0.28	0.34	0.27	0.28	0.15	0.24	0.31
200m				0.35	0.29	0.42	0.53	0.41	0.32	0.20	0.27	0.02	0.19	0.23
300m				0.35	0.28	0.40	0.39	0.34	0.27	0.09	0.09	0.22	0.19	0.18
400m				0.30	0.19	0.23	0.30	0.15	0.22	0.24	0.18	0.23	0.16	0.05
500m				0.18	0.12	0.14	0.03	0.07	0.14	0.23	0.08	0.15	0.22	0.16
600m					0.13	0.09	0.19	0.19	0.19	0.17	0.13	0.23	0.17	0.21
700m					0.25	0.32	0.28	0.25	0.22	0.21	0.19	0.23	0.16	0.23
800m					0.27	0.33	0.30	0.27	0.16	0.18	0.25	0.23	0.19	0.25
900m					0.29	0.35	0.27	0.26	0.19	0.22	0.22	0.28	0.21	0.22
1000m					0.31	0.37	0.25	0.26	0.25	0.24	0.22	0.22	0.27	0.17
1100m					0.30	0.35	0.23	0.19	0.26	0.26	0.23	0.27	0.29	0.15
1200m					0.23	0.31	0.22	0.17	0.22	0.25	0.17	0.23	0.33	0.15

Seasonal amplitude for salinity

Depth	N01	N02	N03	N04	N05	N06	N07	N08	N09	N10	N11	N12	N13	N14
10m	0.024	0.022	0.024	0.052	0.086	0.082	0.104	0.120	0.122	0.066	0.043	0.051	0.042	0.042
100m		0.019	0.020	0.043	0.030	0.044	0.081	0.059	0.052	0.028	0.021	0.009	0.015	0.017
200m				0.041	0.052	0.080	0.100	0.057	0.027	0.013	0.009	0.001	0.007	0.007
300m				0.050	0.049	0.057	0.043	0.020	0.010	0.003	0.002	0.004	0.004	0.003
400m				0.040	0.015	0.011	0.010	0.003	0.003	0.006	0.002	0.002	0.002	0.000
500m				0.011	0.003	0.003	0.000	0.001	0.001	0.002	0.000	0.001	0.001	0.001
600m					0.001	0.001	0.001	0.001	0.001	0.001	0.000	0.001	0.001	0.001
700m					0.002	0.002	0.001	0.001	0.001	0.001	0.001	0.001	0.001	0.001
800m					0.001	0.001	0.001	0.001	0.001	0.001	0.001	0.001	0.001	0.001
900m					0.001	0.001	0.001	0.001	0.001	0.001	0.001	0.001	0.001	0.001
1000m					0.001	0.001	0.001	0.001	0.001	0.001	0.001	0.001	0.001	0.001
1100m					0.001	0.001	0.001	0.001	0.001	0.001	0.001	0.001	0.001	0.000
1200m					0.001	0.001	0.001	0.001	0.001	0.001	0.000	0.001	0.001	0.000

Day number of seasonal salinity maximum

Depth	N01	N02	N03	N04	N05	N06	N07	N08	N09	N10	N11	N12	N13	N14
10m	125	112	118	122	111	116	130	130	118	109	102	97	102	114
100m		146	192	189	187	215	223	244	226	235	226	237	205	243
200m				251	284	264	258	273	259	260	268	206	348	307
300m				273	286	264	265	255	266	233	309	85	16	324
400m				295	299	299	245	217	264	230	270	61	11	41
500m				13	276	234	192	314	217	205	249	96	89	188
600m					75	101	58	82	129	158	121	158	136	166
700m					107	92	83	91	131	132	108	150	157	175
800m					123	103	80	91	136	140	120	147	146	170
900m					122	108	82	95	148	149	120	147	153	175
1000m					125	97	83	97	136	150	123	147	151	169
1100m					127	98	88	91	144	152	129	143	154	158
1200m					134	99	89	106	139	153	114	146	151	160

Appendix B continued:

Sigma-theta

```
==============================================================================================
Maximum correlation coefficient for sigma-theta
```

Depth	N01	N02	N03	N04	N05	N06	N07	N08	N09	N10	N11	N12	N13	N14
10m	0.97	0.96	0.91	0.89	0.88	0.89	0.91	0.90	0.90	0.91	0.91	0.92	0.93	0.92
100m		0.97	0.93	0.80	0.70	0.64	0.68	0.65	0.52	0.50	0.42	0.45	0.35	0.38
200m				0.65	0.44	0.39	0.50	0.38	0.27	0.11	0.30	0.35	0.18	0.17
300m				0.45	0.27	0.35	0.42	0.35	0.32	0.13	0.14	0.27	0.11	0.10
400m				0.19	0.14	0.31	0.41	0.38	0.25	0.09	0.17	0.23	0.17	0.11
500m				0.06	0.11	0.37	0.39	0.30	0.23	0.05	0.20	0.23	0.23	0.15
600m					0.22	0.37	0.34	0.26	0.15	0.13	0.19	0.19	0.23	0.17
700m					0.22	0.38	0.31	0.24	0.16	0.13	0.16	0.22	0.22	0.17
800m					0.23	0.33	0.30	0.23	0.13	0.18	0.23	0.19	0.24	0.23
900m					0.23	0.31	0.26	0.19	0.18	0.20	0.18	0.21	0.26	0.23
1000m					0.23	0.33	0.21	0.16	0.23	0.22	0.20	0.17	0.25	0.18
1100m					0.21	0.28	0.16	0.13	0.26	0.22	0.23	0.18	0.33	0.13
1200m					0.11	0.23	0.14	0.11	0.25	0.22	0.14	0.18	0.36	0.15

```
Seasonal amplitude for sigma-theta
```

Depth	N01	N02	N03	N04	N05	N06	N07	N08	N09	N10	N11	N12	N13	N14
10m	0.289	0.276	0.280	0.314	0.333	0.346	0.367	0.389	0.423	0.449	0.468	0.502	0.502	0.504
100m		0.260	0.142	0.106	0.114	0.120	0.132	0.130	0.084	0.063	0.038	0.038	0.025	0.028
200m				0.076	0.081	0.082	0.101	0.069	0.031	0.007	0.015	0.015	0.006	0.006
300m				0.069	0.055	0.065	0.065	0.038	0.017	0.005	0.004	0.006	0.003	0.002
400m				0.033	0.020	0.031	0.031	0.018	0.006	0.002	0.003	0.003	0.003	0.002
500m				0.008	0.007	0.016	0.012	0.007	0.003	0.001	0.002	0.002	0.002	0.001
600m					0.005	0.007	0.005	0.003	0.001	0.001	0.001	0.001	0.001	0.001
700m					0.003	0.004	0.003	0.002	0.001	0.001	0.001	0.001	0.001	0.001
800m					0.002	0.003	0.002	0.002	0.001	0.001	0.001	0.001	0.001	0.001
900m					0.002	0.002	0.002	0.001	0.001	0.001	0.001	0.001	0.001	0.001
1000m					0.001	0.002	0.001	0.001	0.001	0.001	0.001	0.001	0.001	0.001
1100m					0.001	0.001	0.001	0.001	0.001	0.001	0.001	0.001	0.001	0.000
1200m					0.001	0.001	0.001	0.000	0.001	0.001	0.000	0.000	0.001	0.000

```
Day number of seasonal sigma-theta
```

Depth	N01	N02	N03	N04	N05	N06	N07	N08	N09	N10	N11	N12	N13	N14
10m	75	72	65	63	62	63	62	63	64	63	64	62	62	62
100m		80	86	95	103	109	102	105	112	118	140	162	164	174
200m				100	116	103	94	91	79	112	199	231	240	254
300m				113	121	82	74	76	59	20	181	245	211	281
400m				134	117	68	65	69	69	65	164	225	192	201
500m				194	75	63	64	69	96	108	176	210	165	198
600m					87	74	64	68	101	130	165	208	185	168
700m					98	81	64	70	108	149	142	205	198	182
800m					112	88	58	66	117	159	144	199	198	175
900m					110	87	50	57	145	170	142	174	186	179
1000m					112	81	40	47	141	161	142	168	176	184
1100m					121	72	28	17	147	165	143	170	173	191
1200m					146	69	10	361	138	167	139	167	166	181

Appendix C:
Miscellaneous tables

Table C1. Main characteristics of the 4°C-isotherm at standard stations on the section based on CTD observations 1987 – 2019. The table lists the number of CTD profiles at each station, the percentage of profiles with surface water being warmer than 4°C, the average depth of the 4°C-isotherm and its standard deviation where only occupations with the 4°C-isotherm within the CTD profile are included. Copied from Hansen et al. (2019).

Station:	N01	N02	N03	N04	N05	N06	N07	N08	N09	N10	N11	N12	N13	N14
Number CTD:	155	152	142	135	133	120	122	117	116	114	110	100	98	100
Surf > 4°C:	100	100	100	100	98	99	96	91	82	78	75	78	73	79
Avg D_4 (m):				387	297	244	202	161	114	78	73	69	67	65
Std D_4 (m):				77	100	102	95	83	69	49	37	33	30	29

Table C2. Number of CTD cruises (N) and correlation coefficient between the measured 4°C-isotherm depth at one station and the average of the isotherm depths at the two neighbouring stations. The last row lists the Root-Mean-Square error made by replacing the measured value by the average. Only cruises where CTD profiles were acquired from all three stations within 24 hours are included. Copied from Hansen et al. (2019).

Station:	N05	N06	N07	N08	N09
No cruises:	108	115	114	112	110
Correlation C.:	0.82***	0.86***	0.89***	0.82***	0.84***
RMS:	48m	40m	35m	40m	28m

Appendix C continued:

Table C3. Depth of 4°C-isotherm at station N04 (D04) and station N05 (D05) as well as their average (DNB) and difference (dif) on CTD cruises 1997-2016. The times of station occupation are shown as well as the time difference in hours (dt).

Cru-ise	N04-time yyyymmddhh	N05-time yyyymmddhh	D04 m	D05 m	DNB m	dif m	dt h	Cru-ise	N04-time yyyymmddhh	N05-time yyyymmddhh	D04 m	D05 m	DNB m	dif m	dt h
9748	1997061306	1997061309	316	296	306	20	3	0708	2007021601	2007021603	452	357	405	95	2
9764	1997082907	1997082909	444	383	414	61	2	0728	2007042908	2007042906	393	275	334	118	2
9808	1998021212	1998021214	461	382	422	79	2	0732	2007051601	2007051523	356	246	301	110	2
9832	1998051907	1998051905	427	303	365	124	2	0764	2007083003	2007083004	409	384	397	25	1
9848	1998070602	1998070600	399	377	388	22	1	0804	2008030612	2008030613	434	410	422	24	1
9864	1998091505	1998091508	466	357	412	109	3	0824	2008051312	2008051310	250	181	216	69	2
9888	1998110820	1998110822	453	354	404	99	2	0866	2008082900	2008082902	356	319	338	37	2
9908	1999022310	1999022312	376	150	263	226	2	0888	2008110606	2008110607	435	322	379	113	1
9932	1999052508	1999052506	91	142	117	-51	1	0904	2009021919	2009021921	374	193	284	181	1
9940	1999061415	1999061413	299	82	191	217	2	0932	2009051204	2009051202	346	418	382	-72	2
9964	1999091015	1999091016	404	345	375	59	1	0972	2009082723	2009082801	431	294	363	137	2
9988	1999110800	1999110801	364	271	318	93	1	0992	2009110600	2009110601	431	284	358	147	1
0012	2000030422	2000030423	444	306	375	138	1	1014	2010051111	2010051109	225	353	289	-128	2
0032	2000052512	2000052514	438	316	377	122	2	1032	2010090200	2010090201	452	424	438	28	1
0040	2000061701	2000061623	246	44	145	202	2	1042	2010110404	2010110406	387	389	388	-2	2
0060	2000090813	2000090817	448	429	439	19	4	1102	2011021708	2011021709	451	392	422	59	1
0084	2000110616	2000110617	381	343	362	38	0	1116	2011051602	2011051600	401	267	334	134	2
0108	2001022707	2001022709	371	291	331	80	2	1134	2011090100	2011090101	357	170	264	187	1
0132	2001051609	2001051613	416	359	388	57	4	1144	2011110318	2011110320	462	364	413	98	2
0140	2001061506	2001061508	368	209	289	159	2	1202	2012021608	2012021610	355	252	304	103	2
0160	2001090619	2001090621	389	336	363	53	2	1220	2012052119	2012052117	368	267	318	101	2
0184	2001110420	2001110422	440	371	406	69	2	1236	2012100717	2012100718	411	323	367	88	1
0208	2002022107	2002022109	418	467	443	-49	2	1302	2013021416	2013021418	407	259	333	148	2
0232	2002051804	2002051806	354	86	220	268	1	1320	2013051220	2013051218	465	363	414	102	2
0264	2002090523	2002090600	465	231	348	234	1	1342	2013082900	2013082905	461	441	451	20	4
0280	2002101915	2002101917	381	396	389	-15	2	1402	2014021704	2014021708	403	360	382	43	3
0284	2002110106	2002110108	271	205	238	66	1	1414	2014042423	2014042502	417	249	333	168	2
0308	2003022104	2003022105	447	303	375	144	1	1416	2014051202	2014051122	339	360	350	-21	4
0328	2003042815	2003042818	349	318	334	31	3	1422	2014060520	2014060600	374	329	352	45	4
0332	2003052415	2003052410	456	503	480	-47	4	1434	2014082720	2014082721	425	383	404	42	1
0334	2003053018	2003053019	435	395	415	40	1	1502	2015021408	2015021409	489	461	475	28	1
0364	2003090420	2003090421	374	273	324	101	1	1516	2015051401	2015051323	353	246	300	107	2
0388	2003103105	2003103106	449	386	418	63	1	1534	2015090505	2015090503	406	269	338	137	2
0408	2004022007	2004022008	202	47	125	155	1	1602	2016021202	2016021204	426	318	372	108	2
0428	2004051921	2004051923	357	123	240	234	2	1618	2016051610	2016051609	399	274	337	125	1
0448	2004070500	2004070502	269	286	278	-17	2	1624	2016060822	2016060823	461	226	344	235	1
0464	2004090500	2004090501	510	434	472	76	1	1636	2016090108	2016090110	397	162	280	235	2
0492	2004111201	2004111203	349	290	320	59	2	1702	2017021523	2017021601	456	268	362	188	2
0508	2005022109	2005022110	444	174	309	270	1	1714	2017042309	2017042311	446	406	426	40	2
0536	2005052104	2005052102	341	105	223	236	2	1718	2017051416	2017051414	399	274	337	125	2
0568	2005090115	2005090116	377	370	374	7	1	1742	2017083105	2017083107	476	438	457	38	2
0588	2005111101	2005111103	452	430	441	22	2	1802	2018021206	2018021208	382	425	404	-43	2
0608	2006021604	2006021605	319	342	331	-23	1	1821	2018051500	2018051421	469	449	459	20	2
0644	2006061003	2006061001	415	260	338	155	2	1838	2018083002	2018083004	356	324	340	32	2
0664	2006083123	2006090101	527	385	456	142	2	1902	2019021522	2019021600	437	385	411	52	1
0684	2006111003	2006111004	431	291	361	140	1	1919	2019051403	2019051400	411	241	326	170	3

Appendix C continued:

Table C4. ADCP deployments at site NB listing deployment id (Depl-id), Instrument (Instr.), Period (full days), number of days, depth range (m), and values for A and 2α in Eq. (4.2) derived from the minimum intensity profiles in Figure 4.1. BB = BroadBand ADCP. LR = Long Ranger ADCP.

Depl-id	Inst	Period	Days	Depth	A	2α
NWNB9706	BB-1284	19970614-19980612	364	73-623	122.8	0.069
NWNB9807	BB-1245	19980705-19990618	349	72-672	126.8	0.069
NWNB9908	BB-1577	19990821-20000615	300	79-679	122.8	0.055
NWNB0007	BB-1577	20000708-20010615	343	101-676	124.8	0.062
NWNB0107	BB-1577	20010707-20020614	343	102-702	125.8	0.060
NWNB0207	BB-1577	20020706-20030613	343	103-703	122.8	0.051
NWNB0307	BB-1577	20030706-20040610	341	90-665	127.8	0.064
NWNB0407	BB-1577	20040703-20050519	321	97-697	121.8	0.053
NWNB0506	BB-1577	20050612-20060126	229	116-666	121.8	0.055
NWNB0606	BB-1577	20060610-20070517	342	144-669	119.6	0.055
NWNB0706	BB-1577	20070609-20080517	344	116-666	118.6	0.049
NWNB0806	BB-1577	20080607-20090514	342	114-664	117.6	0.049
NWNB0906	BB-1577	20090606-20100513	342	120-670	117.6	0.045
NWNB1006	BB-1577	20100605-20110519	349	122-672	112.6	0.041
NWNB1106	BB-1577	20110611-20120519	344	112-662	118.6	0.049
NWNB1206	BB-1577	20120609-20130516	342	121-671	118.8	0.051
NWNB1306	LR-9518	20130610-20140514	339	71-691	167.9	0.094
NWNB1406	LR-9518	20140607-20150524	352	66-686	170.9	0.094
NWNB1506	BB-1644	20150615-20160518	339	132-657	118.8	0.023

Table C5. Explained variance (R^2) by Eq. (5.2) for various choices of the parameter $x_j(t)$ (listed in the leftmost column) and for the three alternative ways to treat de-trending and de-seasoning (Tables C5a, C5b, C5c). Highest R^2 values are underlined bold.

Table C5a. Both the altimetry parameters and isotherm depths are the raw data without any de-trending or de-seasoning.

Station:	N04	N05	N06	N07	N08	N09	N10
None :	0.221	0.443	0.442	0.601	0.574	0.538	0.472
U1 :	0.223	0.443	0.443	0.601	0.578	0.538	0.475
U2 :	0.260	0.508	0.447	0.602	0.579	0.539	**0.483**
U3 :	0.229	0.563	0.487	0.609	0.579	0.541	0.472
U4 :	0.253	0.446	0.450	0.621	0.578	0.538	0.474
U5 :	0.294	0.585	0.496	0.602	0.597	**0.546**	0.473
U6 :	0.233	0.523	**0.570**	**0.654**	0.574	0.542	0.475
U7 :	0.222	0.446	0.449	0.654	**0.616**	0.545	0.474
PcAH-1:	**0.307**	**0.618**	0.532	0.632	0.588	0.543	0.477
PcAH-2:	0.243	0.443	0.442	0.604	0.577	0.538	0.474
PcAH-3:	0.280	0.599	0.535	0.628	0.576	0.541	0.472
PcAU-1:	0.224	0.459	0.486	0.642	0.577	0.539	0.473
PcAU-2:	0.297	0.594	0.490	0.604	0.591	0.545	0.472
PcAU-3:	0.225	0.443	0.473	0.631	0.585	0.538	0.483

Table C5b. The altimetry parameters were de-trended and de-seasoned.and isotherm depths were de-seasoned and de-trended using Γ_j from the 3-year Running mean.

Station:	N04	N05	N06	N07	N08	N09	N10
None :	0.240	0.469	0.477	0.617	0.578	0.564	0.576
U1 :	0.241	0.475	0.479	0.617	0.578	0.565	0.577
U2 :	0.262	0.500	0.480	0.619	0.579	0.564	0.576
U3 :	0.247	0.575	0.531	0.630	0.580	0.566	0.582
U4 :	0.253	0.469	0.487	0.643	0.584	0.564	0.586
U5 :	0.283	0.564	0.523	0.618	0.597	0.574	0.576
U6 :	0.250	0.533	**0.612**	**0.686**	0.578	0.567	0.578
U7 :	0.240	0.470	0.482	0.680	**0.618**	**0.575**	0.579
PcAH-1:	**0.291**	**0.605**	0.591	0.666	0.598	0.573	0.577
PcAH-2:	0.251	0.469	0.477	0.621	0.585	0.567	**0.587**
PcAH-3:	0.280	0.589	0.578	0.655	0.578	0.566	0.578
PcAU-1:	0.240	0.485	0.526	0.679	0.582	0.564	0.584
PcAU-2:	0.288	0.571	0.519	0.621	0.589	0.570	0.576
PcAU-3:	0.244	0.469	0.509	0.652	0.587	0.565	0.577

Table C5c. The altimetry parameters were de-trended and de-seasoned.and isotherm depths were de-seasoned and de-trended using Γ_j from Eq. (5.3).

| Station:	N04	N05	N06	N07	N08	N09	N10
None :	0.255	0.509	0.497	0.615	0.600	0.545	0.533
U1 :	0.255	0.515	0.498	0.615	0.604	0.545	0.533
U2 :	0.281	0.538	0.498	0.617	0.605	0.546	0.534
U3 :	0.261	0.595	0.533	0.625	0.605	0.549	0.535
U4 :	0.272	0.510	0.505	0.639	0.605	0.545	**0.542**
U5 :	0.300	0.598	0.533	0.616	0.627	**0.555**	0.533
U6 :	0.262	0.553	**0.601**	**0.670**	0.600	0.550	0.533
U7 :	0.255	0.514	0.500	0.665	**0.631**	0.550	0.534
PcAH-1:	**0.310**	**0.623**	0.580	0.655	0.623	0.553	0.533
PcAH-2:	0.267	0.510	0.498	0.619	0.607	0.546	0.540
PcAH-3:	0.293	0.605	0.568	0.644	0.604	0.550	0.533
PcAU-1:	0.256	0.518	0.533	0.666	0.602	0.546	0.538
PcAU-2:	0.305	0.603	0.528	0.618	0.620	0.553	0.533
PcAU-3:	0.258	0.510	0.525	0.643	0.606	0.545	0.533

Appendix D: Miscellaneous figures
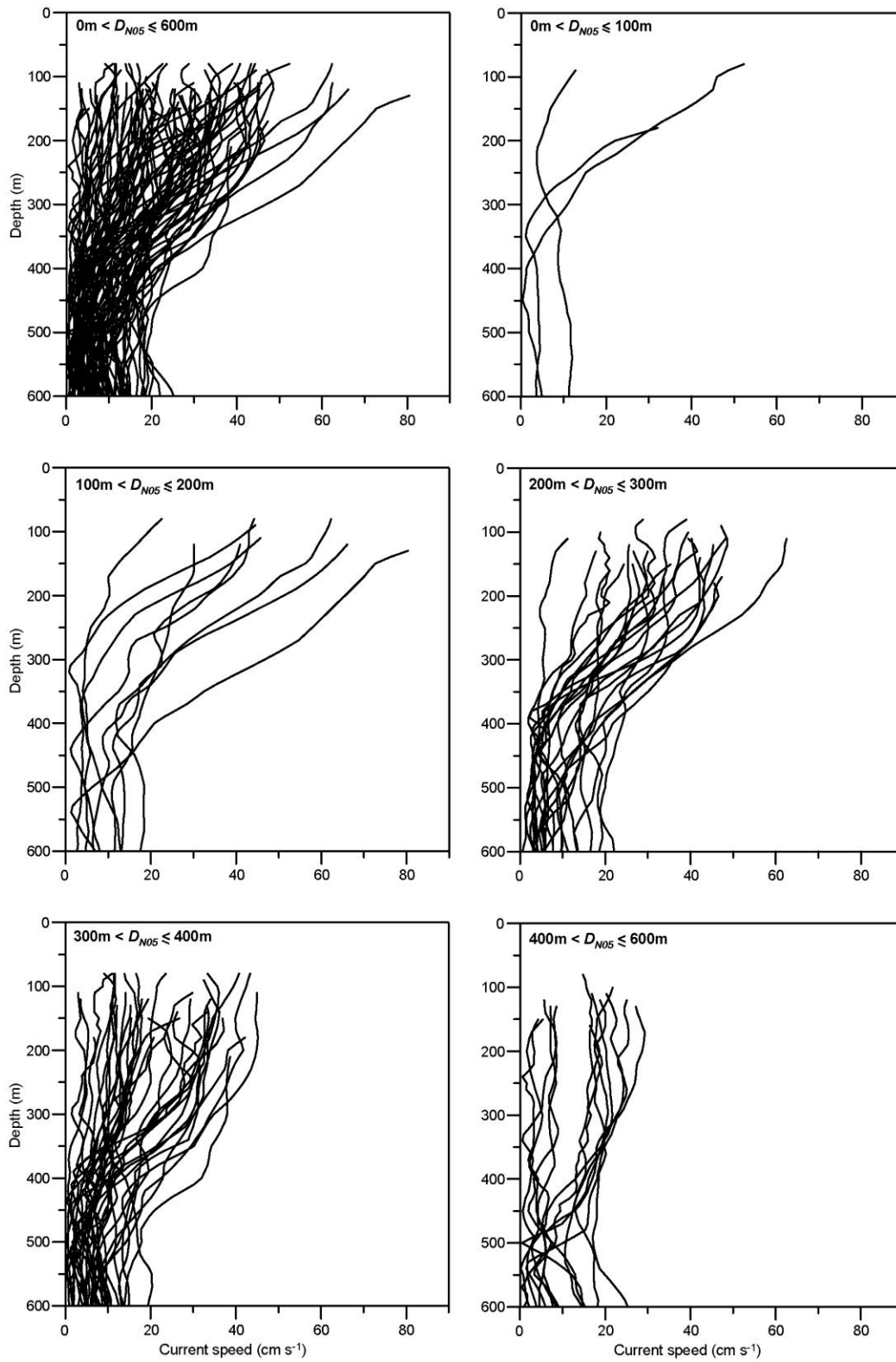
Figure D1. Vertical variation of current speed at NB sorted into groups according to the depth of the 4°C-isotherm at N05.
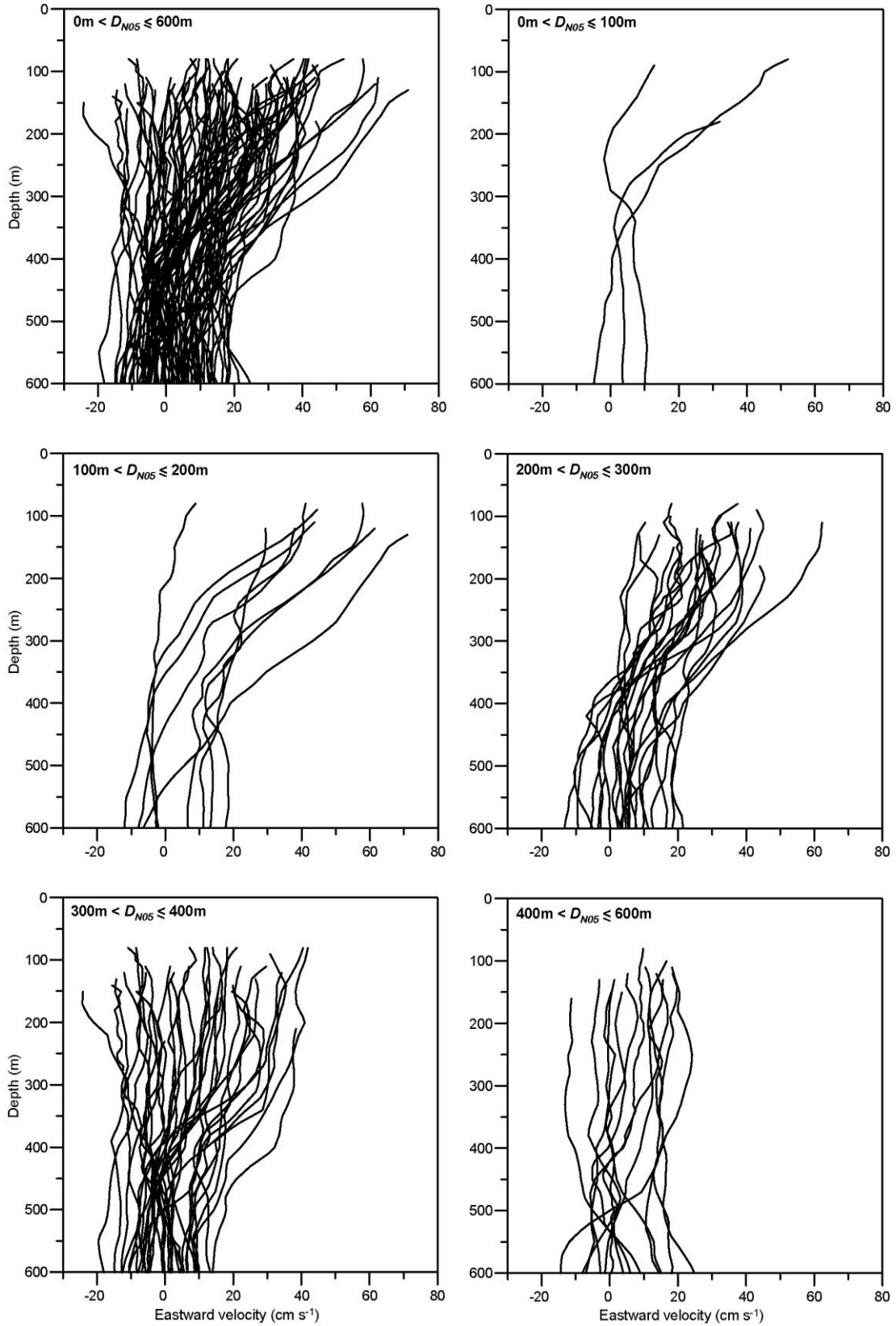
Figure D2. Vertical variation of Eastward velocity at NB sorted into groups according to the depth of the 4°C-isotherm at N05.
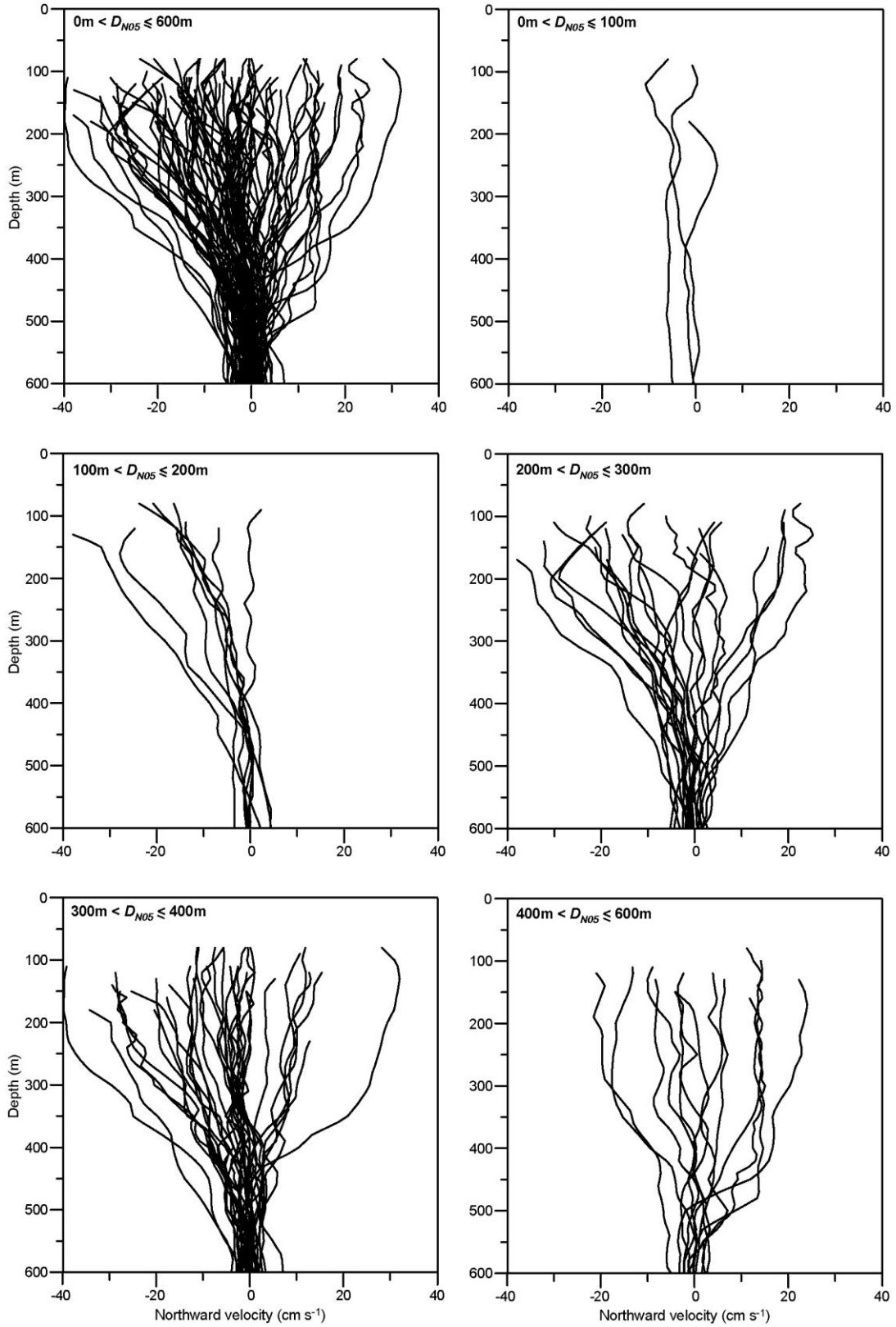
Figure D3. Vertical variation of Northward velocity at NB sorted into groups according to the depth of the 4°C-isotherm at N05.